

Cite this: *RSC Appl. Interfaces*, 2025, 2, 1171

## Progress in cathode catalysts for rechargeable aprotic lithium–oxygen batteries

Chen Liu \*<sup>a</sup> and Huahuan Wang<sup>b</sup>

Lithium–oxygen batteries (LOBs) are highly esteemed for their exceptional energy density ( $\sim 3500$  Wh  $\text{kg}^{-1}$ ) and are regarded as one of the most promising battery technologies. However, several challenges hinder the commercialization and widespread adoption of LOBs, including side reactions occurring at the lithium anode, electrolyte decomposition, and growth of lithium dendrites. These issues contribute to reduced cycle life and increased overpotential, adversely affecting the performance of LOBs. Consequently, exploring effective cathode catalysts is crucial for advancing this field. Initially, this review provides background information on LOBs, including that on singlet oxygen formation, and then clearly and succinctly outlines their operational mechanisms. Subsequently, a detailed analysis of recent developments in cathode catalysts for aprotic LOBs is presented, notably spin engineering and amorphization strategy for spinel oxides and development of high-entropy alloys. Finally, innovative directions are proposed, especially new soluble catalysts and machine learning, for investigating cathode catalysts and enhancing the electrochemical performance of LOBs considering existing challenges.

Received 25th May 2025,  
Accepted 11th July 2025

DOI: 10.1039/d5lf00153f

rsc.li/RSCApplInter

## Introduction

### Background

Nowadays, fossil fuels remain the dominant energy resources worldwide despite the rapid development of new energy, including solar, wind, and tidal energy.<sup>1</sup> As environmental issues such as climate change and global warming continue to deteriorate, more eco-friendly and renewable energy storage systems are under scientific research. Electric vehicles (EVs) have gained widespread adoption in recent years due to their sustainability and lower air pollution. However, the energy density of lithium-ion batteries (LIBs), which are the primary power source for EVs, is approaching their energy density limits.<sup>1,2</sup> Current commercialized LIBs ( $< 500$  Wh  $\text{kg}^{-1}$ ) cannot meet the demand for high-energy-density, lightweight battery solutions.<sup>1,2</sup> Thus, the application of LIBs is increasingly constrained.

By contrast, lithium–oxygen batteries (LOBs) can overcome the energy density deficiency with their extraordinarily high theoretical energy density of  $\sim 3500$  Wh  $\text{kg}^{-1}$  during discharging (based on  $\text{Li}_2\text{O}_2$ ). Therefore, LOBs have the potential to extend the mile range of EVs to more than 500 miles in an ideal scenario.<sup>2,3</sup> LOBs have emerged as the new star in the field of batteries since they were first reported in 1996 by Abraham and

Jiang.<sup>4</sup> Thus far, the major LOBs can be categorized into three types according to the differences in their electrolytes, which are aprotic, aqueous, and solid-state.<sup>4–8</sup> Among them, aprotic LOBs are the most popular and promising, which are the topic of this review. Through the persistent efforts of numerous scientists and researchers, a large variety of potential catalysts and electrolytes have been found and studied to facilitate the oxygen reduction reaction (ORR) and oxygen evolution reaction (OER). Thus, it appears that LOBs are advancing toward the stage of commercialization.

### Obstacles

However, as research progresses, several technical difficulties hinder the practical application of aprotic lithium–oxygen batteries (LOBs).<sup>5,8,9</sup>

In terms of the anode, the Li anode is highly reactive and tends to undergo side reactions with  $\text{CO}_2$  and  $\text{H}_2\text{O}$ .<sup>5,10,11</sup> Furthermore, the formation of Li dendrites, which is a common issue in all Li-based batteries, severely impairs the performance of  $\text{Li}-\text{O}_2$ .<sup>12</sup> Dendrites can lead to short circuit, dead Li, low coulombic efficiency (CE), more serious adverse reactions and increased polarization, which eventually result in safety hazards, shortened cycle life and reduced energy density.<sup>12,13</sup>

In the case of the cathode, the high charging overpotential ( $\eta_{\text{OER}}$ ) and short cycle life caused by the accumulation of insulating and insoluble  $\text{Li}_2\text{O}_2$  in the cathode are also fatal to aprotic LOBs.<sup>9,16,17</sup> Furthermore, the rate of  $\text{O}_2$  diffusion through the cathode materials is crucial for the  $\text{Li}-\text{O}_2$  performance; thus, improving the  $\text{O}_2$  diffusion kinetics becomes

<sup>a</sup> College of New Energy and Materials, China University of Petroleum, Beijing, PR China. E-mail: 13176230761@163.com

<sup>b</sup> State Key Laboratory of Heavy Oil Processing, China University of Petroleum, Beijing, PR China



another priority.<sup>18,19</sup> In cathodes composed of carbon, they also encounter erosion caused by  $\text{LiO}_2/\text{Li}_2\text{O}_2$ .<sup>106</sup>

In addition, nucleophiles, bases and free radicals including  $\text{LiO}_2$ ,  $\text{HOO}^-$ ,  $\text{HOO}^\cdot$ ,  $\text{O}_2^-$ , and even  $\text{Li}_2\text{O}_2$  are likely to attack the electrolyte.<sup>14,15,173</sup> The reactions of electrolyte decomposition are diverse, such as nucleophilic attack, auto-oxidation, acid/base reactions and proton-mediated reactions, which seriously hinder the performance of  $\text{Li}-\text{O}_2$  cells.<sup>165</sup> The decomposition of the electrolyte such as DME can result in its electrodeposition on the cathode, producing  $\text{CO}_2$  during charging.<sup>167</sup> Therefore, it is necessary to reduce the negative effects caused by reactive oxygen species (ROSS).

The relationship between cathodes with carbon and the electrolyte is inseparable, given that it has been reported that their decomposition results in a synergistic effect.<sup>166</sup> Bruce *et al.* found that in DMSO or TEGDME, the decomposition of the electrolyte is the main side reaction, which is accelerated by the catalysis of carbon, especially hydrophilic carbon.<sup>16</sup> Thus, to avoid  $\text{CO}_2$  emission from side reactions, Kang *et al.* used  $\text{LiNO}_3$  in DME as the electrolyte and its solvate on the surface of the cathode deactivated carbon.<sup>168</sup> The erosion of the carbon cathode and decomposition of the electrolyte catalyzed by carbon were both effectively controlled. Thus, these results demand a proper match between the cathodes and electrolyte in future research.

Furthermore, it seems that traditional catalysts have negative catalytic effects in  $\text{Li}-\text{O}_2$  cells. McCloskey *et al.* found that traditional OER catalysts on carbon ( $\text{Au}/\text{XC72}$ ,  $\text{MnO}_2/\text{XC72}$  and  $\text{Pt}/\text{XC72}$ ) had a lower Coulombic efficiency (OER/ORR) than pure carbon (XC72) in pure DME because these catalysts catalyzed the decomposition of DME into  $\text{CO}_2$  more than the oxidation of  $\text{LiO}_2/\text{Li}_2\text{O}_2$ .<sup>167</sup>

It is universally acknowledged that singlet oxygen ( $^1\Delta_g$  or  $^1\text{O}_2$ ), a type of ROS, exhibits greater reactivity with organic matter than other ROSS. It is widely reported that singlet oxygen also contributes to parasitic reactions in  $\text{Li}-\text{O}_2$  cells,<sup>10,11,169</sup> and water can lead to the generation of more  $^1\text{O}_2$ .<sup>170</sup> Thus far, several pathways for the formation of  $^1\text{O}_2$  have been proposed, mainly including the disproportionation of the superoxide anion,<sup>172</sup> the oxidation of the  $\text{LiO}_2$  superoxide intermediate above 3.5 V,<sup>169,173</sup> and the electrochemical oxidation of  $\text{Li}_2\text{CO}_3$ .<sup>174</sup>

However, the latest studies indicate that singlet oxygen is not the main source of electrolyte decomposition, and its production depends on the redox potential of the redox mediators (RMs).<sup>175,176</sup> Bruce *et al.* found that instead of  $^1\text{O}_2$ ,  $^3\text{O}_2$  is the main generated oxygen molecule when RMs are added to the electrolyte.<sup>176</sup>

In conclusion,  $^1\text{O}_2$  may contribute to carbon erosion and electrolyte decomposition, but is not the major cause of the latter.

Besides the above-mentioned negative impacts, singlet oxygen has been reported to decompose RMs.<sup>171</sup> However, RMs play an important role in the decomposition of the discharge products (mainly  $\text{Li}_2\text{O}_2$ ). The gradual deactivation of RMs causes  $\text{Li}_2\text{O}_2$  to be left on the cathode surface, and then the cathode catalyst cannot work normally.

Thus, to address these challenges, it is necessary to develop new effective, durable, and cost-effective cathode catalysts. Drawing on the understanding of the working principles of aprotic LOBs, this review systematically analyses the recent advances in cathode catalyst materials and several key modulation strategies. Additionally, it proposes several novel potential directions for enhancing the electrochemical performance of LOBs.

## Mechanisms of aprotic LOBs

Aprotic LOBs consist of an Li anode, a nonaqueous electrolyte or mixed nonaqueous electrolyte, a membrane, and a porous cathode, as shown in Fig. 1. Given that oxygen from the air needs to be reduced at the cathode, LOBs are semi-open batteries, which is a unique trait of metal-air batteries. The porous cathode is not directly involved in reactions but serves as a gas exchange channel, an electron transfer carrier, and a catalyst for nucleation, growth, and decomposition of  $\text{Li}_2\text{O}_2$  and other discharging products.<sup>9</sup>

However, the charging and discharging reactions taking place at the cathode were controversial to some extent in the early stage of research on  $\text{Li}-\text{O}_2$  batteries.

### ORR mechanisms

There are two oxygen reduction mechanisms or  $\text{O}_2$  reduction reactions in  $\text{Li}-\text{O}_2$  batteries, surface route and solution route.<sup>20</sup> At the cathode,  $\text{Li}_2\text{O}_2$  is the main discharge product due to the instability of  $\text{LiO}_2$ . According to the hard-soft acid-base theory, smaller cations are less effective in stabilizing  $\text{O}_2^{2-}$  compared to larger cations such as  $\text{Na}^+$ .<sup>3,21</sup>  $\text{Li}^+$  is too small to remain stable with  $\text{O}^{2-}$  and two  $\text{LiO}_2$  molecules transform into  $\text{Li}_2\text{O}_2$  and  $\text{O}_2$  through a disproportionation reaction. Film-like  $\text{Li}_2\text{O}_2$  is formed by the surface route, while toroidal  $\text{Li}_2\text{O}_2$  is observed by the solution route.

In the early stage, the surface electrochemical reactions of the surface route were thought to be as follows:<sup>5,21,22</sup>

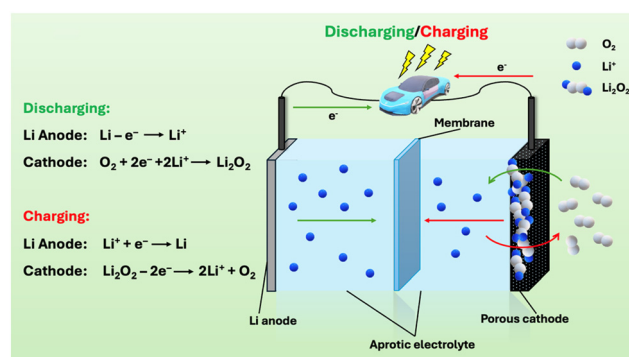
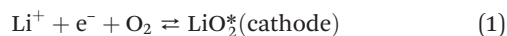


Fig. 1 Structure and working principles of aprotic LOBs. During discharge,  $\text{Li}^+$  ions move from the anode zone to the cathode zone, where  $\text{O}_2$  molecules are reduced on the cathode and then combine with  $\text{Li}^+$  to form insoluble  $\text{Li}_2\text{O}_2$ . During charge,  $\text{Li}^+$  ions move backwards, and  $\text{Li}_2\text{O}_2$  is oxidized to  $\text{O}_2$ , ideally.

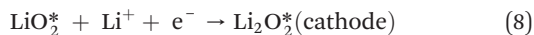
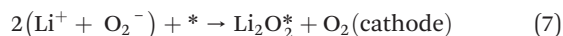
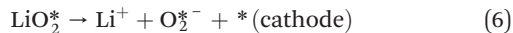
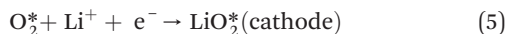
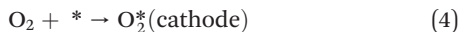




In all the equations in this part, the symbol \* in the upper right corner of a molecule means that the molecule is adsorbed on the cathode, and the individual \* means an adsorption site. Molecules without \* mean that they are in the gas or solid phase.  $\text{LiO}_{2(\text{sol})}$  (solvated  $\text{LiO}_2$ ) is replaced by  $\text{Li}^+$  and  $\text{O}_2^-$ .

The forward reactions occur during discharging, while the backward reactions take place during charging. However, it was unknown whether the specific steps of OER were just the reverse to the ORR at that time.

None of eqn (1)–(3) are solution electrochemical or chemical processes. Although there is clear evidence that  $\text{Li}_2\text{O}_2$  can barely dissolve in aprotic electrolytes,<sup>5</sup> some authors<sup>23</sup> thought that the absorbed  $\text{LiO}_2$  species can dissolve in TEGDME, and then nucleate, form  $\text{Li}_2\text{O}_2$  crystallites and grow into toroidal  $\text{Li}_2\text{O}_2$  at a relatively low current density. They thought that the following reactions happened in the solution route:



However, no toroidal  $\text{Li}_2\text{O}_2$  was observed in aprotic LOBs without water at any current density.<sup>24</sup> It is believed that the solution route happens preferentially in the presence of water, even trace amounts.<sup>22,24,25</sup> Also, the results of many experiments have proven the existence of the solution route with water.<sup>133,162</sup>

Then, Johnson *et al.* proposed a unified mechanism of ORR (Fig. 2a), which explains that the solubility of  $\text{LiO}_2$  determines the  $\text{Li}_2\text{O}_2$  form through either the surface route or the solution route.<sup>204</sup> After subsequent studies by other groups,<sup>205–207</sup> this improved mechanism has been widely accepted.

The solubility of  $\text{LiO}_2$  is thought to be determined mainly by the donor number (DN) and acceptor number (AN) of the solvent, with the former being more dominant.<sup>205</sup> High-DN and high-AN solvents have been proven favorable for the solution route.<sup>206,207</sup>

To meet practical use,  $\text{Li}-\text{O}_2$  batteries must run at a low discharge overpotential and a high current. Under a low discharge overpotential, in low-DN solvents such as acetonitrile (ACN) and/or low-AN solvents such as anhydrous DME, only film-like  $\text{Li}_2\text{O}_2$  is formed by the surface route, as follows.<sup>205</sup>

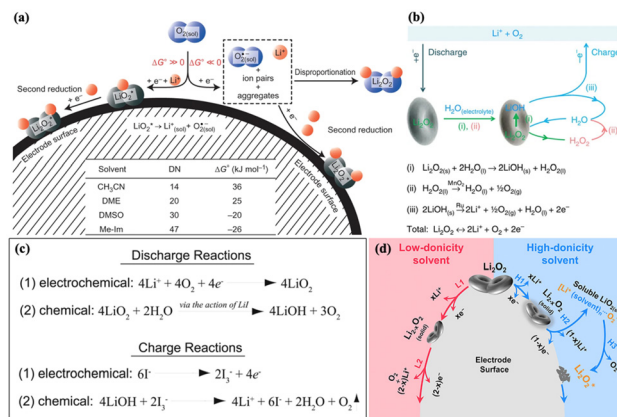
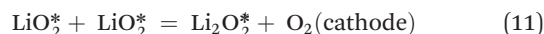
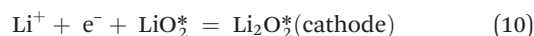
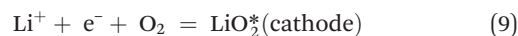
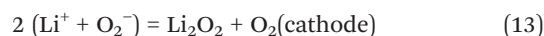
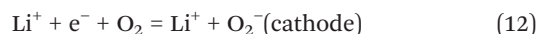


**Fig. 2** (a) Schematic of the first proposed unified  $\text{O}_2$  reduction mechanism in an aprotic solvent containing  $\text{Li}^+$ , showing the surface pathway followed when  $\Delta G^\circ \gg 0$  (low DN) and the solution pathway followed when  $\Delta G^\circ \ll 0$  (high DN).  $\Delta G^\circ$  refers to the following equation:  $\text{LiO}_2^* \rightleftharpoons \text{Li}^+ + \text{O}_2^- + \text{ion pairs} + \text{higher aggregates (clusters)}$ . The table shows the estimated  $\Delta G^\circ$  for this equation in solvents with various DNs. Reproduced with permission.<sup>204</sup> Copyright 2014, Springer Nature Limited. (b) Proposed mechanism for the discharging and charging processes of the cell with  $\text{Ru}/\text{MnO}_2/\text{SP}$  and the electrolyte containing a trace amount of  $\text{H}_2\text{O}$ . (i) Is a spontaneous process; (ii) is promoted over  $\text{MnO}_2$  nanoparticles in  $\text{Ru}/\text{MnO}_2/\text{SP}$ ; and the oxidation of  $\text{LiOH}$  in (iii) occurs at low charge overpotentials over  $\text{Ru}$  nanoparticles. Reproduced with permission.<sup>208</sup> Copyright 2015, Fujun Li *et al.* (c) Schematic mechanisms for the formation and removal of  $\text{LiOH}$  in iodide redox-mediated  $\text{Li}-\text{O}_2$  cells in the presence of water. The electron/ $\text{LiOH}$  molar ratios during discharge and charge are both equal to 1. Reproduced with permission.<sup>211</sup> Copyright 2015, The American Association for the Advancement of Science. (d) Proposed solvent-controlled  $\text{Li}_2\text{O}_2$  decomposition mechanism. "H" denotes a high-donicity solvent and "L" denotes a low-donicity solvent.  $\text{Li}_2\text{O}_2^*$  denotes the  $\text{Li}_2\text{O}_2$  generated by  $\text{LiO}_{2(\text{sol})}$  disproportionation. Reproduced with permission.<sup>212</sup> Copyright 2018, Elsevier.



In this circumstance,  $\text{LiO}_2$  on the cathode surface cannot dissolve in solvents and tends to be further reduced (eqn (10)) or undergo a disproportionation reaction<sup>205</sup> (eqn (11), not shown in Fig. 2a) and form film-like  $\text{Li}_2\text{O}_2$ .

By contrast, in high-DN solvents such as DMSO and/or high-AN solvents such as water and  $\text{CH}_3\text{OH}$ ,<sup>207</sup> toroidal  $\text{Li}_2\text{O}_2$ , as the major product, is formed by the solution route.<sup>205</sup> However, a second reduction still happens in high-DN and/or high-AN solvents to some extent, possibly due to its fast reaction speed.<sup>204</sup>



In this case, solvated  $\text{LiO}_2$  mainly undergoes the dominant disproportionation reaction (eqn (13)). At the same time, solvated  $\text{O}_2^-$  also can be further reduced, and then combines with two  $\text{Li}^+$  ions to form minor film-like  $\text{Li}_2\text{O}_2$  (eqn (14)), as shown in Fig. 2a.

It is widely known that insoluble  $\text{LiOH}$  can be formed in the presence of an appropriate amount of water. As mentioned above, even trace water can prompt the formation of toroidal  $\text{Li}_2\text{O}_2$ , which increases the battery capacity. With an increase in the content of water, it was reported that the size of  $\text{Li}_2\text{O}_2$  also increases. Li *et al.* observed  $\text{LiOH}$  in  $\text{Li}-\text{O}_2$  cells with 0.5 M  $\text{LiClO}_4$  in DMSO with 120 ppm  $\text{H}_2\text{O}$ .<sup>208</sup> They proved that  $\text{Li}_2\text{O}_2$  transformed to  $\text{LiOH}$  through a chemical process. Based on the experimental results, the overall ORR and OER mechanism for  $\text{Li}-\text{O}_2$  systems with trace water was proposed (Fig. 2b).

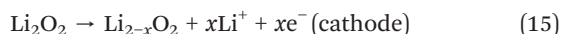
However, no  $\text{LiOH}$  was detected in  $\text{Li}-\text{O}_2$  batteries with 1 M  $\text{LiTFSI}$  in DME with varying water contents (up to 4000 ppm).<sup>207</sup> However, the formation of  $\text{H}_2\text{O}_2$  was indirectly proven. It was explained that the reason why no  $\text{LiOH}$  was detected in the former study<sup>207</sup> may be that after a small amount of water was consumed, the existing  $\text{H}_2\text{O}_2$  could not transform into  $\text{H}_2\text{O}$  without catalysts such as  $\text{MnO}_2$ , which led to the reverse reaction of step (i), and then  $\text{Li}_2\text{O}_2$  was the major discharge product.<sup>208</sup>

However, it seems that there is no unified ORR mechanism for water-containing  $\text{Li}-\text{O}_2$  systems. With an increase in the water content, different mechanisms have been put forward.<sup>209–211</sup> For example, in  $\text{Li}-\text{O}_2$  systems with added  $\text{LiI}$  redox mediator and 45 000 ppm  $\text{H}_2\text{O}$ , their discharge and charge reactions are shown in Fig. 2c.<sup>211</sup> In this case,  $\text{LiOH}$  is produced from  $\text{LiO}_2$  and  $\text{H}_2\text{O}$  *via* the action of  $\text{LiI}$ .

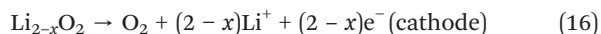
### OER mechanisms

Contrary to the stable discharge voltage platform during ORR, a dramatic upward charge voltage and turning points exist during OER, which indicates the orderly steps for the oxidation of different discharge products. In general, the decomposition voltage for  $\text{LiOH}$  is lower than that for  $\text{Li}_2\text{O}_2$ ,<sup>208</sup> whereas the voltage for the decomposition of  $\text{Li}_2\text{CO}_3$  is higher than that for  $\text{Li}_2\text{O}_2$  and  $\text{LiOH}$ .<sup>106</sup>

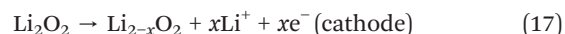
Wang *et al.* proposed an OER mechanism that relates the decomposition of  $\text{Li}_2\text{O}_2$  to the donicity (donor number, namely) of the solvent (Fig. 2d).<sup>212</sup> In low-donicity solvents, owing to their low ability to dissolve  $\text{LiO}_2$ ,  $\text{Li}_2\text{O}_2$  first decomposes into solid  $\text{Li}_{2-x}\text{O}_2$ , as follows:



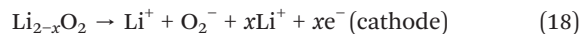
Then, when the Li deficiency reaches a critical point,  $\text{Li}_{2-x}\text{O}_2$  becomes unstable and further decomposes into  $\text{O}_2$ :



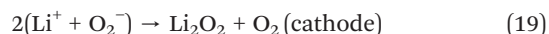
In high-donicity solvents,  $\text{Li}_2\text{O}_2$  also first transforms into  $\text{Li}_{2-x}\text{O}_2$ :



After that,  $\text{Li}_{2-x}\text{O}_2$  can dissolve in high-donicity solvents:



Then, solvated  $\text{LiO}_2$  can undergo disproportionation:



However, as mentioned before, disproportionation of the superoxide anion ( $\text{O}_2^-$ ) contributes to  $^1\text{O}_2$  formation, which causes electrolyte degradation to some extent.  $\text{LiO}_2$  itself also can attack the electrolyte. Therefore, although high-DN solvents are favorable for the solution route during ORR, they may be not suitable for OER. It has been suggested that adding RMs to solvents can improve  $\text{Li}-\text{O}_2$  cells.<sup>212</sup> In this way, oxidized RM ( $\text{RM}^+$ ) reacts with  $\text{Li}_2\text{O}_2$  and produces  $\text{O}_2$ ,  $\text{Li}^+$  and RM without  $\text{LiO}_2$ .

## Metrics of structures and performances of catalysts

In this review, we mainly assess catalysts in terms of the following aspects.

In the case of rechargeable aprotic  $\text{Li}-\text{O}_2$  batteries, improving the diffusion of  $\text{O}_2$  is important, which further depends on the number and structure of pores in the catalysts. Then, the adsorption energies for  $\text{O}_2$  or intermediates especially  $\text{LiO}_2$ , which are subject to change depending on the electronic structure of the catalyst, determine the amount of deposited  $\text{Li}_2\text{O}_2$  and its formation route. They can influence the ORR/OER overpotentials, reversibility, capacity, and cycling life of  $\text{Li}-\text{O}_2$  cells. Therefore, the electronic structure of catalysts needs much attention. It is obvious and accepted that more  $\text{Li}_2\text{O}_2$  can deposit on the unit surface area of the catalyst when its specific surface area is larger, especially in the case of 2D and hierarchical catalysts, leading to a more favorable capacity.

Considering the commercialization of LOBs, they need to satisfy the electricity demand of humans, who are concerned about their useful lives and maximum capacities. In addition, to make LOBs more enduring, their ORR/OER overpotentials must be low.

Therefore, in nearly all modulation strategies, the optimization of the structure of the pores, electronic structure and/or specific surface area is the method applied to achieve an improvement in cycling capability, increase in maximum capacity, and/or decrease in the ORR/OER overpotentials of  $\text{Li}-\text{O}_2$  cells.

To make this clear, several vital metrics are listed and stated briefly.



### 1. The structure of pores

Due to the importance of appropriate size and number of pores to achieve O<sub>2</sub> diffusion, the structure of the pores of several catalysts, especially carbon-based materials and MOF-based materials are given attention.

### 2. The electronic structure

Modulation strategies such as doping and vacancy engineering can change the electronic structure of materials, which can be proven by the peak shifts in XPS, changes in the adsorption energies for O<sub>2</sub>, intermediates and the discharge products, AC impedance measurements, outcomes of DFT calculation, *etc.*

### 3. Specific surface area

Regarding catalyst materials, especially carbon-based and MOF-based catalysts, a higher specific surface area leads to the greater deposition of discharge products, which results in a larger capacity in batteries.

### 4. Cycling capability

The cycling number of a catalyst within a specific voltage window and/or within a set coulombic efficiency shows its potential as a practical catalyst in the future. More cycles under the same testing conditions indicate that the battery is more durable.

### 5. Maximum capacity

The maximum capacity determines the working duration of Li–O<sub>2</sub> cells until electricity runs out. A larger maximum capacity at the same rate means a longer working time for batteries.

### 6. ORR/OER overpotentials

Besides good cycling capability and a large maximum capacity, an ideal catalyst also needs to show low ORR and OER overpotentials. Typically, the OER and ORR overpotentials increase as cycling proceeds. Therefore, in this review, we summarize the OER and ORR overpotentials in the first cycle in Table 1.

Considering the above-mentioned factors, the potential of developed materials as Li–O<sub>2</sub> cathode catalysts can be in a systematically and comprehensively assessed.

## Progress in cathode catalysts

Since Abraham and Jiang's first report on LOBs in 1996, the research on LOBs has continuously increased. However, many technical difficulties have been encountered both in the anode and cathode. In this case, compared to the Li anode, the obstacles associated with the cathode are more complicated due to its unclear reaction mechanisms.<sup>3,5,21,22</sup> Therefore, the exploration of methods for improving the performance of the cathode is vital for the commercialization of LOBs. In recent years, various cathode catalysts have been synthesized and tested, mainly including transition metals and their compounds,<sup>26–29</sup> carbon-based materials,<sup>30–32</sup> noble metals and their corresponding oxides,<sup>33–41</sup> and metal–organic-framework-based (MOF-based) materials.<sup>42–44</sup>

In the case of transition-metal spinel oxides, morphological control and pore structure optimization are

the key to improving their catalytic performance. Side reactions need to be suppressed for carbon-based materials. Thus, electronic structure adjustment, crystal plane effects, and formation of composites with noble metal-free materials are the common strategies applied for the preparation of noble-metal-based catalysts. In the case of MOF-based materials, despite their controllable pore structure, they have the drawbacks of poor electronic conductivity and complex synthesis. Thus, to achieve the practical application of Li–O<sub>2</sub> batteries, the impeding problems must be addressed.

### Transition metal compounds

Owing to their relatively low cost and natural abundance on Earth, transition metals have been extensively researched and utilized in the synthesis of transition metal compounds (TMCs), including transition metal oxides, carbides, sulfides, and phosphides. Many of them have the potential to function as cathode catalysts in LOBs. Among these materials, spinel-structured transition metal oxides have been the most prevalent in research recently.

**Spinel oxides.** The typical structural formula<sup>48</sup> of AB<sub>2</sub>O<sub>4</sub> contains two metals, A and B, such as NiCo<sub>2</sub>O<sub>4</sub>, or one metal element when A and B are the same, such as Co<sub>3</sub>O<sub>4</sub>. The oxide ions are negative bivalent ions. To achieve electric neutrality, metal ion A can be positive bivalent with two positive trivalent B ions, or A can be positive quadrivalent with two positive bivalent B ions, respectively. The A and B cations can exist in tetrahedrons and octahedrons with diverse ratios. Therefore, spinel oxides can be categorized into normal spinels, inverse spinels, and complex spinels.<sup>49</sup> To describe their structures better, A<sub>1-x</sub>B<sub>x</sub>[A<sub>x</sub>B<sub>2-x</sub>]O<sub>4</sub> is introduced, where *x* is between 0 and 1. Inverse spinels (when *x* = 1) can be described as B[AB]O<sub>4</sub>.<sup>50</sup>

Due to their many advantages,<sup>5,49,51,52</sup> including low cost, easy synthesis, controllable structure, high activity in ORR and OER, and good thermodynamic stability in alkaline media, spinels are widely used in LOBs. Moreover, to optimize their electronic structure, increase the number of active sites, and improve their electrical conductivity, many modification strategies<sup>9,20,26,53</sup> have been applied, including doping modification, vacancy engineering, heterostructure engineering, crystal plane effects, synergistic effects, and dimension engineering. In this chapter, several common spinel oxides will be introduced.

**1. Co<sub>3</sub>O<sub>4</sub>.** One of the most common spinel oxides is Co<sub>3</sub>O<sub>4</sub>, which has been widely used as an electrocatalyst for ORR and OER.<sup>55,56</sup> However, although spinel oxides have many advantages, as mentioned above, they still require doping engineering and defect engineering to optimize their electronic structure and reduce their overpotential. Recently, Xia *et al.* constructed an oxygen-rich metal–organic skeleton-derived nickel-doped Co<sub>3</sub>O<sub>4</sub> material (Ni–Co<sub>3</sub>O<sub>4</sub>–Vo).<sup>54</sup> Through Ni doping and NaBH<sub>4</sub> treatment, double oxygen vacancies were introduced in Ni-doped Co<sub>3</sub>O<sub>4</sub> (Fig. 3a). Fig. 3c shows the high-resolution XPS spectra of Co 2p, where



Table 1 Summary of the cathode catalysts mentioned in this review

	The first OER potential <sup>a</sup> (V)	The first ORR potential <sup>b</sup> (V)	Maximum capacity <sup>c</sup> (mAh g <sup>-1</sup> )/rate <sup>d</sup> (mA g <sup>-1</sup> )	Cycle number/cut-off capacity <sup>e</sup> (mAh g <sup>-1</sup> )/rate <sup>d</sup> (mA g <sup>-1</sup> )	Electrolyte	Ref.
Transition metal compounds (spinel oxides and composites)						
Co <sub>3</sub> O <sub>4</sub> films/Ni foams	~3.5	~2.5	2460/200	35/1000/200	1.0 M LiTFSI in TEGDME	18
Co-Mn-O	~4.0	~2.75	7653/0.04 mA cm <sup>-2</sup>	100/500/0.16 mA cm <sup>-2</sup>	1.0 M LiCF <sub>3</sub> SO <sub>3</sub> in TEGDME	27
ZnCo <sub>2</sub> O <sub>4</sub> nanoflakes	~4.0	~2.6	—	30/500/0.1 mA cm <sup>-2</sup>	1.0 M LiTFSI in TEGDME	28
NiFeO-600	~3.5	~2.75	23 413/100	193/1000/1000 300/2000/500	1.0 M LiTFSI in TEGDME	29
Ni-Co <sub>3</sub> O <sub>4</sub> -Vo	4.06	2.65	5275/200	371/500/200 337/500/500	1.0 M LiTFSI in TEGDME	56
Co <sub>3-x</sub> O <sub>4</sub> , Co-300	~4.0	~2.7	14 517/100	70/1000/100	1.0 M LiTFSI in TEGDME	62
Co <sub>3</sub> O <sub>4</sub> @ND-CN	4.10	2.78	9838.8/100	80/1000/100	1.0 M LiTFSI in TEGDME	63
Co <sub>3</sub> O <sub>4</sub> -HCNFs	~4.3	~2.6	14 949/100	180/600/100	1.0 M LiCF <sub>3</sub> SO <sub>3</sub> in TEGDME	64
Co <sub>3</sub> O <sub>4</sub> NF/GNF	~4.1	~2.7	10 500/200	80/1000/200	1.0 M LiTFSI in TEGDME	65
Pt-Co <sub>3</sub> O <sub>4</sub> NWS@CP	~3.8	~2.8	17079.4/100	75/500/100	1.5 M LiTFSI in TEGDME	66
Co <sub>2</sub> N/Co <sub>3</sub> O <sub>4</sub> -Ti <sub>3</sub> C <sub>2</sub> Tx	~3.2	~2.6	14 271/100	>300/500/500	1.0 M LiTFSI in TEGDME	67
Ni <sub>5A</sub> -Co <sub>3</sub> O <sub>4</sub> /CC	~3.3	~2.5	21 442/200	128/1000/200	1.0 M LiCF <sub>3</sub> SO <sub>3</sub> in TEGDME	68
{112} faceted Co <sub>3</sub> O <sub>4</sub> plate	~3.9	~2.7	9144/100	45/500/-	1.0 M LiCF <sub>3</sub> SO <sub>3</sub> in TEGDME	159
Co <sub>3</sub> O <sub>4</sub> -H	~3.5	~2.65	5200/200	>100/500/200	1.0 M LiTFSI in TEGDME	160
Mesoporous ZnCo <sub>2</sub> O <sub>4</sub> nanoflakes	~4.0	~2.6	~1322/0.1 mA cm <sup>-2</sup>	30/500/0.1 mA cm <sup>-2</sup>	1.0 M LiTFSI in TEGDME	177
3DOM ZnCo <sub>2</sub> O <sub>4</sub>	~3.9	~2.75	6024/100	27/500/100	1.0 M LiCF <sub>3</sub> SO <sub>3</sub> in TEGDME	178
Porous ZnCo <sub>2</sub> O <sub>4</sub> nanofibers	~4.25	~2.75	~12 500/1000	226/1000/500	1.0 M LiNO <sub>3</sub> in DMAc	180
ZnCo <sub>2</sub> O <sub>4</sub> /CC	~3.8	~2.7	4.23 mAh cm <sup>-2</sup> /0.12 mA cm <sup>-2</sup>	80/0.3 mAh cm <sup>-2</sup> /0.2 mA cm <sup>-2</sup>	1.0 M LiTFSI in TETRAGLYME	181
NiCo <sub>2</sub> O <sub>4</sub> /CC	~3.65	~2.75	6.2 mAh cm <sup>-2</sup> /0.12 mA cm <sup>-2</sup>	200/0.3 mAh cm <sup>-2</sup> /0.2 mA cm <sup>-2</sup>		
CuCo <sub>2</sub> O <sub>4</sub> /CC	~3.6	~2.7	4.76 mAh cm <sup>-2</sup> /0.12 mA cm <sup>-2</sup>	107/0.3 mAh cm <sup>-2</sup> /0.2 mA cm <sup>-2</sup>		
FeCo <sub>2</sub> O <sub>4</sub> /CC	~3.85	~2.7	4.75 mAh cm <sup>-2</sup> /0.12 mA cm <sup>-2</sup>	107/0.3 mAh cm <sup>-2</sup> /0.2 mA cm <sup>-2</sup>		
Cu <sub>1-x</sub> ZnCo <sub>2</sub> O <sub>4</sub> (Cu <sub>0.15</sub> Zn <sub>0.85</sub> Co <sub>2</sub> O <sub>4</sub> )	~3.8	~2.65	12984.9/100	400/1000/200	1.0 M LiTFSI in TEGDME	182
ZCO-650	~3.46	~2.85	—	800 h/1000/500	1.0 M LiClO <sub>4</sub> in DMSO	183
NiCo <sub>2</sub> O <sub>4</sub> /SP	~3.9	~2.8	>8300/100	128/1000/200	1.0 M LiTFSI in TEGDME	184
NiCo <sub>2</sub> O <sub>4</sub> microspheres	~4.0	~2.9	3163/0.08 mA cm <sup>-2</sup>	60/500/0.24 mA cm <sup>-2</sup>	0.1 M LiClO <sub>4</sub> in DMSO	185
Au/NiCo <sub>2</sub> O <sub>4</sub> /3D-G	~3.9	~2.8	1275/42.5	40/510/42.5	0.1 M LiClO <sub>4</sub> in DME	186
NiCo <sub>2</sub> O <sub>4</sub> NS@Ni	~3.4	~2.8	7004/40	100/500/100	0.5 M LiClO <sub>4</sub> in DMSO	187
Flower-like NCO/N-rGO	~4.0	~2.7	15 046/200	50/1000/200	LiTFSI in TEGDME	188
CeO <sub>2</sub> @NiCo <sub>2</sub> O <sub>4</sub> NWAs	~3.1	~2.95	~3250/100	64/500/100	1.0 M LiCF <sub>3</sub> SO <sub>3</sub> in TEGDME	189
NiCo <sub>2</sub> O <sub>4</sub> @CNFs	~4.0	~2.6	4179/100	350/1000/200	1.0 M LiTFSI in TEGDME	190
NCO@CMs	~4.0	~2.7	6489.5	90/1000/	1.0 M LiTFSI in TEGDME	191
NCO-500	~4.2	~2.7	9231/100	80/600/100	1.0 M LiTFSI in TEGDME	193
3D foam-like NiCo <sub>2</sub> O <sub>4</sub>	~3.95	~2.87	10 137/200	80/1000/200	1.0 M LiCF <sub>3</sub> SO <sub>3</sub> in TEGDME	194
Bowl-like NiCo <sub>2</sub> O <sub>4</sub> @CFPs	~3.55	~2.7	9624.2/100	100/500/100	1.0 M LiTFSI in TEGDME	195
NCO@BCNNT	~4.0	~2.8	9823/100	320/1000/500	1.0 M LiCF <sub>3</sub> SO <sub>3</sub> in TEGDME	196
CuNiCo-5-5@Ni mesh	~3.9	~2.8	~7300/-	—	1.0 M LiNO <sub>3</sub> in DMSO	197
CCNO	~3.49	~2.9	9421.7/500	174/1000/500	1.0 M LiClO <sub>4</sub> in DMSO	198
TP-NCO/MO	~3.73	~3.0	~6 mAh cm <sup>-2</sup> /0.2 mA cm <sup>-2</sup>	480/0.5 mAh cm <sup>-2</sup> /0.5 mA cm <sup>-2</sup> 800/0.2 mAh cm <sup>-2</sup> /0.2 mA cm <sup>-2</sup>	1.0 M LiTFSI in TEGDME	199
NiCo <sub>2</sub> O <sub>4</sub> /Ni <sub>x</sub> P	~3.4	~2.9	7.41 mAh cm <sup>-2</sup> /0.1 mA cm <sup>-2</sup>	563/0.2 mAh cm <sup>-2</sup> /0.2 mA cm <sup>-2</sup>	1.0 M LiTFSI in TEGDME	200
NCO 120	~3.6	~2.85	13 759/100	173/500/100	1.0 M LiTFSI in TEGDME	201
Transition metal compounds (other transition metals and their compounds and composites)						
TiC	~3.5	~2.6	—	100/350/1000 mA cm <sup>-2</sup>	0.5 M LiClO <sub>4</sub> in DMSO	46
	~3.5	~2.75	—	25/525/1000 mA cm <sup>-2</sup>	0.5 M LiPF <sub>6</sub> in TEGDME	



Table 1 (continued)

	The first OER potential <sup>a</sup> (V)	The first ORR potential <sup>b</sup> (V)	Maximum capacity <sup>c</sup> (mAh g <sup>-1</sup> )/rate <sup>d</sup> (mA g <sup>-1</sup> )	Cycle number/cut-off capacity <sup>e</sup> (mAh g <sup>-1</sup> )/rate <sup>d</sup> (mA g <sup>-1</sup> )	Electrolyte	Ref.
Mo <sub>3</sub> P	3.23	2.88	—	1200/500/500	0.3 M LiTFSI in a 72:25 volumetric ratio of DMSO: EMIM-BF <sub>4</sub> mixture with 25 × 10 <sup>-3</sup> m of each of TEMPO and DBBQ RMs	47
Co <sub>3</sub> O <sub>4</sub> -TiO <sub>2</sub> (B)	~3.9	~2.75	11 000/100	200/1000/100	1.0 M LiTFSI in TEGDME	57
V-TiO <sub>2</sub> /Ti <sub>3</sub> C <sub>2</sub> Tx	~2.9	~2.75	11 487/100	200/1000/100	1.0 M LiTFSI in TEGDME	58
V <sub>2-x</sub> O <sub>5</sub> @V <sub>2</sub> C MXene, V-400	~3.25	~2.9	>5000/400	501/1000/100	1.0 Mol L <sup>-1</sup> LiTFSI in 100 μL of TEGDME	69
Ni <sub>2</sub> P/Ni <sub>12</sub> P <sub>5</sub> @NF	3.63	2.74	13254.1/500	120/1000/500	1.0 M LiTFSI in TEGDME	71
NiS <sub>2</sub> -NSs	~4.0	~2.6	22 500/500	314/1000/1000	1.0 M of LiNO <sub>3</sub> in DMAC with 0.1 M of TEMPO RM	72
MoS <sub>2-x</sub> /hEG	~3.85	~2.5	19000.3/500	>500/1000/1000	1.0 M LiTFSI in TEGDME	73
CoO/Ti <sub>3</sub> C <sub>2</sub> Tx	3.26	2.72	16 220/100	>160/500/100	1.0 M LiTFSI in TEGDME	78
CoP CPHs	~3.6	~2.95	33 743/50	236/1000/300	1.0 M LiTFSI in TEGDME	161
CoP NPs	~3.8	~3.0	20 264/50	221/1000/300	1.0 M LiTFSI in TEGDME	161
Carbon-based materials						
N1-wdC-900	~3.8	~2.8	9.44 mAh cm <sup>-2</sup> /0.05 mA cm <sup>-2</sup>	113/0.05 mAh cm <sup>-2</sup> /0.05 mA cm <sup>-2</sup>	1.0 M LiTFSI in TEGDME	30
Carbon-black-based self-standing membrane	~3.5	~2.65	7000/0.4 mA cm <sup>-2</sup>	7/3 mAh cm <sup>-2</sup> /0.3 mA cm <sup>-2</sup>	0.5 M LiTFSI, 0.5 M LiNO <sub>3</sub> , and 0.5 M LiBr	31
MACF	~3.5	~2.6	11 150/1000 ~7800/2000	110/1000/300	0.05 M LiI and 1.0 M LiCF <sub>3</sub> SO <sub>3</sub> in TEGDME	34
N-rGO	4.21	2.64	10 818/200	40/1000/400	1.0 M LiTFSI in TEGDME	70
Woven CNT	~4.7	~2.6	>2500/2000	>60/1000/2000	1.0 M LiPF <sub>6</sub> in 0.21 mL TEGDME	83
SWNT/CNF buckypapers	—	—	>2500/0.1 mA cm <sup>-2</sup>	—	1.0 M LiPF <sub>6</sub> in PC and THF	84
GNSs	—	—	8705.9/75	—	1.0 M LiPF <sub>6</sub> in PC/EC (1 : 1 weight ratio)	85
N-a-ex-G/KB	—	—	~11 800/70	—	1.0 M LiPF <sub>6</sub> in TEGDME	86
3D HGNS	~4.0	~2.75	~3600/100	18/1000/100	1.0 M LiTFSI in TEGDME	87
Mesocellular carbon foam	—	—	2500/0.1 mA cm <sup>-2</sup>	—	1.0 M LiClO <sub>4</sub> in PC	88
MCC	~3.8	~2.8	26 100/200	25/1000/400	0.1 M LiClO <sub>4</sub> in DMSO	92
Hierarchically woven CNT fibrils	~4.4	~2.6	—	70/1000/2000	1.0 M LiPF <sub>6</sub> in TEGDME	95
N-CNTs	—	—	866/75	—	1.0 M LiPF <sub>6</sub> in PC	99
1D C@LSSO NFs	~3.7	~2.7	8058.3/200	54/500/200	1.0 M LiTFSI in TEGDME	100
N-GNSs	—	—	11 660/75	—	1.0 M LiPF <sub>6</sub> in TEGDME	101
S-GNSs	—	—	~4300/75	—	1.0 M LiPF <sub>6</sub> in TEGDME	102
Co-SAs/N-C	~3.4	~2.8	20 105/200	260/1000/400	1.0 M LiTFSI in TEGDME	103
Porous graphene (PEG-2)	~4.1	~2.75	29 375/200	20/500/200	0.1 M LiClO <sub>4</sub> in DMSO	104
CNT@RuO <sub>2</sub>	3.56	2.69	4350/385	100/500/100	LiTFSI/TRIGLYME (1 : 5)	108
TiC/MWNTs	~3.4	~2.65	1800/—	10/1000/250	0.5 mol L <sup>-1</sup> LiClO <sub>4</sub> in DMSO	109
AAO/Ta/Fe/CNT	~4.2	~2.7	~4900/43	>10/—/309	0.1 M LiClO <sub>4</sub> in DME	163
Ni-CNTs@Ni	—	—	1814/0.05 mA cm <sup>-2</sup>	9/500/0.05 mA cm <sup>-2</sup>	1.0 M LiPF <sub>6</sub> in DMSO	164
Noble metals and their alloys, oxides, and composites						
Nanoporous gold (NPG)	~3.4	~2.6	325/500	100/—/500	0.1 M LiClO <sub>4</sub> in DMSO	33
RuO <sub>2</sub> decorated MACF (R-MACF)	~3.5	~2.8	13 290/1000 9112/2000	154/1000/300	0.05 M LiI and 1.0 M LiCF <sub>3</sub> SO <sub>3</sub> in TEGDME	34
PtRu	~4.0	~2.75	3689/100	120/1000/500	1.0 M LiTFSI in TEGDME	35
PtAu	~3.4	~2.7	5049/100	220/1000/500	1.0 M LiCF <sub>3</sub> SO <sub>3</sub> in TEGDME	36
Anisotropic Pt	~3.1	~2.75	12 985/200	70/1000/1000	1.0 M LiCF <sub>3</sub> SO <sub>3</sub> in TEGDME	36
Pt <sub>3</sub> Co/KB	~3.2	~2.7	5600/200	70/1000/200	1.0 M LiTFSI in TEGDME	37
PtIr multipods	3.29	2.85	8698/100	180/1000/100	NMP	38
Pd/Al <sub>2</sub> O <sub>3</sub> /C	~3.2	~2.7	2750/100	15/500/100	1.0 M LiCF <sub>3</sub> SO <sub>3</sub> in TEGDME	40
TOH Au NCs@SP	3.63	~2.8	~20 298/100 14 583/400	>30/1000/200	1.0 M LiNO <sub>3</sub> in DMSO	41
PdFe/N-rGO	4.08	2.62	~4800/200	400/1000/400	1.0 M LiTFSI in TEGDME	70
Pd/N-rGO	3.773	2.767	~6700/200	100/1000/400	1.0 M LiTFSI in TEGDME	70
PdCo/N-rGO	3.90	2.83	~5800/200	120/1000/400	1.0 M LiTFSI in TEGDME	70
PdNi/N-rGO	4.08	2.84	~4900/200	200/1000/400	1.0 M LiTFSI in TEGDME	70
Ru-CB	~3.3	~2.8	9800/200	150/1000/200	0.1 M LiClO <sub>4</sub> in DMSO	82

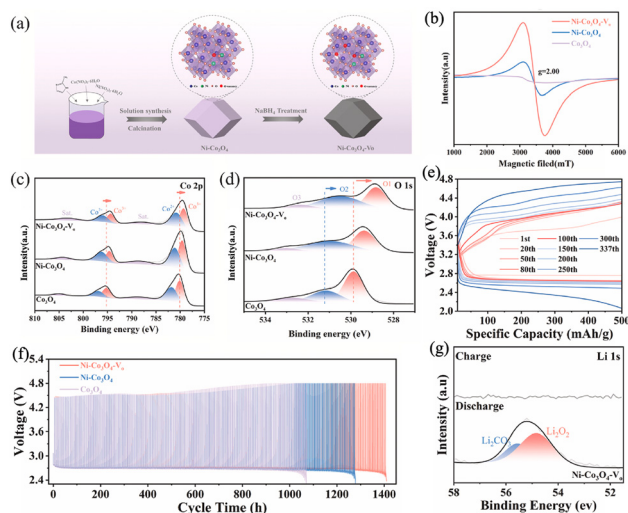


Table 1 (continued)

	The first OER potential <sup>a</sup> (V)	The first ORR potential <sup>b</sup> (V)	Maximum capacity <sup>c</sup> (mAh g <sup>-1</sup> )/rate <sup>d</sup> (mA g <sup>-1</sup> )	Cycle number/cut-off capacity <sup>e</sup> (mAh g <sup>-1</sup> )/rate <sup>d</sup> (mA g <sup>-1</sup> )	Electrolyte	Ref.
				40/4000/200		
				100/1000/1000		
				100/1000/400		
Pt-HGNs	~4.0	~2.75	~5600/100	54/1000/100	1.0 M LiTFSI in TEGDME	87
Ru@MCC	~3.5	~2.8	—	120/1000/400	1.5 M LiNO <sub>3</sub> in DMSO	92
Pt/CNT	~3.8	~2.6	~2500/—	130/1000/2000	1.0 M LiPF <sub>6</sub> in TEGDME	95
Ru@PEG-2	~3.6	~2.8	17 700/200	200/500/200	0.1 M LiClO <sub>4</sub> in DMSO	104
				100/1000/200		
TiC/MWNTs-Ru	~3.5	~2.9	—	90/1000/250	0.5 mol L <sup>-1</sup> LiClO <sub>4</sub> in DMSO	109
PdMo NWs@SWCNTs	~4.2	~2.75	>10 000/100	243/500/300	1.0 M LiTFSI in TEGDME	115
				105/1000/300		
AgPd-3 NTs	~3.4	~2.7	2650/0.2 mA cm <sup>-2</sup>	100/1000/0.2 mA cm <sup>-2</sup>	1.0 M LiCF <sub>3</sub> SO <sub>3</sub> in TEGDME	116
PdCu nanoparticles (PdCu NPs)	~3.7	~2.7	>12 000/200	50/1000/200	1.0 M LiCF <sub>3</sub> SO <sub>3</sub> in TEGDME	117
RuO <sub>2</sub> -Co <sub>3</sub> O <sub>4</sub>	~3.7	~2.9	19 747/200	>100/500/200	1.0 M LiTFSI in TEGDME	120
Fe <sub>SA</sub> -RuO <sub>2</sub> /HPCS	~3.4	~2.8	23 628/200	232/1000/200	1.0 M LiSO <sub>3</sub> CF <sub>3</sub> in TEGDME	121
RuO <sub>2</sub> /HPCS	~3.75	~2.8	19 891/200	134/1000/200		
Fe <sub>2</sub> O <sub>3</sub> /HPCS	~3.8	~2.75	17 004/200	70/1000/200		
IrO <sub>2</sub> /MnO <sub>2</sub>	~4.1	~2.5	16 370/200	312/—/1600	1.0 M LiClO <sub>4</sub> in TEGDME	122
RuO <sub>2</sub> hollow spheres	~3.6	~2.7	1380/100	100/—/500	0.5 M LiClO <sub>4</sub> in DMSO	123
N-doped graphene with encapsulated RuO <sub>2</sub> nanoparticles	~3.7	~2.6	8700/200	>110/2000/400	1.0 M LiTFSI in TEGDME	124
IrO <sub>2</sub> /KB	~3.56	~2.75	4500/0.1 mA cm <sup>-2</sup>	70/500/0.1 mA cm <sup>-2</sup>	1.0 M LiCF <sub>3</sub> SO <sub>3</sub> in TEGDME	125
FeCoNiMnPtIr	~3.34	~2.75	39 100/100	~150/1000/200	1.0 M LiTFSI in TEGDME	218
PtPdIrRuAuAg SNRs	~3.4	~2.8	5252/100	100/1000/500	1.0 M LiSO <sub>3</sub> CF <sub>3</sub> in TEGDME	219
Hollow RuIrFeCoNi nanoparticles	~3.6	~2.8	—	80/4000/2000	1.0 M LiTFSI in DME	220
PtRuFeCoNi HEA@Pt	~3.12	~2.75	8400/100	210/1000/100	1.0 M LiTFSI in TEGDME	221
PtFeCoNiCu@rGO	~3.57	~2.8	13 949/100	148/500/100	1.0 M LiTFSI in TEGDME	222
HEA@Pt-Pt <sub>SAS</sub> -M	~3.2	~2.5	>12 500/200	470/1000/1000	1.0 M LiTFSI in TEGDME	223
MOF-based materials						
N-Fe-MOF	—	—	5300/50	50/~1600/400	1.0 mol L <sup>-1</sup> LiPF <sub>6</sub> in TEGDME	110
Mn-MOF-74	~4.1	~2.75	9420/50	30/1000/250	TEGDME	130
Nickel-hexaminitriphenylene (Ni-HTP)	~3.9	~2.7	18 280/500	150/1000/500	1.0 M LiTFSI in G4	132
NiRu-HTP	~3.63	~2.75	15 080/500	200/1000/500		
ZnO/ZnFe <sub>2</sub> O <sub>4</sub> /C nanocages (ZZFC)	4.05	2.62	11 410/300	15/5000/300	1.0 mol L <sup>-1</sup> LiTFSI in TEGDME	133
Ni-MOFs	~4.0	~2.8	13554.1/500	159/600/500	1 mol L <sup>-1</sup> LiNO <sub>3</sub> in DMSO	134
				93/600/1000		
CoNi-MOFs	~4.0	~2.8	20370.13/200	186/600/500		
				127/600/1000		
				13490.02/1000		
3D printed Co-MOF (3DP-NC-Co)	~3.7	~2.75	1124/0.05 mA cm <sup>-2</sup>	16/1 mA h/0.1 mA cm <sup>-2</sup>	0.5 M LiClO <sub>4</sub> in DMSO	135
				525/0.8 mA cm <sup>-2</sup>		
Fe-UiO-66 <sup>f</sup>	3.56	3.42	~2.5 mA h cm <sup>-2</sup> /0.02 mA cm <sup>-2</sup>	500/—/0.01 mA cm <sup>-2</sup>	1.0 M LiTFSI in TEGDME	136

Default Li-O<sub>2</sub> battery testing atmosphere is pure oxygen unless there is a special comment. The data in Ref. 47, 201 were obtained in (simulated) air atmosphere. <sup>a</sup> The first OER/ORR potential is the potential at half of the cut-off capacity in the fifth column of the table. If there is more than one cut-off capacity, the first OER/ORR potentials correspond to the first cut-off capacity. If there is no cut-off capacity, the first OER/ORR potential is the potential at half of the maximum capacity of the first cycle. <sup>b</sup> The first OER/ORR potential is the potential at half of the cut-off capacity in the fifth column of the table. If there is more than one cut-off capacity, the first OER/ORR potentials correspond to the first cut-off capacity. If there is no cut-off capacity, the first OER/ORR potential is the potential at half of the maximum capacity of the first cycle. <sup>c</sup> The default units of the maximum capacity, rate, and cut-off capacity are in their respective rear brackets. The special cases are labelled particularly. <sup>d</sup> The default units of the maximum capacity, rate, and cut-off capacity are in their respective rear brackets. The special cases are labelled particularly. <sup>e</sup> The default units of the maximum capacity, rate, and cut-off capacity are in their respective rear brackets. The special cases are labelled particularly. <sup>f</sup> Fe-UiO-66 is a photocathode in a photo-assisted Li-O<sub>2</sub> battery; all the data in the row are obtained with light illumination.





**Fig. 3** (a) Schematic synthesis of Ni-Co<sub>3</sub>O<sub>4</sub>-Vo. (b) EPR curves of Ni-Co<sub>3</sub>O<sub>4</sub>-Vo, Ni-Co<sub>3</sub>O<sub>4</sub>, and Co<sub>3</sub>O<sub>4</sub>. (c) High-resolution XPS spectra of Co 2p. (d) High-resolution XPS spectra of O 1s. (e) Partial typical discharge/charge curves of Ni-Co<sub>3</sub>O<sub>4</sub>-Vo during cycling. (f) Cyclic performance of the three cathodes under fast charging and slow discharging conditions (the limited capacity of the battery was set to 500 mAh g<sup>-1</sup>, the charging current density was set to 1000 mA g<sup>-1</sup>, and the discharging current density was set to 100 mA g<sup>-1</sup>). (g) XPS analysis of the Ni-Co<sub>3</sub>O<sub>4</sub>-Vo electrode after discharge and recharge. (a)–(g) Reproduced with permission.<sup>54</sup> Copyright 2025, Elsevier.

compared to Co<sub>3</sub>O<sub>4</sub> and Ni-Co<sub>3</sub>O<sub>4</sub>, the Co 2p<sup>3/2</sup> and Co 2p<sup>1/2</sup> signals of Ni-Co<sub>3</sub>O<sub>4</sub>-Vo show a dramatic shift, which indicates a change in the local environment of the material, probably as a result of the redistribution of charges caused by oxygen vacancies. This charge redistribution may produce an in-built electric field, which can boost the reaction kinetics. Thus, owing to the presence of more surface oxygen vacancies (Fig. 3b and O<sub>2</sub> in Fig. 3d), the LOB with Ni-Co<sub>3</sub>O<sub>4</sub>-Vo cathode showed a better performance with a specific capacity of up to 5275 mAh g<sup>-1</sup>, 337 stable cycles (Fig. 3e) and a “fast-charge-slow-discharge” cycling capability of more than 1400 h (Fig. 3f). Notably, Li substances could not be detected in the Ni-Co<sub>3</sub>O<sub>4</sub>-Vo electrode in the XPS after recharge (Fig. 3g), owing to the excellent catalysis of Ni-Co<sub>3</sub>O<sub>4</sub>-Vo for the decomposition of the discharge products.

Defect/vacancy engineering has been proven to be an effective modulation strategy in metal–air batteries, which is sometimes coupled with other strategies.<sup>5,26,59</sup> Apart from anionic vacancies, cationic vacancies are also common in spinel oxides.

Liu *et al.* synthesized cobalt oxides with cationic vacancies (Co<sub>3-x</sub>O<sub>4</sub>) *via* the thermal treatment of the glycerolatocobalt (GlyCo) nanostructure.<sup>60</sup> At a low temperature of 300 °C in air, the thermal decomposition of its surface functional groups (*e.g.*, Co–O bonds) led to the formation of Co<sup>2+</sup> cation vacancies. The discharge/charge specific capacities of the LOB using the synthesized Co<sub>3-x</sub>O<sub>4</sub> were 14517/13254 mAh g<sup>-1</sup> at a current density of 100 mA g<sup>-1</sup>. These excellent capacity values indicate that the change in the electronic

structure caused by Co<sup>2+</sup> vacancies effectively improved the deposition of Li<sub>2</sub>O<sub>2</sub>.

Due to their wide range of advantages, including high specific surface area, quantum size effect and easy heterostructure engineering with a support, nanomaterials are widely used in energy storage and electrochemistry.<sup>61–63</sup> Zhai *et al.* synthesized Co<sub>3</sub>O<sub>4</sub> nanoparticle evenly dotted hierarchical-assembled carbon nanosheet frameworks (Co<sub>3</sub>O<sub>4</sub>-HCNF) through a simple two-step carbonization–calcination process.<sup>64</sup> Owing to its large BET specific surface area and unique internal structure, the HCNF significantly boosted the electron conduction. Thus, the Li–O<sub>2</sub> battery assembled using the Co<sub>3</sub>O<sub>4</sub>-HCNF cathode showed outstanding ORR/OER capacities (14 901/14 948 mAh g<sup>-1</sup> at a current density of 100 mA g<sup>-1</sup>, respectively) and superior cycling stability and reversibility. Ryu *et al.* used Co<sub>3</sub>O<sub>4</sub> nanofibers fixed on non-oxidized graphene nanoflakes as catalysts,<sup>65</sup> which resulted in a high performance. Liu *et al.* synthesized Pt-doped Co<sub>3</sub>O<sub>4</sub> nanowires hydrothermally on acid-treated carbon paper substrates.<sup>66</sup> These nanowires were closely stacked and displayed an urchin-like morphology. It was found that the doped Pt changed the discharge products from solution-pathway-grown flake-like structures to surface-pathway-grown film-like structures. Then, the tight contact between the film-like discharge products and Co<sub>3</sub>O<sub>4</sub> nanowires was favorable for the OER/ORR kinetics, which led to a low overpotential and high stability.

Heterostructure engineering and crystal plane effects are also widely used strategies for the synthesis of spinels and have been proven to be effective in improving the performance of Li–O<sub>2</sub> batteries.<sup>48–52,67,68</sup> For example, heterostructures such as the Co<sub>2</sub>N/Co<sub>3</sub>O<sub>4</sub> structure optimized the electronic structure of the active sites, which led to an appropriate adsorption energy for LiO<sub>x</sub>, and simultaneously facilitated ORR and OER (Fig. 4b). Furthermore, the highly conductive MXene-based heterostructure accelerated the electron transfer.<sup>67</sup> The XPS spectra showed a shift in the Co<sup>2+</sup> peak to a higher binding energy due to the charge transfer caused by the electron-withdrawing effect (Fig. 4a). Thus, the LOB based on the heterostructure exhibited a higher reversible capacity (14 271 mAh g<sup>-1</sup>), a much lower overpotential (0.65 V) during the first cycle, and more than 300 stable cycles compared to other cathodes (Fig. 4c and d).

Crystal plane effects can cause great differences in the same catalyst material. Co<sub>3</sub>O<sub>4</sub> plates dominantly enclosed by {112} facets were fully covered by the discharge product (Fig. 4e and f), whereas a small amount of discharge product was attached to only the edges of Co<sub>3</sub>O<sub>4</sub> nanocubes with {001} facets as the dominant exposed planes, possibly due to the relatively higher surface energy of the edges.<sup>159</sup> Therefore, Song *et al.* suggested that nucleation sites such as Co<sup>3+</sup> and high surface energy atomic steps seem to be preferential for the growth of Li<sub>2</sub>O<sub>2</sub>. The LOB based on the {112}-faceted Co<sub>3</sub>O<sub>4</sub> plate showed a larger maximum capacity of 9144 mAh g<sup>-1</sup>, a lower overpotential and a greater number of cycles than the {001}-faceted Co<sub>3</sub>O<sub>4</sub> cube. In the case of Co<sub>3</sub>O<sub>4</sub>



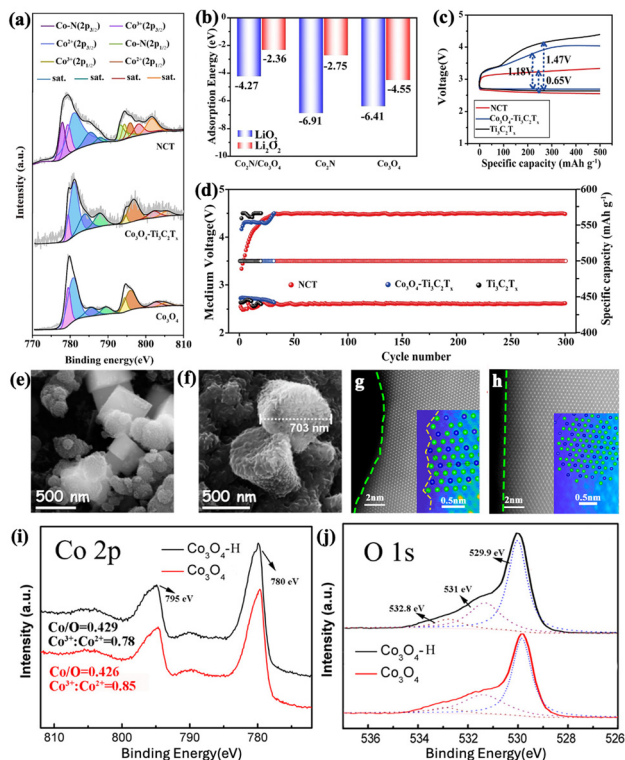


**Fig. 4** (a) High-resolution XPS spectra of Co 2p for NCT,  $\text{Co}_3\text{O}_4\text{-Ti}_3\text{C}_2\text{T}_x$  and  $\text{Ti}_3\text{C}_2\text{T}_x$  materials. (b) Adsorption energy of  $\text{LiO}_2$  and  $\text{Li}_2\text{O}_2$  on different slabs. (c) Discharge-charge curves in the first cycle at  $500 \text{ mA g}^{-1}$  for different cathodes tested in a pure oxygen atmosphere. (d) Cyclability at  $500 \text{ mA g}^{-1}$  for different cathodes tested in a pure oxygen atmosphere. (e) SEM image of the discharged electrode of a {001} faceted  $\text{Co}_3\text{O}_4$  cube. (f) SEM image of the discharged electrode of a {112} faceted  $\text{Co}_3\text{O}_4$  plate. (g and h) Atom states of the edge of  $\text{Co}_3\text{O}_4\text{-H}$  and  $\text{Co}_3\text{O}_4$ , respectively. (i) Co 2p XPS spectra of  $\text{Co}_3\text{O}_4\text{-H}$  and  $\text{Co}_3\text{O}_4$ . (j) O 1s XPS spectra of  $\text{Co}_3\text{O}_4\text{-H}$  and  $\text{Co}_3\text{O}_4$ . (a–d) Reproduced with permission.<sup>67</sup> Copyright 2024, Elsevier B.V. All rights reserved. (e and f) Reproduced with permission.<sup>159</sup> Copyright 2015, the American Chemical Society. (g–j) Reproduced with permission.<sup>160</sup> Copyright 2019, the American Chemical Society.

nanosheets, the nanosheets with an edge-enriched {111} plane (marked as  $\text{Co}_3\text{O}_4\text{-H}$ ) had more atomic steps and kink atoms, and exposed more  $\text{Co}^{2+}$  (the green spheres in Fig. 4g and h) than the poor-edge plane  $\text{Co}_3\text{O}_4$ , which introduced some oxygen vacancy sites, as proven by the XPS spectra Fig. 4i and j, respectively.<sup>160</sup> The more exposed active sites enhanced the electrochemical performance of the  $\text{Li-O}_2$  battery based on  $\text{Co}_3\text{O}_4\text{-H}$  with a lower overpotential, a higher initial capacity and greater cycling stability.

**2.  $\text{ZnCo}_2\text{O}_4$ .** The common morphology of  $\text{ZnCo}_2\text{O}_4$  used in  $\text{Li-O}_2$  cells includes nanoflakes,<sup>177</sup> mesoporous microspheres,<sup>178,179</sup> nanofibers,<sup>180</sup> nanowires<sup>181</sup> and nanoflowers.<sup>182</sup> Mesoporous structures and spin engineering have been emphasized to improve the performance of  $\text{Li-O}_2$  batteries.

$\text{ZnCo}_2\text{O}_4$  was first used as a cathode catalyst in  $\text{Li-O}_2$  batteries by Hung *et al.*<sup>177</sup> The TEM image clearly showed the presence of mesopores in the  $\text{ZnCo}_2\text{O}_4$  nanosheets (Fig. 5a and b). Li *et al.* synthesized 3D ordered mesoporous

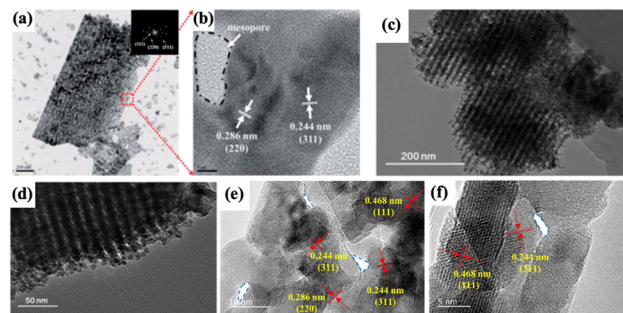


**Fig. 5** (a) TEM micrograph and (b) lattice fringes of 2D mesoporous  $\text{ZnCo}_2\text{O}_4$  NFs. The inset of (a) shows the corresponding SAED pattern. The scale bars of (a) and (b) are 200 nm and 5 nm, respectively. Reproduced with permission.<sup>177</sup> Copyright 2013, RSC. (c and d) TEM images of as-prepared ordered 3D mesoporous  $\text{ZnCo}_2\text{O}_4$ . Reproduced with permission.<sup>178</sup> Copyright 2015, Elsevier. (e and f) HRTEM images of  $\text{NiCo}_2\text{O}_4$ . Reproduced with permission.<sup>181</sup> Copyright 2020, Elsevier.

$\text{ZnCo}_2\text{O}_4$  and its TEM images showed clearly arranged mesopores (Fig. 5c and d).<sup>178</sup> Song *et al.* fabricated  $\text{ZnCo}_2\text{O}_4$  nanowires on carbon cloth, which possessed mesopores (Fig. 5e and f).<sup>181</sup> These mesopores play an essential role in  $\text{O}_2$  diffusion and decide the upper limit of discharge product deposition.

In general, spin engineering involves elevating the spin state of the B ion in  $\text{AB}_2\text{O}_4$  to increase the number of unpaired electrons, which can make the material more active moderately. In the case of  $\text{ZnCo}_2\text{O}_4$ , the low spin state  $\text{Co}^{3+}$  without unpaired electrons ( $t_{2g}^6 e_g^0$ ) cannot trap and interact with the reactants or intermediates. Spin engineering can transform the low spin state  $\text{Co}^{3+}$  into high spin state  $\text{Co}^{3+}$  ( $t_{2g}^4 e_g^2$ ) with four unpaired electrons (Fig. 6a). Ren *et al.* obtained  $\text{ZnCo}_2\text{O}_4$  with high spin state  $\text{Co}^{3+}$  by increasing the calcination temperature.<sup>183</sup> They suggested that the  $\text{Co-O-Co}$  spin tunnel facilitated electron transfer (Fig. 6a). Pan *et al.* introduced  $\text{Cu}^{2+}$  in the tetrahedral sites to partially replace  $\text{Zn}^{2+}$ , and constructed a  $\text{Cu-O-Co}$  spin tunnel (Fig. 6b).<sup>182</sup>

A change in the spin state can adjust the ORR routes (the surface route and the solution route). Ren and coworkers observed a smaller amount of discharge products on  $\text{ZnCo}_2\text{O}_4$  with high spin state  $\text{Co}^{3+}$  (Fig. 7a–f),<sup>183</sup> which indicated that the ORR route changed from the solution route to the surface route. Pan and coworkers detected evenly distributed discharge products, a case between film-like  $\text{Li}_2\text{O}_2$  by the surface route and large-sized  $\text{Li}_2\text{O}_2$  by the solution route, as shown in Fig. 7g.<sup>182</sup>

**3.  $\text{NiCo}_2\text{O}_4$ .**  $\text{NiCo}_2\text{O}_4$  is known to possess core-shell microspherical,<sup>184</sup> sunflower-like,<sup>185</sup> mushroom-like,<sup>186</sup> wave-like,<sup>187</sup> chrysanthemum flower-like,<sup>188</sup> nanowire,<sup>189</sup> nanosheet,<sup>190</sup> waxberry-like,<sup>191</sup> needle-like,<sup>192</sup> urchin-like,<sup>193</sup> foam-like<sup>194</sup> and bowl-like<sup>195</sup> structures.

The development of  $\text{NiCo}_2\text{O}_4$  as an  $\text{Li-O}_2$  cathode catalyst has shifted from focusing on its structure, especially mesopores and porosity in previous studies, to changing its electronic structure through interface engineering,<sup>196</sup> doping engineering,<sup>197,198</sup> heterostructure engineering,<sup>199</sup> amorphization strategy<sup>200</sup> and



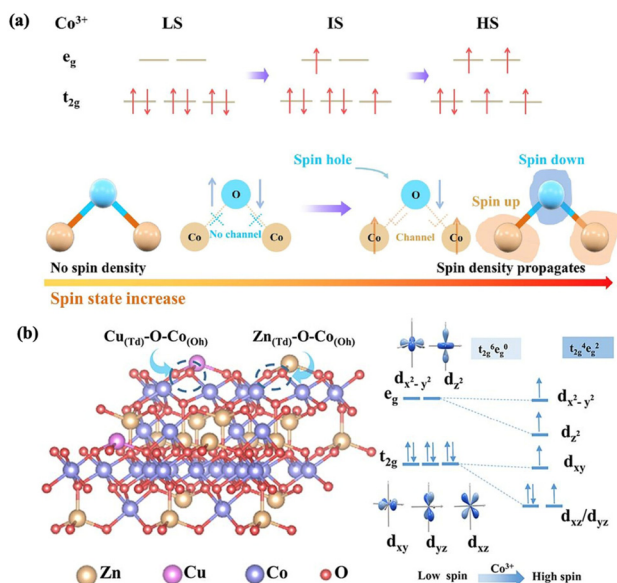


**Fig. 6** (a) Illustration of the different spin configurations of  $\text{Co}^{3+}$  and the formation of Co–O–Co spin channel with an increase in the  $\text{Co}^{3+}$  spin state. Reproduced with permission.<sup>183</sup> Copyright 2023, Elsevier. (b) Illustration of the new co-top oxygen linkage  $\text{Cu}_{(\text{Td})}\text{-O-Co}_{(\text{Oh})}$  and the change in the spin configuration of  $\text{Co}^{3+}$ . Reproduced with permission.<sup>182</sup> Copyright 2023, Elsevier.

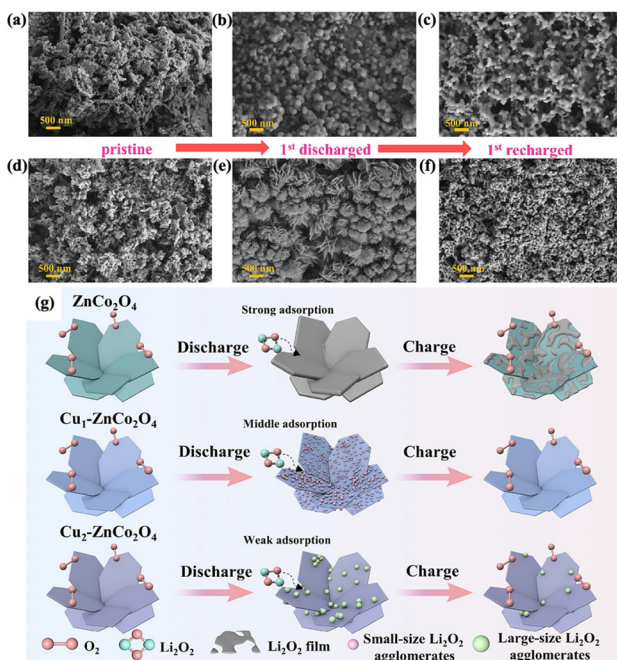


**Fig. 7** SEM images of ZCO-350 electrodes in the (a) pristine state, (b) first discharged and (c) first recharged states. SEM images of ZCO-650 electrodes in (d) the pristine state, (e) first discharged and (f) first recharged states. Reproduced with permission.<sup>183</sup> Copyright 2023, Elsevier. (g) Schematic of the ORR (discharge) and OER (charge) process for  $\text{ZnCo}_2\text{O}_4$ ,  $\text{Cu}_1\text{-ZnCo}_2\text{O}_4$ , and  $\text{Cu}_2\text{-ZnCo}_2\text{O}_4$ . Reproduced with permission.<sup>182</sup> Copyright 2023, Elsevier.

stoichiometry optimization<sup>201</sup> in recent research. These strategies can change the  $\text{Ni}^{3+}/\text{Ni}^{2+}$  ratio and  $\text{Co}^{3+}/\text{Co}^{2+}$  ratio, and obtained

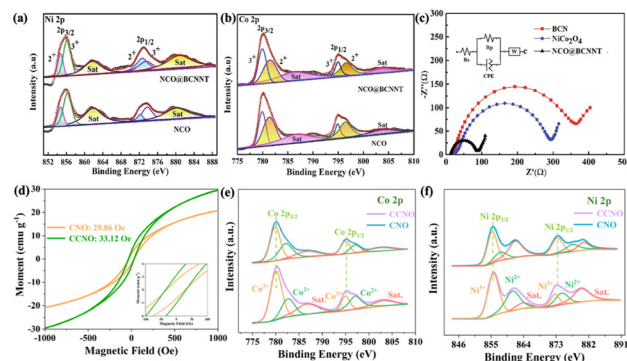


**Fig. 8** High-resolution XPS spectra of (a) Ni 2p and (b) Co 2p. (c) Nyquist plots of batteries in the frequency range of  $10^5$ – $10^2$  Hz. Reproduced with permission.<sup>196</sup> Copyright 2021, Elsevier. (d) Magnetic field dependence of magnetization ( $M-H$ ) profiles of CNO and CCNO at 300 K (the inset shows a partial enlarged image). (e) Co 2p and (f) Ni 2p spectra of CNO and CCNO. Reproduced with permission.<sup>198</sup> Copyright 2022, Elsevier.

catalysts show a better performance, which indicates their improved electronic structure.

Li *et al.* emphasized the improved charge transfer at the interfaces between  $\text{NiCo}_2\text{O}_4$  and boron carbon nitride (BCN) nanotubes.<sup>196</sup> In the case of the composite of  $\text{NiCo}_2\text{O}_4$  and BCN nanocubes (NCO@BCNNT), compared to  $\text{NiCo}_2\text{O}_4$ , a lower  $\text{Ni}^{3+}/\text{Ni}^{2+}$  ratio (1.47 vs. 2.85) and a slightly lower  $\text{Co}^{3+}/\text{Co}^{2+}$  ratio (0.55 vs. 0.62) were observed in its XPS spectra (Fig. 8a and b), respectively. The Nyquist plots showed that the diameter of the hemisphere in the high frequency region of NCO@BCNNT was the smallest among BCN, NCO and NCO@BCNNT (Fig. 8c), which revealed the accelerated electronic transfer in NCO@BCNNT. This was primarily attributed to the change in its electronic structure at the interfaces.<sup>196</sup>

Introducing heterogeneous spin states has been proven to be an effective method for improving the performance of catalysts, which can be detected based on the magnetic field dependence of magnetization ( $M-H$ ) curves.<sup>202</sup> These states are introduced by adding foreign metal ions with a similar atomic size and electronic structure to the crystal lattice, inevitably generating a regional Coulomb force imbalance. Then, this leads to a slight disorder in atomic arrangement in the lattice and exposure of more active sites. Ren *et al.* doped Ce atoms in  $\text{NiCo}_2\text{O}_4$  nanowires and successfully introduced heterogeneous spin states (Fig. 8d).<sup>198</sup> Similarly, they also observed a relatively obvious change in the  $\text{Ni}^{3+}/\text{Ni}^{2+}$  ratio and nearly no change in the  $\text{Co}^{3+}/\text{Co}^{2+}$  ratio (Fig. 8e and f, respectively), in accordance with the study by Li and coworkers.<sup>196</sup> This may be a result of the smaller radius of  $\text{Ni}^{2+}$  and its position in the tetrahedrons, making changes in the  $\text{Ni}^{3+}/\text{Ni}^{2+}$  electronic configuration easier.

It has been reported that amorphous materials provide rich active sites not only on their surfaces but also inside their structure because they possess abundant randomly oriented dangling bonds and unsaturated coordination sites.<sup>203</sup> Xia *et al.* constructed a crystalline  $\text{NiCo}_2\text{O}_4$  (NCO)/amorphous  $\text{Ni}_x\text{P}$  (NP) heterostructure (c/a) catalyst, which



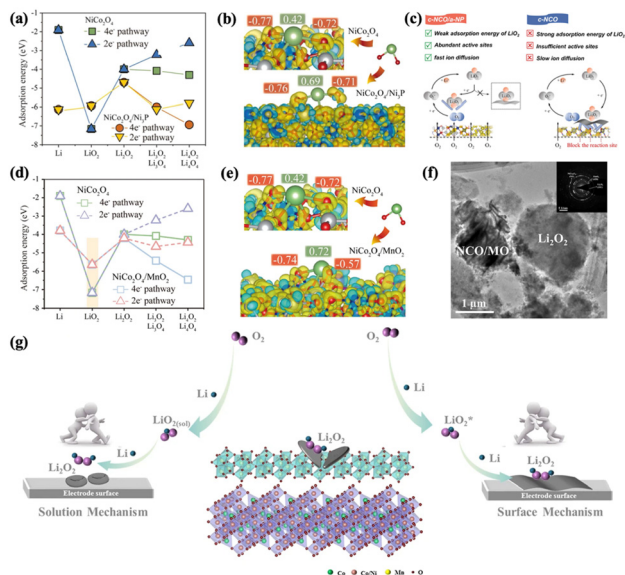


**Fig. 9** (a) Adsorption energies of  $\text{NiCo}_2\text{O}_4$  and  $\text{NiCo}_2\text{O}_4/\text{Ni}_3\text{P}$  for discharge intermediates. (b) CDD and Bader charge for  $\text{Li}_2\text{O}_2$  adsorbed on  $\text{NiCo}_2\text{O}_4$  and  $\text{NiCo}_2\text{O}_4/\text{Ni}_3\text{P}$ , respectively. (c) Schematic reaction mechanism of  $\text{Li}_2\text{O}_2$  generation on the surface of NCO/NP and NCO cathodes. Reproduced with permission.<sup>200</sup> Copyright 2025, Elsevier. (d) Adsorption energy of the discharge intermediates for the  $4e^-$  and  $2e^-$  pathways. (e) CDD and Bader charge for  $\text{Li}_2\text{O}_2$  adsorbed on  $\text{NiCo}_2\text{O}_4$  and  $\text{NiCo}_2\text{O}_4/\text{MnO}_2$ . (f) TEM image of the NCO/MO cathode after deep discharge at  $0.2 \text{ mA cm}^{-2}$  (SAED in insert) with NCO/MO tested as a free-standing air cathode. (g) Schematic reaction mechanism of TP-NCO/MO. Reproduced with permission.<sup>199</sup> Copyright 2024, Yongji Xia *et al.*

could lower the adsorption of  $\text{LiO}_2$  and enhance the adsorption of  $\text{Li}$  (Fig. 9a).<sup>200</sup> In the case of  $\text{LiO}_2$  on NCO/NP,  $\text{Li}^+$  loses more electrons and O receives less electrons (Fig. 9b), weakening the adsorption of  $\text{LiO}_2$ . Therefore,  $\text{Li}_2\text{O}_2$  was deposited on NCO/NP *via* the solution route (Fig. 9c).

Due to the electronic rearrangement at heterostructure interfaces that prompt charge transfer, the Mott–Schottky effect has been applied for the preparation of catalysts for use in Li– $\text{O}_2$ , Li–S, and Li– $\text{CO}_2$  batteries. Recently, Xia *et al.* designed an  $\text{NiCo}_2\text{O}_4/\text{MnO}_2$  heterostructure.<sup>199</sup> Similar to a previous study,<sup>200</sup> this heterostructure exhibited stronger adsorption of Li and weaker adsorption of  $\text{LiO}_2$  (Fig. 9d), and  $\text{Li}^+$  also lost more electrons and O received less electrons (Fig. 9e). After deep discharge at  $0.2 \text{ mA cm}^{-2}$ , chip-like  $\text{Li}_2\text{O}_2$  was observed (Fig. 9f). It was explained that  $\text{Li}_2\text{O}_2$  chips were obtained owing to the competition between the surface route and the solution route (Fig. 9g).<sup>199</sup>

The similarities between these studies reveal the reasons why the intrinsic catalytic activity of  $\text{NiCo}_2\text{O}_4$  is not ideal, including its slow charge transfer, weak adsorption of  $\text{Li}^+$  and too strong adsorption of  $\text{LiO}_2$ . Thus, future studies on  $\text{NiCo}_2\text{O}_4$  can further focus on the exploration of other heterostructures.

### Other transition metals and their compounds

In addition to spinel oxides, single-transition-metal oxides,<sup>57,58,69</sup> transition metal alloys,<sup>70</sup> carbides,<sup>46</sup> phosphides,<sup>47,71</sup> and

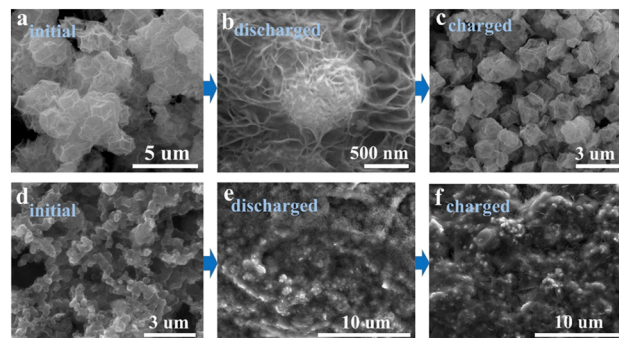


**Fig. 10** SEM images of CoP CPHs (a–c) and commercial CoP (d–f) electrodes in different charging/discharging states; (a and d) initial electrodes, (b and e) after first discharging and (c and f) after first charging. (a–f) Reproduced with permission.<sup>161</sup> Copyright 2021, Elsevier Inc.

sulfides,<sup>45,72,73</sup> which are usually engineered *via* modulation strategies, are potential cathode catalysts in LOBs.

Du *et al.* compared concave polyhedron CoP with exposed (211) crystal planes (CoP CPHs) and CoP polyhedron particles with exposed (011) and (111) crystal planes (commercial CoP).<sup>161</sup> During the first cycle,  $\text{Li}_2\text{O}_2$  on CoP CPHs was completely decomposed (Fig. 10a–c); however, film-like  $\text{Li}_2\text{O}_2$  still remained on commercial CoP (Fig. 10d–f). This indicated that CoP CPHs had better reversibility than the commercial CoP. The CoP-CPH-based LOB exhibited a low overpotential (0.67 V), a maximum discharge capacity of  $33743 \text{ mAh g}^{-1}$  and long cycle life of 950 h due to its large density of atomic steps, edges, ledges, and kink atoms. Wang *et al.* used ultrafine  $\text{Co}_3\text{O}_4$  nanocrystals to decorate atomic-thick  $\text{TiO}_2(\text{B})$  as a highly efficient catalyst,<sup>57</sup> as shown in Fig. 11a. Due to the ion doping effect, oxygen vacancies were induced on  $\text{TiO}_2$  nanosheets by the decoration of  $\text{Co}_3\text{O}_4$  nanocrystals. The existence of these vacancies was proven by XPS, as shown in Fig. 11b, which showed a dramatic shift in the peaks of  $\text{Co}_3\text{O}_4\text{-TiO}_2(\text{B})$  compared to  $\text{TiO}_2(\text{B})$ . Compared to the LOBs with the  $\text{TiO}_2(\text{B})$  electrode with only 70 cycles (Fig. 11c), the LOBs with the  $\text{Co}_3\text{O}_4\text{-TiO}_2(\text{B})$  electrode showed 200 stable and reversible cycles (Fig. 11d). Based on the outcomes, Wang *et al.* proposed the possible mechanism (Fig. 11e), suggesting that the oxygen vacancies and the close contact between  $\text{Li}_2\text{O}_2$  and  $\text{Co}_3\text{O}_4\text{-TiO}_2$  boost the ORR and OER activity. Zheng *et al.* synthesized oxygen vacancy-rich  $\text{TiO}_2$  nanoparticles on  $\text{Ti}_3\text{C}_2\text{Tx}$  MXene ( $\text{V-TiO}_2/\text{Ti}_3\text{C}_2\text{Tx}$ ) nanosheets through HF etching and ethanol-thermal treatment (Fig. 11f).<sup>58</sup> The LOBs with the  $\text{V-TiO}_2/\text{Ti}_3\text{C}_2\text{Tx}$  electrode showed a much lower overpotential (0.21 V) during the first discharge/charge circle in comparison to the  $\text{Ti}_3\text{C}_2\text{Tx}$ - (1.12 V) and  $\text{TiO}_2$ -based (1.45 V) cells (Fig. 11g). The  $\text{V-TiO}_2/\text{Ti}_3\text{C}_2\text{Tx}$ -based LOBs also showed a high specific capacity ( $11487 \text{ mAh kg}^{-1}$ ) and long cycle life (over 200 cycles). Thus, these results not only show the important role of vacancies but also the improved electronic conductivity brought by MXenes, which will be further discussed below.

Single-transition-metal oxides *in situ* decorated on MXenes have been proven to be effective catalysts.  $\text{Ti}_3\text{C}_2\text{Tx}$ , a member



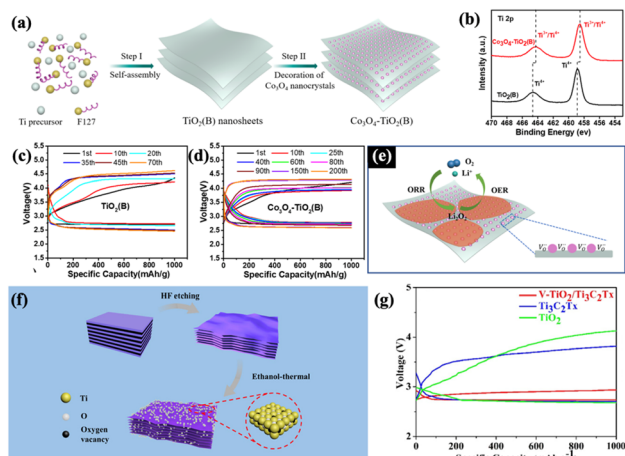


**Fig. 11** (a) Schematic depicting the synthesis of  $\text{Co}_3\text{O}_4\text{-TiO}_2(\text{B})$ . Self-assembly involves a solvothermal process. Decoration of  $\text{Co}_3\text{O}_4$  nanocrystals uses a hydrothermal method. (b) High-resolution XPS spectra of the Ti 2p for  $\text{Co}_3\text{O}_4\text{-TiO}_2(\text{B})$  and  $\text{TiO}_2(\text{B})$ . (c) Cyclic performance of Li– $\text{O}_2$  batteries with the  $\text{TiO}_2(\text{B})$  electrode. (d) Cyclic performance of Li– $\text{O}_2$  batteries with the  $\text{Co}_3\text{O}_4\text{-TiO}_2(\text{B})$  electrode. (e) Schematic of the working mechanism of  $\text{Co}_3\text{O}_4\text{-TiO}_2(\text{B})$  catalysts. (f) Schematic of the procedure for the preparation of V- $\text{TiO}_2/\text{Ti}_3\text{C}_2\text{Tx}$ . HF etching: 4 h in 40% HF at room temperature. Ethanol-thermal: solvothermal synthesis at 140 °C for half of a day. (g) First discharge/charge curves of  $\text{TiO}_2$ -,  $\text{Ti}_3\text{C}_2\text{Tx}$ - and V- $\text{TiO}_2/\text{Ti}_3\text{C}_2\text{Tx}$ -based Li– $\text{O}_2$  batteries with a 1000  $\text{mAh g}^{-1}$  cutoff capacity at 100  $\text{mA g}^{-1}$ . (a)–(e) Reproduced with permission.<sup>57</sup> Copyright 2018, the American Chemical Society. (f) and (g) Reproduced with permission.<sup>58</sup> Copyright 2019, the American Chemical Society.

of the MXene family, was first produced *via* the exfoliation of  $\text{Ti}_3\text{AlC}_2$  in 2011.<sup>74</sup> The MAX phases with the formula  $\text{M}_{n+1}\text{AX}_n$  are layered hexagonal structures, where  $n$  can be 1, 2, or 3.  $M$  is an early transition metal including Ti, Zr, and V.  $A$  is mainly a group IIIA or IVA element, and  $X$  is C and/or N.<sup>58,74,75</sup> By the etching the  $A$  layers from the MAX phases, early transition metal carbides and/or carbonitrides, denoted as MXenes, are produced. Therefore, MXenes are labeled as  $\text{M}_{n+1}\text{X}_n\text{Tx}$ , where Tx represents terminal groups such as  $-\text{OH}$  and  $-\text{F}$ .<sup>58</sup> Considering the fact that there are more than 60 known MAX phases,<sup>74</sup> the potential number of MXenes is huge. Due to their good electronic conductivity and high surface areas, MXenes have been widely used in the energy storage field in LIBs,<sup>76</sup> supercapacitors,<sup>77</sup> and LOBs.<sup>58,69,78</sup> Recently, Xu's group synthesized cationic vanadium vacancy-enriched  $\text{V}_{2-x}\text{O}_5$  on  $\text{V}_2\text{C}$  MXene ( $\text{V}_{2-x}\text{O}_5@/\text{V}_2\text{C}$  MXene) as a bifunctional catalyst for LOBs.<sup>69</sup> The Brunauer–Emmett–Teller (BET) measurement showed the presence of rich mesopores in this material, along with a high surface area, providing mass transfer pathways and active sites for electrochemical reactions. Li *et al.* produced CoO nanoparticle-decorated MXene nanosheets ( $\text{CoO}/\text{Ti}_3\text{C}_2\text{Tx}$ ) as a cathode material for LOBs.<sup>78</sup> Owing to its good electronic conductivity, MXene improved the interface electronic transfer rate. The  $\text{N}_2$  adsorption–desorption analysis showed that the prominent pores were mesopores. The BET results showed that the CoO nanoparticles further improved the

specific surface area. Therefore, the decoration of transition metal oxide nanoparticles on MXenes can combine their individual advantages, showing potential as another effective cathode catalyst in lithium–oxygen batteries.

In conclusion, owing to their advantages such as relatively low cost and natural abundance, transition metals and their compounds have demonstrated significant potential as candidate catalysts for LOBs. These materials are often engineered through modulation strategies to enhance their electrochemical performances as cathode materials in LOBs, including doping engineering, defect/vacancy engineering, crystal plane effects and heterostructure engineering such as decorating them on supports such as MXenes. LOBs with these catalysts have shown improved stability and reversibility, excellent specific energy density, and extended cycle life. Thus, advances in this field will accelerate the commercialization of LOBs.

### Carbon-based materials

As one of the most common cathode catalysts of LOBs, carbon-based materials have advantages including abundant resources, low cost, light weight, structural diversity, high specific surface area, rich pores, and high electronic conductivity.<sup>30,32,79–81</sup> Therefore, they are modified or employed as a support for their wide use as cathode electrodes for Li– $\text{O}_2$  batteries. Carbon-based materials such as carbon black,<sup>31,82</sup> carbon nanotubes (CNTs),<sup>83</sup> carbon nanofibers (CNFs),<sup>84</sup> graphene,<sup>85–87</sup> and carbon foam<sup>88</sup> are commonly utilized. Furthermore, most of these materials can be divided into 1D, 2D, and 3D, among which 1D CNTs/graphene nanotubes (GNTs) and 2D graphene nanosheets/carbon nanosheets (GNSS/CNSSs) are the most commonly used.

Studies have proven that the capacity of Li– $\text{O}_2$  cells largely depends on the pore volume and number of mesopores in their carbon electrode.<sup>89,90</sup> During discharge, oxygen moves to the carbon electrode through the electrolyte in the form of either  $\text{O}_2$  gas or dissolved oxygen.<sup>32</sup> The cathode reactions take place at the interface among the solid electrode, the electrolyte and the  $\text{O}_2$  gas phase, where  $\text{Li}^+$  and  $\text{O}_2$  meet and eventually form  $\text{Li}_2\text{O}_2$ . Micropores are too small to allow the deposition of more  $\text{Li}_2\text{O}_2$  because they become blocked and their small sizes make the diffusion of oxygen difficult. Conversely, macropores reduce the volume efficiency. The solid–liquid–gas tri-phase regions possess less macropores, which leads to the lower production of  $\text{Li}_2\text{O}_2$ .<sup>32</sup>

Besides mesopores, macropores with the appropriate size also play a role in carbon materials. Ding *et al.* found that at the discharge current of 0.1 mA, the cell capacity increased with an increase in pore size and peaked at the pore size of 80 nm.<sup>91</sup> This indicates that small macropores also play an important role in oxygen diffusion and  $\text{Li}_2\text{O}_2$  deposition.

Therefore, the synthesis of mesoporous and/or small macroporous carbon materials is the key to improving the capacity of LOBs. Yang *et al.* prepared mesocellular carbon



foam (MCF-C) *via* nanocasting technology using a mesocellular foam (MCF) silica hard template.<sup>88</sup> The MCF-C showed clear spherical pores of the same size, whose inner diameter was about 28 nm and outer diameter was about 35 nm, as shown in Fig. 12b. Sun *et al.* reported the preparation of mesoporous carbon nanocubes with numerous hierarchical mesopores and macropores.<sup>92</sup> The TEM images (Fig. 12c and d) showed the presence of many interconnected mesopores. The N<sub>2</sub> adsorption-desorption plots of MCCs showed that large-size pores accounted for most of the pore volume, and the inset indicated that the pore sizes were mainly about 50 and 100 nm (Fig. 12a). Guo's group reported the synthesis of three-dimensional ordered mesoporous and macroporous carbon sphere arrays (MMCSAs).<sup>93</sup> These carbon spheres were hexagonal, with a diameter of about 200 nm, and possessed interstices of about 60 nm between them (Fig. 12e). Fig. 12f shows that the mesopores had a size of approximately 8 nm and a wall thickness of 3 nm. Sakaushi *et al.* produced mesoporous noble carbons that were N-doped and showed astonishing oxygen stability.<sup>94</sup> The TEM images (Fig. 12g and h) and pore size distribution (Fig. 12i) graphs showed that this material had a mesoporous structure with an average pore diameter of about 8 nm. The mesopores and small macropores in this material not only promoted O<sub>2</sub>

diffusion and facilitated Li<sup>+</sup> diffusion to the cathode immersed in electrolyte but also provided enough space for Li<sub>2</sub>O<sub>2</sub> deposition.

Besides possessing richly designed mesopores and/or small macropores, CNTs/CNFs have high surface areas, which can provide many more active sites. Through structure design by using chemical vapor deposition (CVD), Lim *et al.* synthesized hierarchical carbon electrodes with highly aligned CNT fibrils, as shown in Fig. 13a and b.<sup>95</sup> The hierarchical porous structure avoided blocking by the discharge products and was strong enough to remain stable after 100 cycles. Mitchell *et al.* fabricated CNF electrodes *via* atmospheric pressure CVD on porous anodized aluminum oxide (AAO) substrates coated with thin layers of Ta and Fe (Fig. 13c and d).<sup>163</sup> The hollow CNFs were almost vertical, while the substrate surface was horizontal. Due to their low carbon packing and void volume, a high gravimetric energy density of ~2500 Wh kg<sup>-1</sup> at a power of up to ~100 W kg<sup>-1</sup> was achieved.

N-doping engineering is one of the most popular methods to promote the performance of CNTs. N atoms can form five main doping structures, including pyridinic N, amine N, pyrrolic N, quaternary N and oxidized N with binding energies of 398–399 eV, 399–400 eV, 400–401 eV, 401–402 eV and 402–405 eV, respectively.<sup>96,97</sup> Among them, pyridinic N seems to play a vital role in changing the structure of CNTs.<sup>98</sup> Chen's group revealed the effects caused by doped Ni in

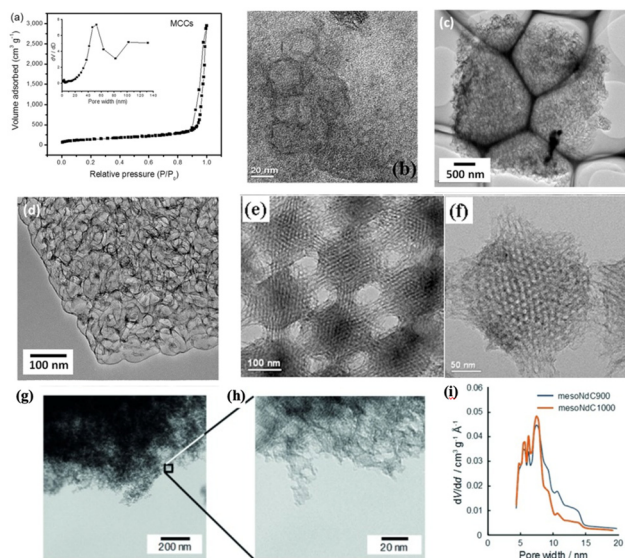


**Fig. 12** (a) Nitrogen adsorption/desorption isotherms and pore-size distribution of the MCCs. Reproduced with permission.<sup>92</sup> © 2015, WILEY-VCH Verlag GmbH & Co. KGaA, Weinheim. (b) TEM image of the MCF-C. Reproduced with permission.<sup>88</sup> Copyright 2009, Elsevier. (c) Low-magnification and (d) high-magnification TEM images of the MCCs. Reproduced with permission.<sup>92</sup> © 2015, WILEY-VCH Verlag GmbH & Co. KGaA, Weinheim. (e and f) TEM images at different magnifications. Reproduced with permission.<sup>93</sup> © 2013, WILEY-VCH Verlag GmbH & Co. KGaA, Weinheim. (g and h) TEM images of the meso-NdCs. Reproduced with permission.<sup>94</sup> © 2015, WILEY-VCH Verlag GmbH & Co. KGaA, Weinheim. (i) Pore size distributions of meso-NdCs. Reproduced with permission.<sup>94</sup> © 2015, WILEY-VCH Verlag GmbH & Co. KGaA, Weinheim.

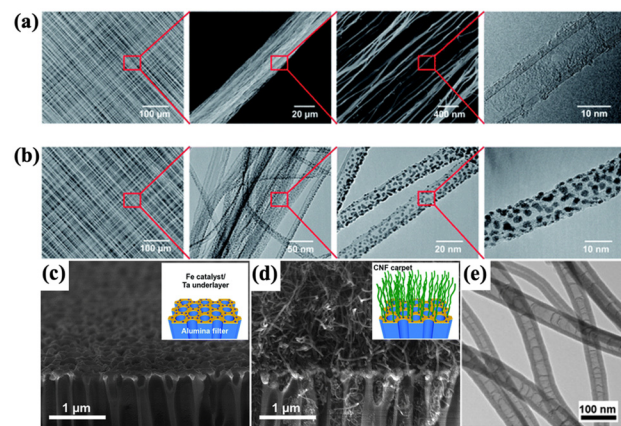


**Fig. 13** (a) SEM images at various magnifications of the CNT electrode before Pt coating and TEM image of a single CNT. (b) SEM and TEM images at various magnifications of the Pt/CNT electrode after Pt coating. (c) Cross-sectional (70°-tilt) SEM micrograph of the porous anodized aluminium oxide (AAO) filter after thin film deposition using electron beam evaporation. Inset: Schematic representation of the electrode after the deposition of metal thin films (Ta 30 nm, Fe 2 nm) on one side of the AAO filter. (d) Cross-sectional (70°-tilt) SEM image of the AAO filter after nanofiber growth. Inset: Schematic representation of the electrode after the catalyzed growth of carbon nanofibers. (e) TEM image of N-CNTs. (a and b) Reproduced with permission.<sup>95</sup> Copyright 2013, the Royal Society of Chemistry. (c and d) Reproduced with permission.<sup>163</sup> Copyright 2011, the Royal Society of Chemistry. (e) Reproduced with permission.<sup>99</sup> Copyright 2011, Elsevier B.V. All rights reserved.



CNTs.<sup>97</sup> They synthesized CNTs and N-doped CNTs (CNx) *via* the floating catalyst chemical vapor deposition (FCCVD) method. The TEM images showed that CNx possessed a bamboo-like structure, with kinks along the tubes and abundant surface defects. The XPS spectra showed that N-doping was successful and the N atoms were mainly pyridinic, graphitic, and oxidized nitrogen. By comparing the rotating ring-disk electrode (RRDE) tests for ORR using Pt/CNTs and Pt/CNx, they found that the electrochemical active area of Pt/CNx was 1.6 times greater than that of Pt/CNTs and the specific activity of Pt/CNx was 1.34 times higher than that of Pt/CNTs. Thus, N-doping increases the electrochemical active area and promotes the intrinsic electrocatalytic activity toward ORR.

Li *et al.* first used N-doped CNTs (N-CNTs) as a cathode material for Li-O<sub>2</sub> cells.<sup>99</sup> The TEM plots showed that N-CNTs possessed typical bamboo-like structures (Fig. 13e), in accordance with previous research.<sup>97</sup> The N atoms improved the performance of N-CNTs, the specific discharge capacity of which was 1.5 times higher than that of CNTs. Further, Lin *et al.* synthesized binder-free nickel foam-supported nitrogen-doped carbon nanotubes (N-CNTs@Ni) using the FCCVD method to avoid the decomposition of the binder and consequent formation of LiF (Fig. 14a-d).<sup>164</sup> The binder-free material improved the capacity (1814 mAh g<sup>-1</sup> at

0.05 mA cm<sup>-1</sup>, more than 2 times the capacity of the N-CNT-based Li-O<sub>2</sub> cells) and rate performance of the Li-O<sub>2</sub> cells.

Heterostructure engineering is another common method employed for the modulation of CNTs/CNFs. Kim *et al.* synthesized pyrochlore LaSrSn<sub>2</sub>O<sub>7</sub> nanoparticles (LSSO NPs) anchored on CNFs (C@LSSO NFs) as bifunctional catalysts (Fig. 14e).<sup>100</sup> Compared to LSSO NPs and KB, the C@LSSO-NFs-based Li-O<sub>2</sub> batteries had a lower overpotential (1.01 V) and higher round-trip efficiency (72.6%), which could be attributed to the synergistic effect of the intrinsic activity of LSSO NPs and electronic conductivity of CNFs. To avoid parasitic reactions, Jian's group designed a core-shell-structured CNT@RuO<sub>2</sub> catalyst to prevent direct contact between carbon and the electrolyte, as shown in Fig. 14f and h.<sup>108</sup> The RuO<sub>2</sub> shell had a thickness of about 4 nm and could effectively wrap CNTs (Fig. 14h). The CNT@RuO<sub>2</sub>-based Li-O<sub>2</sub> cells showed a low overpotential of 0.71 V and a high round-trip efficiency of about 79%, which can be attributed to the electronic conductivity of CNFs and high OER catalytic activity of RuO<sub>2</sub>.

2D CNSs/GNSs are also promising materials for application in the energy storage field due to their high surface areas and unique structures. Li *et al.* first used GNSs as a cathode material for Li-O<sub>2</sub> cells.<sup>85</sup> Compared to two other carbon materials, BP-2000 and Vulcan XC-72, GNSs possessed much more unsaturated carbon, which was active in reacting with O<sub>2</sub>, and consequently led to higher ORR activity, and more mesopores with a size in the range of 2 nm and 20 nm. At a current density of 75 mA g<sup>-1</sup>, GNSs showed a much higher energy density (8705.9 mAh g<sup>-1</sup>) than BP-2000 (1909.1 mAh g<sup>-1</sup>) and Vulcan XC-72 (1053.8 mAh g<sup>-1</sup>). Then, Li *et al.* used N-doped GNSs (N-GNSs) that possessed defects and functional groups including C-O, C=O, and O=C-O, which led to a better electrocatalytic performance for ORR and a higher discharge capacity of 11660 mAh g<sup>-1</sup> because the discharge products prefer to grow around the defective sites with functional groups according to density functional theory (DFT) calculation.<sup>101</sup> This was verified by the Tafel plots of N-GNSs and GNSs, with N-GNSs showing a smaller Tafel tangent than GNSs and 0.99 and 0.80 electrons transferred in ORR, respectively. Compared to GNSs, smaller-sized discharge products were observed on N-GNSs (Fig. 15a and b, respectively). In addition, Li's group explored the effects of S doping on GNSs.<sup>102</sup> However, the effects of S doping were not ideal because of the much lower discharge capacity (4300 mAh g<sup>-1</sup>) than GNSs and other ordinary performance indexes.

N-doped GNS/CNS-based composites with transition metal or transition metal oxide nanostructures have been proven to be effective catalysts for Li-O<sub>2</sub> cells. For example, Wang *et al.* embedded Co nanoparticles in N-doped CNSs and found that the Co-N<sub>4</sub> active sites improved the OER performance, as illustrated in Fig. 15c.<sup>103</sup> The Li-O<sub>2</sub> cell with this material achieved a low overpotential of 0.40 V, a high-rate discharge capacity of 11 098 mAh g<sup>-1</sup> at 1 A g<sup>-1</sup>, and excellent cyclability of 260 cycles at 400 mA g<sup>-1</sup>. Sun *et al.* added Ru nanocrystals

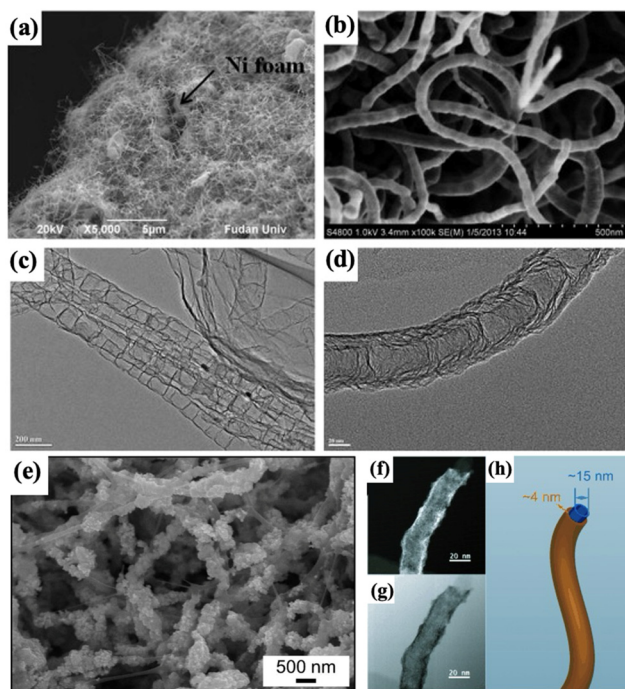


**Fig. 14** (a and b) SEM images and (c and d) TEM images of the N-CNT@Ni electrode. Reproduced with permission.<sup>164</sup> Copyright 2013, Elsevier B.V. All rights reserved. (e) Typical SEM images of C@LSSO NFs. Reproduced with permission.<sup>100</sup> Copyright 2023, Jong Guk Kim, Yuseong Noh, Youngmin Kim. Published by Elsevier Ltd. (f) HAADF-STEM and (g) BF-STEM images of a single CNT@RuO<sub>2</sub> structure (space bar: 20 nm). (h) Schematic of a single CNT@RuO<sub>2</sub> structure. (f-h) Reproduced with permission.<sup>108</sup> Copyright 2014, WILEY-VCH Verlag GmbH & Co. KGaA, Weinheim.



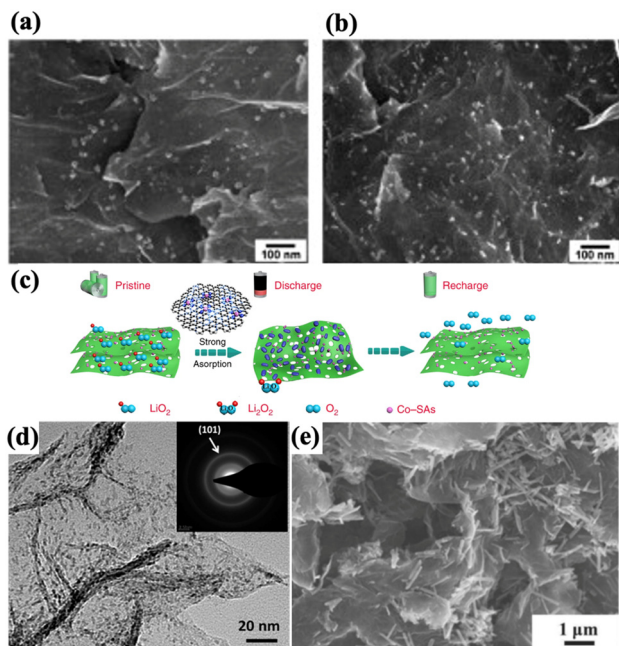


**Fig. 15** (a) GNS and (b) N-GNS electrodes discharged for 1 h. reproduced with permission.<sup>101</sup> Copyright 2012, Elsevier B.V. All rights reserved. (c) Schematic of the working mechanism of the Co-SA/N-C electrodes. Reproduced with permission.<sup>103</sup> Copyright 2022, Peng Wang *et al.* (d) TEM image of Ru@PGE-2 and its SAED pattern (inset). Reproduced with permission.<sup>104</sup> Copyright 2014, the American Chemical Society. (e) SEM image of MnO<sub>2</sub> NT/NExG composite electrode. Reproduced with permission.<sup>105</sup> Copyright 2012, Electrochemical Society.

to porous graphene oxide (Ru@nanoporous graphene), as shown in Fig. 15d, and found that the Ru nanocrystals could accelerate OER.<sup>104</sup> Consequently, the Ru@nanoporous-graphene-based Li–O<sub>2</sub> cells showed a low overpotential of *ca.* 0.355 V, a high reversible capacity of 17700 mAh g<sup>-1</sup>, and long cycling life of 200 cycles at a limited capacity of 1000 mAh g<sup>-1</sup>. Park *et al.* combined N-doped thermally exfoliated graphene (NExG) with  $\alpha$ -MnO<sub>2</sub> nanotubes (NTs) to form NExG/ $\alpha$ -MnO<sub>2</sub> NTs as a cathode material.<sup>105</sup> Owing to the defective sites caused by N doping and the thin 2D structure of NexG (Fig. 15e), the ORR was improved dramatically, with a max power density 32% larger than that of the MnO<sub>2</sub>-NT/Vulcan-carbon-based Li–O<sub>2</sub>.

In summary, various types of carbon materials have been employed as cathode catalysts for Li–O<sub>2</sub> batteries, primarily due to their low cost and good electronic conductivity. Nevertheless, the instability of carbon materials impedes their practical application in Li–O<sub>2</sub> batteries. McCloskey *et al.* first reported that Li<sub>2</sub>O<sub>2</sub> (or LiO<sub>2</sub>) could react with ether electrolyte or carbon cathodes to form Li<sub>2</sub>CO<sub>3</sub> and other carbonates, which led to a high overpotential and poor cycle life.<sup>106</sup> The research by Gallant's group's on the chemical and morphological changes in vertically aligned carbon nanotube electrodes also confirm this.<sup>107</sup> Further, Thotiyl *et al.* found that above 3.5 V (*vs.* Li/Li<sup>+</sup>), carbon tended to oxidatively decompose to Li<sub>2</sub>CO<sub>3</sub> and lithium carboxylates (HCO<sub>2</sub>Li and

CH<sub>3</sub>CO<sub>2</sub>Li), while under 3.5 V (*vs.* Li/Li<sup>+</sup>), carbon was relatively stable. However, carbon catalyzing the degradation of the electrolyte is inevitable.<sup>16</sup> In addition, as mentioned before, <sup>1</sup>O<sub>2</sub> may exacerbate carbon erosion. Faced with these problems, even many well-designed carbon materials have poor stable cycle lives (typically <100 cycles without severe capacity losses).<sup>108–110</sup> Thus, increasing the stability of carbon and finding electrolytes that can coexist with carbon materials without degradation reactions are the key to carbon-based Li–O<sub>2</sub> batteries.

### Noble metals, their alloys and oxides

Compared to carbon materials, which have low catalytic activity and subject to erosion by superoxide radicals and parasitic reactions that produce Li<sub>2</sub>CO<sub>3</sub> and lithium carboxylates, the most commonly used noble metals (Au, Ag, Ru, Pt, Ir, and Pd) and their alloys and oxides (for example, RuO<sub>2</sub> and IrO<sub>2</sub>) in Li–O<sub>2</sub> cells are much higher catalytic activity, despite the fact that the electronic conductivity of noble metal oxides is inferior to that of carbon materials in general. Therefore, noble metals and their alloys and oxides have been widely explored as cathode catalysts for Li–O<sub>2</sub> cells in labs.

It is acknowledged that the Sabatier principle is useful in heterogeneous catalysis related to noble metals and alloys, which suggests that the interactions between the intermediates and the catalyst should be moderate, not too strong or weak. Conversely, the d-band model suggests that electrons in the s band are important but not decisive to adsorption; however, the electronic states of the d-band of each metal are different and the widths of the d-band of diverse metals vary. Also, the position of the d-band center varies in different metals. In general, if the d-band center is high, which means it is close to the Fermi level, the adsorption of intermediates by noble metals will be strong; the adsorption will be weak if the d-band center is low. The position of d-band center determines the adsorption energy (sometimes also called the binding energy). Therefore, adsorption is mainly determined by the electronic states of the d-band. It has been proven that a universal volcano-like relationship exists between the adsorption energy and catalytic activity, regardless of the reactants.<sup>217</sup> Thus, the d-band model can be used to explain the catalytic activity of catalysts based on the Sabatier principle.

**Noble metals.** The adsorption energy for oxygen on the surface of polycrystalline noble metals has been found to influence their Li<sup>+</sup>-ORR activity, and the nonaqueous Li<sup>+</sup>-ORR potentials and oxygen adsorption energies of different noble metals show a volcano-dependent relationship.<sup>111</sup> Based on the Sabatier principle, the ORR potential is the largest when the oxygen adsorption energy is moderate. The ORR potential decreases with too strong or weak oxygen adsorption. This means that Li–O<sub>2</sub> batteries exhibit a better performance with a suitable oxygen adsorption energy. The Li<sup>+</sup>-ORR activity follows the order of Pd > Pt > Ru  $\approx$  Au on bulk surfaces.



In the case of OER activity, the d-band model has been proven to be effective in explaining heterogeneous catalysis and electrochemistry.<sup>112</sup> Noble metals have controllable d-band conditions, which can manipulate the interactions between them and the intermediates during the OER.<sup>98</sup> As mentioned before, the intensity of the adsorption also needs to be moderate for a better catalysis performance. Further, the changes in the surface structures of noble metals also play a vital role in their OER activity. Thus, these two main factors should be considered simultaneously. For example, the calculated overpotential for Pt{111} is reported to be 1.62 V,<sup>36</sup> possibly due to the strong adsorption of intermediates by Pt{111}.<sup>37,38</sup> Song *et al.* found that the high index {411} has a larger surface energy, and therefore stronger adsorption than {111}, showing a lower OER overpotential of 1.20 V,<sup>36</sup> which seemed contradictory to the d-band model. However, the rough facet with atomic steps provides high-density atoms on the step edge, kink, and ledge as active sites (Fig. 16a–d). The overall influence of these two factors makes the {411} facets more active than other facets, with a much lower overpotential of 0.51 V (Fig. 16e).

Su *et al.* researched the variable index facets of Au and found that the {441} high-index facet has a high density of stepped surface atoms compared with the {111} facet, as

shown in Fig. 16f.<sup>41</sup> Cubic gold (Au) NCs enclosed by {100} facets, truncated octahedral Au NCs enclosed by {100} and {110} facets, and trisoctahedral (TOH) Au NCs enclosed by 24 high-index {441} facets loaded on Super-P (SP), respectively, were tested in Li–O<sub>2</sub> cells (Fig. 16g). Among them, it was found that TOH Au NCs@SP showed the lowest overpotential of 0.95 V and the largest discharge capacity of 20 298 mAh g<sup>-1</sup>. DFT calculations showed that the reaction energy between the Au, Li, and O atoms decreases as the surface energy increases. The high index {441} facet has the highest surface energy of 2.55 J m<sup>-2</sup> and the lowest reaction energy with Li and O atoms (1.64 J m<sup>-2</sup>). The results of this work indicated that the high index facet of the same noble metal has stepped atoms with higher catalytic activity, in accordance with the research by Song's group.

**Traditional alloys.** Alloying can also change the d-band conditions of noble metals, and the substrate metal causes d-band shifts in the overlayer of another noble metal.<sup>112,113</sup> Therefore, pairing different noble metals may improve the catalytic activity of one or both metals. The ORR activity on noble metal alloys has been explored by Sankarasubramanian's group, and they expected that the dopants on the surface could provide better binding sites and lead to the “ligand effect”, which means that the d-bands of the two metals overlap and the electron density in their d-bands changes.<sup>114</sup> They also found that the nucleation of Li<sub>2</sub>O<sub>2</sub> seems to preferentially occur on interstitial face-centered cubic (FCC) and hexagonal-closed packed (HCP) sites. Pt<sub>3</sub>Ni, Pt<sub>3</sub>Co, and Pd<sub>3</sub>Fe were expected to be high-performance Li–O<sub>2</sub> catalysts based on *ab initio* DFT modeling and an electrode kinetic model based on the collision theory.<sup>114</sup> However, to the best of our knowledge, there is no report on the use of Pt<sub>3</sub>Ni and Pt<sub>3</sub>Fe as Li–O<sub>2</sub> cathode materials thus far.

Interestingly, an earlier work about Pt<sub>3</sub>Co reported that the introduction of Co atoms could change the electron states of Pt and reduce the  $\eta_{\text{OER}}$  of Pt{111} from 1.62 V to 1.13 V (Fig. 17a–c).<sup>37</sup> The DFT calculations suggested that the reduction in  $\eta_{\text{OER}}$  was related to the decrease in the adsorption strength of LiO<sub>2</sub> on the outermost Pt catalytic sites, with the LiO<sub>2</sub> adsorption strength changing from 3.65 eV to 3.01 eV, which helped prove the reasonability of the former study.<sup>114</sup>

Due to its outstanding ORR catalytic activity among the noble metals, Pt is often alloyed with other noble or transition metals. PtAu nanoparticles were confirmed to be an efficient Li–O<sub>2</sub> catalyst.<sup>39</sup> PtAu/C had an average charge potential of 3.6 V, which is slightly lower than that of Pt/C and much lower than that of Au/C. Also, the discharge potential of PtAu/C was slightly lower than that of Au/C and much lower than that of Pt/C (Fig. 17d). Thus, the results suggested that the surface Au and Pt atoms of bifunctional PtAu are primarily responsible for its ORR and OER kinetics in Li–O<sub>2</sub> cells, respectively. PtAu alloy has been further explored by designing the  $e_g$  occupancy of Pt to alter its overpotentials.<sup>35</sup> Compared to PtRu, PtAu had a smaller  $e_g$  occupancy, which indicated that the number of  $e_g$  electrons

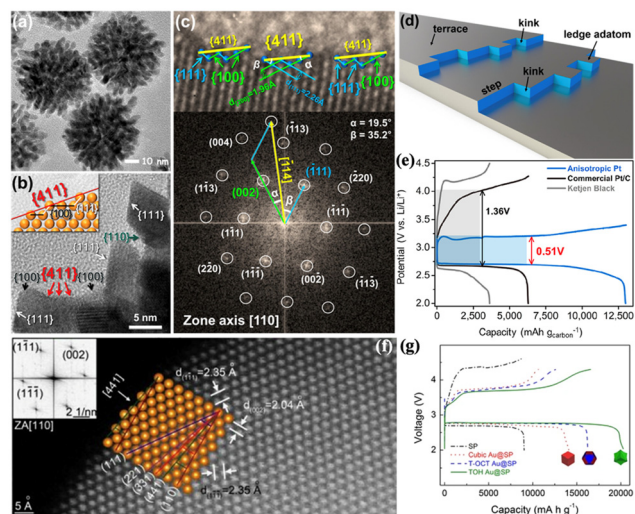


**Fig. 16** (a) TEM and (b) HRTEM images of the anisotropic Pt catalysts. The inset of (b) is an atomic model of the {411} facets exposed on the surface of the anisotropic Pt catalysts. (c) Enlarged HRTEM image and corresponding FFT pattern. (d) Schematic of the atomic steps on the high-index facet. (e) Charge–discharge curves of the cubic Au NCs@SP (red solid line), T-OCT Au NCs@SP (blue solid line), TOH Au NCs@SP (green solid line) and bare SP electrodes (black solid line) at 100 mA g<sup>-1</sup> in the first cycle. (a–e) Reproduced with permission.<sup>36</sup> Copyright 2018, the American Chemical Society. (f–g) Reproduced with permission.<sup>41</sup> Copyright 2015, Dawei Su *et al.*



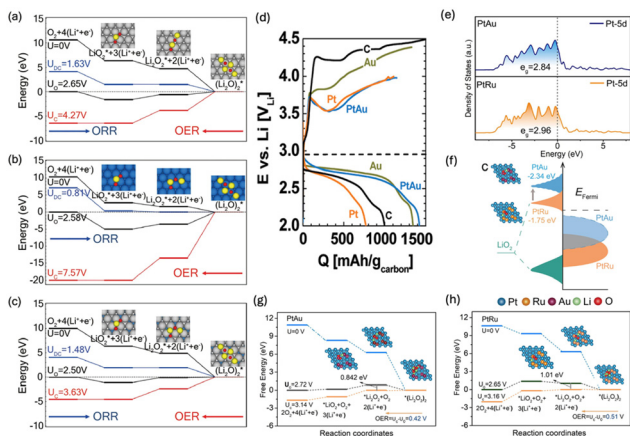


**Fig. 17** Calculated energy diagrams for Li-ORR/OER on (a) Pt(111), (b) Co(0001), and (c) Pt<sub>3</sub>Co(111), along with the optimized structures of Li<sub>x</sub>O<sub>2</sub> ( $x = 1, 2$  and  $4$ ) adsorbed on the surfaces. (d) First discharge/charge profiles of carbon at 85 mA g<sub>carbon</sub><sup>-1</sup> and of Au/C, Pt/C, and PtAu/C at 100 mA g<sub>carbon</sub><sup>-1</sup> in an Li–O<sub>2</sub> cell. Reproduced with permission.<sup>39</sup> Copyright 2010, the American Chemical Society. (e) The PDOS of Pt 5d orbitals for PtRu and PtAu catalysts. (f) Schematic of the bond formation between the adsorbate (LiO<sub>2</sub>) valence bands and the d states of PtM (M = Au and Ru). From PtRu to PtAu, the upshift in the d-band center elevates the corresponding antibonding orbits. (g) and (h) Free energy curves at various potentials for PtAu (g) and PtRu (h) cathodes. The embedded graphics in (g) and (h) show the refined crystal structures of the PtAu and PtRu catalysts with specific adsorbates at the corresponding steps. (a–c) Reproduced with permission.<sup>37</sup> Copyright 2014, Byung Gon Kim *et al.* (e–h) Reproduced with permission.<sup>35</sup> © 2022, Wiley-VCH GmbH.

in PtAu (2.84) was less than that in PtRu (2.96) and led to an increase in the d-band center (Fig. 17e and f), thus enhancing its adsorption of LiO<sub>2</sub>. The Gibbs free energies for the two catalysts were calculated during the OER processes. The energy barrier of PtAu (0.842 eV) was less than that of PtRu (1.01 eV) because of the stronger adsorption of LiO<sub>2</sub> on PtAu. Therefore, the calculated OER overpotential of PtAu was smaller than that of PtRu (Fig. 17g and h), respectively, in accordance with the experiment.

In addition, PtIr alloy has been researched for use in high-performance Li–O<sub>2</sub> cells.<sup>38</sup> Multipod-like PtIr was synthesized with a length of *ca.* 45 nm and a width of *ca.* 10 nm. At 1 mA g<sup>-1</sup> when the capacity was set to 1000 mAh g<sup>-1</sup>, the PtIr multipods displayed much lower OER and ORR overpotentials of 0.33 V and 0.11 V, respectively, than that of Pt nanocrystals (1.02 V and 0.17 V). Due to the higher electronegativity of Pt than Ir, the charge state of Pt becomes more negative, leading to lower Lewis acidity. The Pt atoms with higher electron density and lower Lewis acidity showed weaker adsorption for LiO<sub>2</sub> because of the downshift in the Pt d-band center. Other alloys have also been explored as Li–O<sub>2</sub> catalysts, such as AgPd and PdCu.<sup>115–117</sup>

**High-entropy alloys.** Furthermore, as emerging materials in the past two decades,<sup>213</sup> high-entropy alloys (HEAs) have been used in many fields including catalysis.<sup>214,215</sup> Quite different from traditional alloys, which typically contain one or two types of metal atoms, HEAs are defined based on their

composition as alloys that consist of at least 5 principal elements with the near-equimolar concentration of each in the range of 5% to 35%, sometimes with other minor elements.<sup>213</sup> Therefore, the combinations of the principal elements and their concentrations can be numerous, resulting in a vast number of HEAs. High-entropy alloys mainly form substitutional solid solutions that have FCC, HCP or body-centered cubic (BCC) structures instead of intermetallic compounds.<sup>216</sup> The presence of multiple elements and complex interactions between them endow HEAs with unique traits, including the high-entropy effect, lattice distortion effect, slow diffusion effect and “cocktail” effect. It has been widely acknowledged that the high-entropy effect and slow diffusion effect are favorable to enhance the stability of HEAs, and the structural defects caused by the lattice distortion effect and complex synergistic effects caused by the “cocktail” effect are responsible for the effective catalytic activity of designed HEAs.<sup>214–216</sup> However, these four effects are not divided, and among them, the high-entropy effect is the basis.

Recently, high-entropy materials (HEMs) have been used as Li–O<sub>2</sub> catalysts, including HEAs, high-entropy oxides, and high-entropy sulfides.<sup>215</sup> In this part, we only focus on HEAs.

Based on the Sabatier principle and the tunable d-band structure of HEAs due to the high entropy effect, Tian *et al.* used several HEAs to explore the detailed mechanism of their d-band structure and catalytic activity.<sup>218</sup> The positions of the d-band center are shown in Fig. 18a, with the sequence from high to low being HEA > PtIr > HEAPtIr > HEAIr > HEAPt (here, HEA is FeCoNiMn alloy), which indicates that the order of the adsorption energies for the intermediates also follows this trend. Then, the five catalysts were tested in Li–O<sub>2</sub> cells. As expected, the HEAPtIr-based LOB exhibited a super low OER overpotential of 0.38 V (Fig. 18b), which is much lower than that of the other four catalysts. Furthermore, though DFT calculations, the order of the binding energies for LiO<sub>2</sub> and Li<sub>2</sub>O<sub>2</sub> corresponds to the positions of the d-band centers and the conversion efficiency shows a volcano-like relationship with the binding energy (Fig. 18c and d). As shown in Fig. 18e and f, when the d-band center is too high, the energy of the antibonding orbital is higher than the Fermi level ( $E_F$ ), which no electrons fill. On the contrary, more electrons fill the bonding orbital, making adsorption too strong because of the stabilization effect of the bonding orbital. In the case of FeCoNiMn, the adsorption of LiO<sub>2</sub> and Li<sub>2</sub>O<sub>2</sub> is too strong on its surface. Thus, LiO<sub>2</sub> cannot transform into Li<sub>2</sub>O<sub>2</sub> sufficiently, and it is difficult for Li<sub>2</sub>O<sub>2</sub> to decompose into O<sub>2</sub>. When the d-band center is too low, the energy of the antibonding orbital is lower than  $E_F$ , and then the electrons fill both the antibonding and bonding orbitals; thus, the proportion of electrons in the antibonding orbital increases, which offsets the stabilization effect of the bonding orbital to some extent, making adsorption too weak. In the case of FeCoNiMnPt, the adsorption of LiO<sub>2</sub> is too weak on its surface. Thus, the conversion of LiO<sub>2</sub> to Li<sub>2</sub>O<sub>2</sub> is sluggish, and the slow electronic transfer caused by the weak



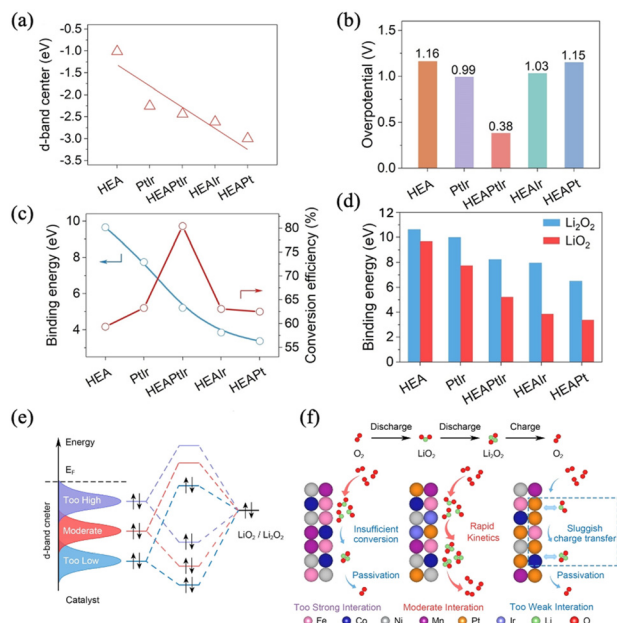


**Fig. 18** (a) d-Band centers of HEA, PtIr, HEAPtIr, HEAlr, and HEAPt. (b) Corresponding overpotentials at 500 mA g<sup>-1</sup> of the five alloy materials at 200 mA g<sup>-1</sup> with a limited capacity of 1000 mAh g<sup>-1</sup>. (c) Binding energies between LiO<sub>2</sub> and as-designed cathodes (HEA, PtIr, HEAPtIr, HEAlr, and HEAPt), and the energy conversion efficiency of LOBs with different cathodes. (d) Binding energies of LiO<sub>2</sub> and Li<sub>2</sub>O<sub>2</sub> on as-designed cathodes. (e) Orbital interactions between LiO<sub>2</sub>/Li<sub>2</sub>O<sub>2</sub> and catalysts with different d-band centers and (f) corresponding catalytic effects. Reproduced with permission.<sup>218</sup> Copyright 2023, Wiley-VCH GmbH.

interaction between the catalyst and O makes it difficult for Li<sub>2</sub>O<sub>2</sub> on its surface to decompose, leading to surface passivation. Therefore, when the energy of the d-band center is moderate, the energies of the antibonding and bonding orbitals and electrons filling them are suitable, making adsorption ideal.

Tao *et al.* developed a universal low-temperature method for synthesizing subnanometer ribbons (SNRs), with a single layer possesses a thickness of 0.8 nm and containing up to 8 elements, using Ag nanowires as a template.<sup>219</sup> PtPdIrRuAuAg SNRs/C (PtPdIrRuAuAg deposited on commercial carbon black) was used as an Li–O<sub>2</sub> catalyst. At 100 mA g<sup>-1</sup> with a limited capacity of 1000 mAh g<sup>-1</sup>, the Li–O<sub>2</sub> cell with this catalyst showed a low OER overpotential of only 0.49 V. Even when the current increased to 1 A g<sup>-1</sup>, an OER overpotential of 0.75 V was observed. Also, the Li–O<sub>2</sub> battery with this catalyst could run for 100 stable cycles at 500 mA g<sup>-1</sup> with a limited capacity of 1000 mAh g<sup>-1</sup>, and its terminal charge voltage was lower than about 3.8 V.

In addition, HEA nanoparticles (NPs) have been well-designed recently. Wang *et al.* first developed a continuous “droplet-to-particle” method to fabricate hollow HEA NPs.<sup>220</sup> The hollow structure can save 60% materials but provide the same number of active sites on its surface. Zhang *et al.* synthesized a core-satellite HEA@Pt heterogeneous catalyst with PtRuFeCoNi HEA NPs as the core and Pt dendrites on

its surface.<sup>221</sup> As mentioned before, changes in the electronic structure of heterointerfaces can improve the charge transfer and expose the active sites. In detail, exposed electron-rich and electron-deficient sites prompt ORR and OER kinetics, respectively. Due to the lower electronegativity of the other elements than Pt, the d-band center moved down, and then the adsorption of the adsorbates HEA@Pt was weakened compared to Pt. Owing to the moderate adsorption energy for LiO<sub>2</sub> being between that of HEA and Pt, the HEA@Pt-based LOB showed the maximum capacity of 8400 mAh g<sup>-1</sup> at 100 mA g<sup>-1</sup> with a low overpotential of only 0.46 V, a small overpotential of only 0.37 V at 100 mA g<sup>-1</sup> with a fixed capacity of 1000 mAh g<sup>-1</sup>, and 210 cycles, among which the terminal voltages of approximately the first 180 cycles were very stable. Wu *et al.* synthesized PtFeCoNiCu NPs loaded on reduced graphene oxide (PtFeCoNiCu@rGO) through a high-temperature annealing route.<sup>222</sup> Due to the rich pores and large specific surface area of rGO as well as high electronic conductivity and lattice distortion effect of the HEA NPs, the PtFeCoNiCu@rGO-based LOB showed a high maximum capacity of 13 949 mA g<sup>-1</sup> at 100 mA g<sup>-1</sup>, a low overpotential of 0.77 V and 148 cycles at 100 mA g<sup>-1</sup> with a limited capacity of 500 mAh g<sup>-1</sup>. By removing the nonnoble elements on the surface of PtFeCoNiCuMo HEA, causing some free Pt single atoms to be caught by defect-rich CNTs, Li *et al.* fabricated amorphous Pt-skin-coated HEA nanoparticles paired with Pt single atoms (HEA@Pt-Pt<sub>SAS</sub>) on CNTs.<sup>223</sup> Toroid-like Li<sub>2</sub>O<sub>2</sub> tended to form on the pure Pt cathode and film-like Li<sub>2</sub>O<sub>2</sub> tended to form on HEA. Due to the synergistic catalysis of Pt and HEA, needle-like Li<sub>2</sub>O<sub>2</sub> was observed on HEA@Pt-Pt<sub>SAS</sub>. Owing to its suitable adsorption energy, the HEA@Pt-Pt<sub>SAS</sub>-based LOB showed an excellent performance including an ultralow total overpotential of 0.3 V at 200 mA g<sup>-1</sup> with a fixed capacity of 1000 mAh g<sup>-1</sup>, 470 cycles at 1000 mA g<sup>-1</sup> with a fixed capacity of 1000 mAh g<sup>-1</sup>, and a maximum capacity of 13 116 mAh g<sup>-1</sup> at 200 mA g<sup>-1</sup>. Furthermore, no clear parasitic reactions were detected, revealing that HEA@Pt-Pt<sub>SAS</sub> had an obvious inhibitory effect on them.

Compared to traditional alloys, HEAs can contain fewer noble metals by increasing the content of nonnoble metals, making HEAs more economical. In future studies, the development of more HEAs that show higher stability and catalytic activity than traditional alloys will be a great contribution to the commercialization of Li–O<sub>2</sub> batteries.

**Noble metal oxides.** Noble metal oxides such as RuO<sub>2</sub> and IrO<sub>2</sub> have been deeply explored and used in acidic or alkaline electrolytes in electrolyzers, photoelectrochemical water splitting, and metal-air batteries because of their outstanding OER performances.<sup>118,119</sup> They have also shown potential as Li–O<sub>2</sub> cathode catalysts.<sup>34,108,120–122</sup> For example, hierarchically porous metallic RuO<sub>2</sub> hollow spheres were applied as a carbon-free Li–O<sub>2</sub> cathode.<sup>123</sup> These RuO<sub>2</sub> hollow spheres showed a low charge potential of *ca.* 3.5 V, with the OER/ORR overpotentials of 0.54/0.13 V, a reversible capacity of *ca.* 1400 mAh g<sup>-1</sup>, and 100 cycles of full discharge and charge. Furthermore, to improve the stability of the RuO<sub>2</sub> nanoparticles and avoid their



agglomeration, they were covered with N-doped graphene.<sup>124</sup> The batteries based on the encapsulated RuO<sub>2</sub> cathode operated for over 110 cycles and exhibited a stable lower charge potential (<4.05 V) compared to the batteries based on unencapsulated RuO<sub>2</sub>, showing poorer stability of *ca.* 60 cycles. IrO<sub>2</sub> supported on KB as Li–O<sub>2</sub> cathodes showed a 0.4 V lower charge overpotential than pure KB due to the high OER catalytic activity of IrO<sub>2</sub>.<sup>125</sup> Unfortunately, IrO<sub>2</sub> has been relatively less researched due to its high prices.

Noble metals and their oxides have exhibited potential for accelerating ORR and OER in Li–O<sub>2</sub> cells, respectively. Thus, the combination of noble metals and their oxides may be a possible way to find bifunctional catalysts. The mechanistic understanding of noble-metal-based catalysts has been systematically established through the d-band center theory combined with density functional theory (DFT) calculations.<sup>35,37,38,112,114,115,126</sup> Nevertheless, the high cost of noble metals and their oxides has severely hindered their practical usage on a large scale. Alternatively, although noble-metal single-atom catalysts (SACs) have relatively lower cost, the agglomeration of their atoms can diminish their catalytic activity.<sup>158</sup> Consequently, the design of composite catalysts with noble-metal-free catalysts, such as transition metals and carbon materials, as the main bodies decorated by a small amount of noble metals and/or their oxides, such as doping and core-shell structures, is one possible method to achieve suitable catalysts.

### MOF-based materials

MOFs are coordination polymers that are formed by linking metal atoms and organic ligands, with a periodic network structure. Yaghi *et al.* synthesized a crystalline, metal-organic, open framework having extended channel systems and composed of uncommon metal coordination, and they first used the term “metal-organic framework” (MOF) to describe these polymers.<sup>127</sup> Owing to their potential advantages including specific crystalline structures, low density, and high specific surface areas, MOFs have been applied in numerous fields, particularly catalysis.<sup>42,128,129</sup>

MOFs were first applied as Li–O<sub>2</sub> cathode materials in 2014, and it was found that their rich and even pores could gather at most 18 times the O<sub>2</sub> density than that in the atmosphere at 273 K.<sup>130</sup> A high capacity of 9420 mAh g<sup>-1</sup> was gained in Mn-MOF-74-based Li–O<sub>2</sub> cells, which was more than 4-times larger than that of super-P-based Li–O<sub>2</sub> cells.

After that, more MOF-derived materials, such as atom-doped MOFs and their composites (such as composites with MXenes), have been tested as Li–O<sub>2</sub> cathodes because of the intrinsic poor electron conductivity and low stability of MOFs.<sup>27,42,129,131–134</sup> To address these problems, an Fe(III)-MOF-5 carbonization-derived conductive carbon structure was fabricated through thermal annealing.<sup>133</sup> Covered by a thin carbon layer, the hierarchical mesoporous ZnO/ZnFe<sub>2</sub>O<sub>4</sub>/C (ZZFC) nanocages obtained at the sintering temperature at 500 °C had a balance of good electronic conductivity and

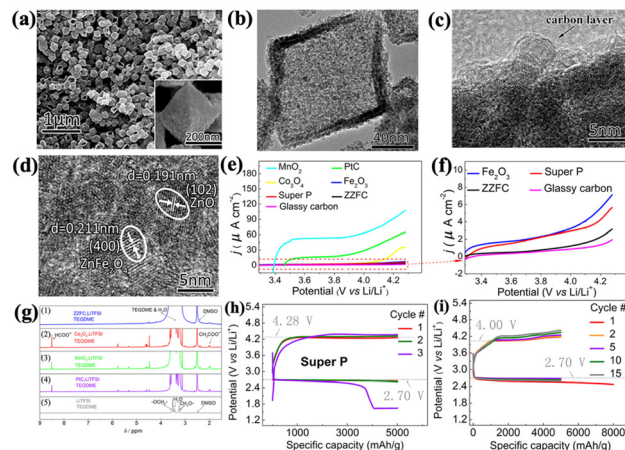


**Fig. 19** (a) SEM images of ZZFC. (b) TEM images of ZZFC. (c and d) High-resolution TEM images of ZZFC. (e and f) LSV curves measured on a rotating glassy carbon electrode coated with various air-electrode materials (the sweep rate was set at 0.01 V s<sup>-1</sup> without rotation; panel f is the magnified image of panel e). (g) Magnified <sup>1</sup>H NMR spectra of the electrolytes with various cathodes after cycling (the cathode catalyst in each sample is (1) ZZFC, (2) Co<sub>3</sub>O<sub>4</sub>, (3) MnO<sub>2</sub>, and (4) 5% PtC; all spectra are presented after magnified). (5) Non-magnified <sup>1</sup>H NMR spectra of 1.0 mol L<sup>-1</sup> LiTFSI in TEGDME solution. (h) Fixed capacity galvanostatic discharge/charge curves of super P cathode (90% super P + 10% PVDF). (i) Galvanostatic discharge/charge curves of ZZFC cathode in a “deep discharge + fixed capacity” mode. The cell was first discharged to 8000 mAh g<sup>-1</sup>, and then cycled at a fixed capacity of 5000 mAh g<sup>-1</sup>. (a–i) Reproduced with permission.<sup>133</sup> Copyright 2015, the American Chemical Society.

proper porosity with the average pore size of 12.2 nm (– Fig. 19a–d). Therefore, the stability was enhanced, as proven by a series of LSV and NMR experiments, where the TEGDME-based electrolyte hardly decomposed in the presence of the ZZFC electrode (Fig. 19e–g). Furthermore, the ZZFC-based Li–O<sub>2</sub> batteries could run for 15 cycles at the fixed capacity of 5000 mAh g<sup>-1</sup>, 12 more cycles than the super-P-based Li–O<sub>2</sub> batteries (Fig. 19h and i).

Flower-like Co and Ni atom-doped MOFs (CoNi-MOFs) exhibited higher electrochemical catalytic performance than Ni-MOF due to the change in the adsorption of the LiO<sub>2</sub> intermediate and the enlarged pore size of CoNi-MOFs (Fig. 20e and f).<sup>134</sup> The pores with larger sizes permitted the smoother transportation of Li<sup>+</sup> and O<sub>2</sub> as well as the greater deposition of Li<sub>2</sub>O<sub>2</sub>, which accelerated the electron transfer and promoted the capacity. In comparison to Ni-MOFs, where only film-like Li<sub>2</sub>O<sub>2</sub> was formed, film-like Li<sub>2</sub>O<sub>2</sub> through the surface path and toroid-like Li<sub>2</sub>O<sub>2</sub> through the solution path were formed on the surface of CoNi-MOFs after discharge to 600 mAh g<sup>-1</sup> (Fig. 20a and b). As the discharge capacity increased to 2000 mAh g<sup>-1</sup>, toroid-like Li<sub>2</sub>O<sub>2</sub> remained, which could better ease the congestion of the Li<sup>+</sup> and O<sub>2</sub> diffusion channels than the film-like Li<sub>2</sub>O<sub>2</sub> (Fig. 20c). Also, after charging, Li<sub>2</sub>O<sub>2</sub> completely disappeared (Fig. 20d), which indicated the excellent cyclic ability of CoNi-MOFs.

Interestingly, a 3D printed MOF-derived hierarchically porous framework was used as an Li–O<sub>2</sub> cathode material.<sup>135</sup>



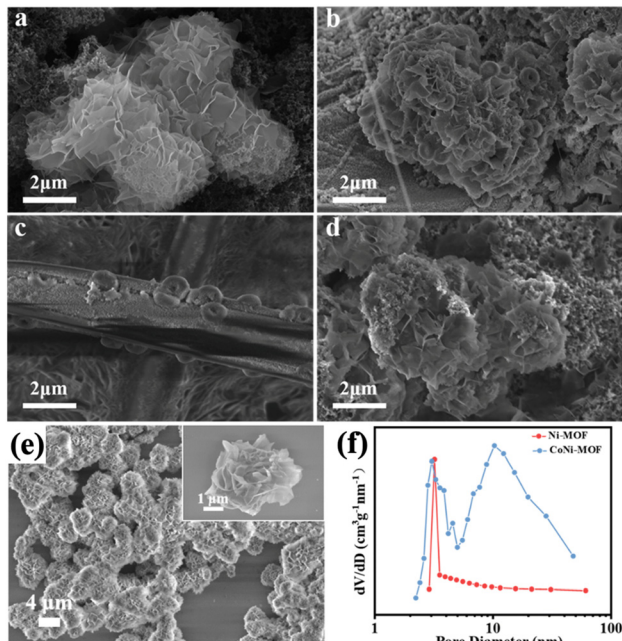


**Fig. 20** SEM images of the CoNi-MOF cathodes: (a) fresh cathode, (b) discharge to  $600 \text{ mAh g}^{-1}$ , (c) discharged to  $2000 \text{ mAh g}^{-1}$  and (d) recharged to  $2000 \text{ mAh g}^{-1}$ . (e) SEM images of CoNi-MOF (the inset is an enlarged SEM image). (f) Pore size distribution curve of Ni-MOF and CoNi-MOF. (a–f) Reproduced with permission.<sup>134</sup> Copyright 2024, the American Chemical Society.

Applying one-step calcination, Co nanoparticles assembled in N-doped mesoporous carbon flakes (3DP-NC-Co) were decomposed from the Co-MOF gained from 3D printing (3DP-Co-MOF), as shown in Fig. 21a. The 3DP-Co-MOF had

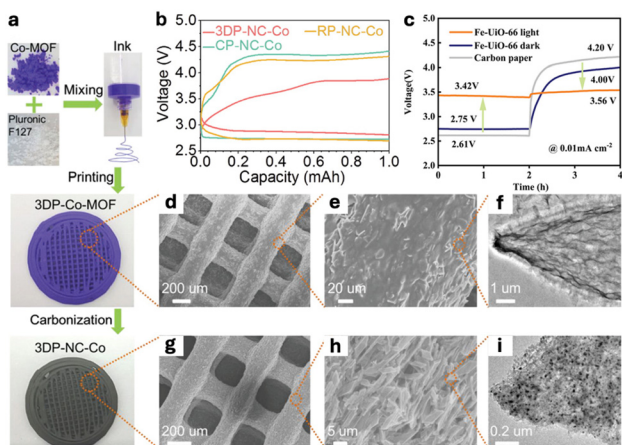


**Fig. 21** (a) Diagram showing the preparation of a 3DP Co-MOF-derived framework. (b) Comparison of the charge overpotential with the marked cathodes at a limited capacity of 1 mAh and current density of  $0.1 \text{ mA cm}^{-2}$ . (c) Discharge and charge profiles of the Li-O<sub>2</sub> battery with and without illumination. (d–f) Typical characterization of 3DP-Co-MOF. (d and e) SEM images. (f) TEM image. (g–i) Typical characterization of 3DP-NC-Co. (g and h) SEM images. (i) TEM image. (a and b) and (d–i) reproduced with permission.<sup>135</sup> © 2018, WILEY-VCH Verlag GmbH & Co. KGaA, Weinheim. (c) Reproduced with permission.<sup>136</sup> © 2024, Wiley-VCH GmbH.

large pores (*ca.* 200 nm), and its crystal blocks had micron-sized leaf structures (Fig. 21d–f). 3DP-NC-Co retained the framework of 3DP-Co-MOF (Fig. 21g–i). Compared to the Co-MOF-derived powder (NC-Co), 3DP-NC-Co showed a higher specific surface area ( $640 \text{ m}^2 \text{ g}^{-1}$  vs.  $433 \text{ m}^2 \text{ g}^{-1}$ ) and a larger meso- and microporous volume ( $1.09 \text{ cm}^3 \text{ g}^{-1}$  vs.  $0.21 \text{ cm}^3 \text{ g}^{-1}$ ), respectively, which illustrated the importance of the hierarchical porous network geometry. More Li<sub>2</sub>O<sub>2</sub> nanoparticles could deposit in the micron-sized pores to improve the capacity and achieve good contact with the cathode to enable the easier decomposition of Li<sub>2</sub>O<sub>2</sub> during charging, which led to lower overpotentials for 3DP-NC-Co than NC-Co randomly packed on carbon paper (RP-NC-Co) and NC-Co directly grown on carbon paper (CP-NC-Co), as shown in Fig. 21b.

Photoactive MOFs have been successfully employed in photo-assisted Li-O<sub>2</sub> batteries.<sup>137</sup> Because of the impacts of photoelectrons and holes produced by photocatalysts, the discharge voltage can surpass the thermodynamic limit value (2.96 V),<sup>138</sup> for example, 3.42 V in Fig. 21c. Recently, Fe<sup>3+</sup> ions were doped in UiO-66 (Fe-UiO-66) as a bifunctional Li-O<sub>2</sub> cathode catalyst.<sup>136</sup> Fe<sup>3+</sup> may act as an electron donor and oxidation site, and the charge was transferred from Fe<sup>3+</sup> to Zr-oxo clusters, expanding the visible light absorption. Then, the photogenerated electrons accelerated the reduction of O<sub>2</sub> to O<sub>2</sub><sup>•−</sup> radicals, expediting the ORR process. A thin Li<sub>2</sub>O<sub>2</sub> film was formed after discharge in the presence of light, which is much more conducive to the charge process than bulk Li<sub>2</sub>O<sub>2</sub> without light because of the larger contact area between Fe-UiO-66 and the Li<sub>2</sub>O<sub>2</sub> film. In addition, there was an electronic energy input during exposure to light. Therefore, when employed in Li-O<sub>2</sub> cells, Fe-UiO-66 in the presence of light exhibited a much lower overall overpotential of 0.14 V than Fe-UiO-66 in the dark (Fig. 21c) and 500 stable cycles.

As one of the emerging materials used as Li-O<sub>2</sub> cathodes, MOF-based materials exhibit significant promise due to their well-defined porous structures, high specific surface areas and other inherent advantages. Furthermore, to improve their electronic conductivity and stability, the design of hierarchical structures, the optimization of their porosity, the coating of a carbon layer, metal atom doping, and formation of composites with high conductive carbon materials are widely applied. Research has explored the relationship between the quantitative electronic structure and the OER activity of bimetallic Ni-based MOFs in KOH electrolyte.<sup>139</sup> However, analogous studies on MOF-based materials in the organic electrolytes or ionic liquids (ILs) commonly used in Li-O<sub>2</sub> batteries remain limited. In addition, reducing the synthesis costs of MOF-based materials is also a critical challenge for their practical application.<sup>131</sup>

## Conclusion and outlook

This review provides an overview of Li-O<sub>2</sub> cathode catalysts/materials, including transition metals and their compounds, carbon-based materials, noble metals, their alloys and oxides,



and MOF-based materials from different perspectives, respectively. The cathode catalysts mentioned in this review are summarized in Table 1.

Doping engineering, vacancy/defect engineering, crystal plane effects, spin engineering and amorphization strategy have been proven to be some of the most common modulation methods for TMCs, as illustrated by the examples of  $\text{Co}_3\text{O}_4$ ,  $\text{ZnCo}_2\text{O}_4$  and  $\text{NiCo}_2\text{O}_4$ . Due to their wide range of advantages, including high specific surface area, quantum size effect, and easy heterostructure engineering with supports, nano-sized TMCs have also been widely applied in Li– $\text{O}_2$  batteries. MXenes, as common supports for TMCs, were introduced in detail because of their excellent electronic conductivity and high surface areas.

Carbon-based materials play an important role in LOBs due to their rich resources, suitable prices, high electronic conductivity, *etc.* Much attention was paid to the importance of pores, especially mesopores, in terms of  $\text{O}_2$  diffusion and improving the Li– $\text{O}_2$  capacity herein. Then, 1D CNTs/CNFs were reported through modulation strategies, among which N-doping was analyzed preferentially due to the great changes in nanotubes caused by N atoms, followed by a discussion on 2D CNSs/GNSs.

In general, noble metals exhibit superior ORR activity, while their oxides demonstrate higher activity in OER. The d-band model and DFT calculations serve as powerful tools for assessing the catalytic activities of noble metal-based materials for ORR and OER. Alloying has been demonstrated to be an effective strategy to improve the OER activity of noble metals. Recently, high-entropy alloys have gained much attention due to their peculiar effects not shown by traditional alloys. However, the high costs of noble metals hinder their practical use.

Recently, MOF-based materials with rich pores and high specific surface areas have begun to demonstrate potential as Li– $\text{O}_2$  cathodes. Notably, photoactive MOFs exhibit the capability to dramatically reduce the overall overpotential, while maintaining long cycle lives.

However, there are common obstacles for all types of cathode catalysts, hindering the commercialization of LOBs, including Li dendrites, parasitic reactions, and unclear catalytic mechanisms.

Therefore, great efforts need to be devoted to solving these technological difficulties. The specific strategies are as follows:

1. Owing to the unclear catalytic mechanism, the unclear role of the electrolyte, and the controversial oxygen reduction reaction mechanism, the development of cathode catalysts is unsatisfactory. Also, the current analysis of the advantages of new catalysts mainly depends on theoretical calculations, such as DFT calculations.

*In situ* probing techniques, such as *in situ* electrochemical quartz microbalance (EQCM) and fluorescence microscopy, are helpful for detecting the changes in the composition and structure of the electrodes and electrolyte.<sup>140–142</sup> For example, *in situ* TEM was used for detecting the decomposition of

$\text{Li}_2\text{O}_2$ .<sup>140</sup> *In situ* electron paramagnetic resonance (EPR) can be used to monitor the formation of Li dendrites.<sup>143</sup>

However, most of the *in situ* techniques cannot combine the analysis of the evolution in electrochemical performance and chemical compositional and structural changes. Recently, *in situ* electrochemical impedance spectroscopy (EIS) combined with the distribution of relaxation times (DRT) and the distribution of capacitive times (DCT) was found to be a viable solution to this problem.<sup>144</sup> Thus, the exploration of more effective *in situ* probing techniques is a direction to reveal the unclear mechanisms.

2. The research on universal descriptors for catalysts of the same category and the foundation of models are important because of their great roles in evaluating and forecasting new materials. For example, the  $e_g$  occupancy, d-band center/model, and metal–O covalency have been widely used as descriptors for transition metal oxides.<sup>145–147</sup> Recently, a new descriptor,  $W_F$ , for 2D transition metal oxides has been reported to evaluate the  $\text{LiO}_2$  adsorption energy and overall catalytic properties.<sup>148</sup> The descriptors and models can provide a better understanding of emerging cathode catalyst development.

3. Attention also needs to be paid to the control of the decomposition of the electrolyte and cathode materials in the presence of  $\text{Li}_2\text{O}_2$ , which means they should remain stable in the presence of each other. Generally, carbon-based materials can catalyze the degradation of the electrolyte, such as organic carbonate-based electrolytes and ethers.<sup>16,149</sup> Thus, it is necessary to find stable and high-donor-number electrolytes that are not only resistant to side reactions but also able to achieve higher capacities.

4. The addition of soluble catalysts, including RMs in pairs, ligand mediators<sup>224–226</sup> (LMs) that can change the solvation structure of ions or coordinate with them, multifunctional additives,<sup>227–230</sup> soluble photocatalysts used for photos-assisted Li– $\text{O}_2$  batteries,<sup>231</sup> and anti-superoxide disproportionators,<sup>232,233</sup> to the electrolyte has been attracting more attention recently. It has been reported that RMs can enhance the cycling ability and make carbon materials more stable.<sup>150,151</sup> Ligand mediators form complexes with ions or molecules such as  $\text{O}_2$ ,<sup>224,226</sup>  $\text{Li}^+$ ,<sup>225</sup> and  $\text{O}_2^-$ ,<sup>228,229</sup> which prompt ORR and even make changes in the final discharge product from  $\text{Li}_2\text{O}_2$  to LiOH possible.<sup>224</sup> A low LiOH decomposition voltage effectively lowers the OER overpotential. In this case, multifunctional catalysts such as carbonized polymer dots (CPD)<sup>230</sup> play two or three roles, including serving as RMs and/or LMs,<sup>227–229</sup> protecting the Li anode,<sup>229,230</sup> increasing the stability of the electrolyte,<sup>230</sup> and accelerating the superoxide disproportionation reaction.<sup>227</sup> Notably, to relieve the slow dynamics of  $\text{Li}_2\text{O}_2$  decomposition, iridium (Ir) single-atom-based porous organic polymers (Ir/AP-POP), as anti-superoxide disproportionation, have been developed to make nonsolid  $\text{LiO}_2$  the final discharge product.<sup>232</sup> An Ir/AP-POP-based Li– $\text{O}_2$  battery with a carbon cloth cathode showed an ultralow OER overpotential of 0.03 V, an ultrahigh maximum capacity of 12.8 mAh and a long



cyclic life of over 700 h. In short, the development of more stable soluble catalysts is favorable for the experimental exploration of Li–O<sub>2</sub> batteries.

5. The Li anode should be protected from erosion due to H<sub>2</sub>O and CO<sub>2</sub> and the growth of Li dendrites. Thus far, protective layers such as a film induced *via* an *in situ* electrochemical process,<sup>152</sup> an organic–inorganic hybrid layer (OIHL),<sup>153</sup> and a layer comprised of a conductive polymer and AlF<sub>3</sub> particles<sup>154</sup> have been used to protect the Li anode. The research on protective layers is meaningful for the suppression of the growth of Li dendrites, Li anode erosion, and electrolyte decomposition.

6. Machine learning can be a powerful tool for improving the performance of Li–O<sub>2</sub> batteries. Thus far, in the field of Li–O<sub>2</sub> batteries, machine learning has been used in developing a dual-solvent electrolyte possessing anion-induced ion-solvent-coordinated structures, which contribute to the formation of a stable inorganic-rich solid electrolyte interphase (SEI), and consequently a better performance in LOBs,<sup>155</sup> finding factors that lead to a better performance based on thousands of experimental data,<sup>156</sup> and predicting the chemical stability of organic materials including many electrolyte solvents and RMs.<sup>157</sup>

In the future, AI models that can anticipate new high-performance materials may be developed and make a great difference in this field based on big data on Li–O<sub>2</sub> batteries including their working mechanism, basic systematic knowledge about common materials and experimental outcomes.

Through the implementation of these strategies and considering the urgent demand for high-energy-density batteries, lithium–oxygen batteries are anticipated to be promising candidates.

## Data availability

No primary research results, software or code have been included, and no new data were generated or analyzed as part of this review.

## Author contributions

Chen Liu: conceptualization, methodology, investigation, visualization, writing – original draft, writing – review and editing. Huahuan Wang: methodology, writing – review and editing, and supervision.

## Conflicts of interest

There are no conflicts to declare.

## Acknowledgements

We are especially thankful to associate professors Mr. Sun and Ms. Li in College of New Energy and Materials and State Key Laboratory of Heavy Oil Processing for their valuable and professional suggestions to improve the work.

## Notes and references

- M. M. Thackeray, C. Wolverton and E. D. Isaacs, *Energy Environ. Sci.*, 2012, **5**, 7854–7863.
- P. G. Bruce, S. A. Freunberger, L. J. Hardwick and J.-M. Tarascon, *Nat. Mater.*, 2012, **11**, 19–29.
- Y. Li and J. Lu, *ACS Energy Lett.*, 2017, **2**, 1370–1377.
- K. M. Abraham and Z. Jiang, *J. Electrochem. Soc.*, 1996, **143**, 1.
- A. C. Luntz and B. D. McCloskey, *Chem. Rev.*, 2014, **114**, 11721–11750.
- H. Li, J. Chen and J. Fang, *Adv. Mater. Technol.*, 2023, **8**, 2201762.
- Y. Han, X. Zhang, B. Lu, Y. Li, C. Shao, Q. Guo and Z. Zhang, *Nano Futures*, 2020, **4**, 032005.
- C. Chen, J. Liu, Z. Liu, J. Xue, X. Cui, W. Liu, P. Cheng, T. Huang and A. Yu, *Chem. Rec.*, 2025, e202400046.
- J. Guo, X. Meng, Q. Wang, Y. Zhang, S. Yan and S. Luo, *Batteries*, 2024, **10**, 260.
- N. Mahne, B. Schafzahl, C. Leypold, M. Leypold, S. Grumm, A. Leitgeb, G. A. Strohmeier, M. Wilkening, O. Fontaine, D. Kramer, C. Slugovc, S. M. Borisov and S. A. Freunberger, *Nat. Energy*, 2017, **2**, 17036.
- J. Wandt, P. Jakes, J. Granwehr, H. A. Gasteiger and R.-A. Eichel, *Angew. Chem.*, 2016, **128**, 7006–7009.
- W. Xu, J. Wang, F. Ding, X. Chen, E. Nasybulin, Y. Zhang and J.-G. Zhang, *Energy Environ. Sci.*, 2014, **7**, 513–537.
- X.-B. Cheng, R. Zhang, C.-Z. Zhao and Q. Zhang, *Chem. Rev.*, 2017, **117**, 10403–10473.
- S. A. Freunberger, Y. Chen, Z. Peng, J. M. Griffin, L. J. Hardwick, F. Barde, P. Novak and P. G. Bruce, *J. Am. Chem. Soc.*, 2011, **133**, 8040–8047.
- B. D. McCloskey, D. S. Bethune, R. M. Shelby, G. Girishkumar and A. C. Luntz, *J. Phys. Chem. Lett.*, 2011, **2**, 1161–1166.
- M. M. O. Thotiyil, S. A. Freunberger, Z. Peng and P. G. Bruce, *J. Am. Chem. Soc.*, 2013, **135**, 494–500.
- D. Geng, N. Ding, T. S. A. Hor, S. W. Chien, Z. Liu, D. Wu, X. Sun and Y. Zong, *Adv. Energy Mater.*, 2016, **6**, 1502164.
- G. Zhao, Z. Xu and K. Sun, *J. Mater. Chem. A*, 2013, **1**, 12862–12867.
- S. R. Younesi, S. Urbonaite, F. Björefors and K. Edström, *J. Power Sources*, 2011, **196**, 9835–9838.
- C. Dang, Q. Mu, X. Xie, X. Sun, X. Yang, Y. Zhang, S. Maganti, M. Huang, Q. Jiang, I. Seok, W. Du and C. Hou, *Adv. Compos. Hybrid Mater.*, 2022, **5**, 606–626.
- C. O. Laoire, S. Mukerjee, K. M. Abraham, E. J. Plichta and M. A. Hendrickson, *J. Phys. Chem. C*, 2009, **113**, 20127–20134.
- B. D. McCloskey, R. Scheffler, A. Speidel, G. Girishkumar and A. C. Luntz, *J. Phys. Chem. C*, 2012, **116**, 23897–23905.
- B. D. Adams, C. Radtke, R. Black, M. L. Trudeau, K. Zaghbi and L. F. Nazar, *Energy Environ. Sci.*, 2013, **6**, 1772–1778.
- N. B. Aetukuri, B. D. McCloskey, J. M. García, L. E. Krupp, V. Viswanathan and A. C. Luntz, *Nat. Chem.*, 2015, **7**, 50–56.
- L. Ma, T. Yu, E. Tzoganakis, K. Amine, T. Wu, Z. Chen and J. Lu, *Adv. Energy Mater.*, 2018, **8**, 1800348.



- 26 Z. Liu, Z. Zhao, W. Zhang, Y. Huang, Y. Liu, D. Wu, L. Wang and S. Chou, *InfoMat*, 2022, **4**, e12260.
- 27 J. Zhang, L. Wang, L. Xu, X. Ge, X. Zhao, M. Lai, Z. Liu and W. Chen, *Nanoscale*, 2015, **7**, 720–726.
- 28 T.-F. Hung, S. G. Mohamed, C.-C. Shen, Y.-Q. Tsai, W.-S. Chang and R.-S. Liu, *Nanoscale*, 2013, **5**, 12115–12119.
- 29 B. He, J. Wang, J. Liu, Y. Li, Q. Huang, Y. Hou, G. Li, J. Li, R. Zhang, J. Zhou, W. Tian, Y. Du, F. Dang, H. Wang and B. Kong, *Adv. Energy Mater.*, 2020, **10**, 1904262.
- 30 S. Jing, Z. Gai, M. Li, S. Tang, S. Ji, H. Liang, F. Chen, S. Yin and P. Tsiakaras, *Electrochim. Acta*, 2022, **410**, 140002.
- 31 S. Matsuda, E. Yasukawa, T. Kameda, S. Kimura, S. Yamaguchi, Y. Kubo and K. Uosaki, *Cell Rep. Phys. Sci.*, 2021, **2**, 100506.
- 32 S. L. Candelaria, Y. Shao, W. Zhou, X. Li, J. Xiao, J.-G. Zhang, Y. Wang, J. Liu, J. Li and G. Cao, *Nano Energy*, 2012, **1**, 195–220.
- 33 Z. Peng, S. A. Freunberger, Y. Chen and P. G. Bruce, *Science*, 2012, **337**, 563–566.
- 34 Y.-B. Yin, J.-J. Xu, Q.-C. Liu and X.-B. Zhang, *Adv. Mater.*, 2016, **28**, 7494–7500.
- 35 Y. Zhou, Q. Gu, K. Yin, Y. Li, L. Tao, H. Tan, Y. Yang and S. Guo, *Angew. Chem., Int. Ed.*, 2022, **61**, e202201416.
- 36 K. Song, J. Jung, M. Park, H. Park, H.-J. Kim, S.-I. Choi, J. Yang, K. Kang, Y.-K. Han and Y.-M. Kang, *ACS Catal.*, 2018, **8**, 9006–9015.
- 37 B. G. Kim, H.-J. Kim, S. Back, K. W. Nam, Y. Jung, Y.-K. Han and J. W. Choi, *Sci. Rep.*, 2014, **4**, 4225.
- 38 Y. Zhou, K. Yin, Q. Gu, L. Tao, Y. Li, H. Tan, J. Zhou, W. Zhang, H. Li and S. Guo, *Angew. Chem., Int. Ed.*, 2021, **60**, 26592–26598.
- 39 Y.-C. Lu, Z. Xu, H. A. Gasteiger, S. Chen, K. Hamad-Schifferli and Y. Shao-Horn, *J. Am. Chem. Soc.*, 2010, **132**, 12170–12171.
- 40 J. Lu, Y. Lei, K. C. Lau, X. Luo, P. Du, J. Wen, R. S. Assary, U. Das, D. J. Miller, J. W. Elam, H. M. Albishri, D. A. El-Hady, Y.-K. Sun, L. A. Curtiss and K. Amine, *Nat. Commun.*, 2013, **4**, 2383.
- 41 D. Su, S. Dou and G. Wang, *NPG Asia Mater.*, 2015, **7**, e155–e155.
- 42 H. Ma, S. Luo, J. Cong and S. Yan, *Inorganics*, 2025, **13**(2), 56.
- 43 H. Furukawa, K. E. Cordova, M. O’Keeffe and O. M. Yaghi, *Science*, 2013, **341**, 1230444.
- 44 R. Zhao, Z. Liang, R. Zou and Q. Xu, *Joule*, 2018, **2**, 2235–2259.
- 45 H. Yuan, L. Kong, T. Li and Q. Zhang, *Chin. Chem. Lett.*, 2017, **28**, 2180–2194.
- 46 M. M. O. Thotiyil, S. A. Freunberger, Z. Peng, Y. Chen, Z. Liu and P. G. Bruce, *Nat. Mater.*, 2013, **12**, 1049–1055.
- 47 A. Kondori, Z. Jiang, M. Esmaeilrad, M. Tamadoni Saray, A. Kakekhani, K. Kucuk, P. Navarro Munoz Delgado, S. Maghsoudipour, J. Hayes, C. S. Johnson, C. U. Segre, R. Shahbazian-Yassar, A. M. Rappe and M. Asadi, *Adv. Mater.*, 2020, **32**, 2004028.
- 48 W. H. Bragg, *Nature*, 1915, **95**, 561–561.
- 49 Q. Zhao, Z. Yan, C. Chen and J. Chen, *Chem. Rev.*, 2017, **117**, 10121–10211.
- 50 A. Seko, K. Yuge, F. Oba, A. Kuwabara and I. Tanaka, *Phys. Rev. B: Condens. Matter Mater. Phys.*, 2006, **73**, 184117.
- 51 M. G. Brik, A. Suchocki and A. Kamińska, *Inorg. Chem.*, 2014, **53**, 5088–5099.
- 52 F. Cheng and J. Chen, *Chem. Soc. Rev.*, 2012, **41**, 2172–2192.
- 53 Y. Cai, Y. Hou, Y. Lu and J. Chen, *Inorganics*, 2019, **7**, 69.
- 54 Y. Xia, Z. Hong, L. Wang, X. Jin, S. Lin, J. Yan, D.-L. Peng, Z. Yu and G. Yue, *J. Power Sources*, 2025, **635**, 236542.
- 55 Y. Liang, Y. Li, H. Wang, J. Zhou, J. Wang, T. Regier and H. Dai, *Nat. Mater.*, 2011, **10**, 780–786.
- 56 F. Cheng, J. Shen, B. Peng, Y. Pan, Z. Tao and J. Chen, *Nat. Chem.*, 2011, **3**, 79–84.
- 57 G. Wang, S. Zhang, R. Qian and Z. Wen, *ACS Appl. Mater. Interfaces*, 2018, **10**, 41398–41406.
- 58 R. Zheng, C. Shu, Z. Hou, A. Hu, P. Hei, T. Yang, J. Li, R. Liang and J. Long, *ACS Appl. Mater. Interfaces*, 2019, **11**, 46696–46704.
- 59 W. Tang, K. Teng, W. Guo, F. Gu, B. Li, R. Qi, R. Liu, Y. Lin, M. Wu and Y. Chen, *Small*, 2022, **18**, 2202194.
- 60 X. Liu, L. Zhao, H. Xu, Q. Huang, Y. Wang, C. Hou, Y. Hou, J. Wang, F. Dang and J. Zhang, *Adv. Energy Mater.*, 2020, **10**, 2001415.
- 61 S. Liu, H. Du, K. Liu, M.-G. Ma, Y.-E. Kwon, C. Si, X.-X. Ji, S.-E. Choi and X. Zhang, *Adv. Compos. Hybrid Mater.*, 2021, **4**, 1367–1383.
- 62 Z. Zhuang, W. Wang, Y. Wei, T. Li, M. Ma and Y. Ma, *Adv. Compos. Hybrid Mater.*, 2021, **4**, 938–945.
- 63 L. Zhang, T. Song, L. Shi, N. Wen, Z. Wu, C. Sun, D. Jiang and Z. Guo, *J. Nanostruct. Chem.*, 2021, **11**, 323–341.
- 64 Y. Zhai, W. Yang, X. Xie, X. Sun, J. Wang, X. Yang, N. Naik, H. Kimura, W. Du, Z. Guo and C. Hou, *Inorg. Chem. Front.*, 2022, **9**, 1115–1124.
- 65 W.-H. Ryu, T.-H. Yoon, S. H. Song, S. Jeon, Y.-J. Park and I.-D. Kim, *Nano Lett.*, 2013, **13**, 4190–4197.
- 66 S. Liu, Z. Hu, L. Zuo, Q. Yang, G. He, Z. Zhang, X. Lai, Z. Zhu, Q. Zhang, H. Huang, Y. Xiao, L. Wang and Y. Zhao, *Electrochim. Acta*, 2025, **512**, 145479.
- 67 X. Zheng, M. Yuan, P. Su, M. Li, Z. Li, F. Li, H. Li and G. Sun, *Chem. Eng. J.*, 2024, **482**, 148916.
- 68 Z. Lian, Y. Lu, S. Ma, Z. Li and Q. Liu, *Chem. Eng. J.*, 2022, **445**, 136852.
- 69 H. Xu, R. Zheng, D. Du, L. Ren, R. Li, X. Wen, C. Zhao, T. Zeng, B. Zhou and C. Shu, *Sci. China Mater.*, 2022, **65**, 1761–1770.
- 70 L. Leng, J. Li, X. Zeng, H. Song, T. Shu, H. Wang and S. Liao, *J. Power Sources*, 2017, **337**, 173–179.
- 71 Z. Ran, C. Shu, Z. Hou, W. Zhang, Y. Yan, M. He and J. Long, *Chem. Eng. J.*, 2021, **413**, 127404.
- 72 B. Ju, H. J. Song, G.-H. Lee, M.-C. Sung and D.-W. Kim, *Energy Storage Mater.*, 2020, **24**, 594–601.
- 73 X. Chen, Q. Fan, L. Liu, J. Deng and J. Xu, *ACS Appl. Mater. Interfaces*, 2024, **16**, 53697–53704.
- 74 M. Naguib, M. Kurtoglu, V. Presser, J. Lu, J. Niu, M. Heon, L. Hultman, Y. Gogotsi and M. W. Barsoum, *Adv. Mater.*, 2011, **23**, 4248–4253.



- 75 M. Naguib, V. N. Mochalin, M. W. Barsoum and Y. Gogotsi, *Adv. Mater.*, 2014, **26**, 992–1005.
- 76 Y. Wang, Y. Li, Z. Qiu, X. Wu, P. Zhou, T. Zhou, J. Zhao, Z. Miao, J. Zhou and S. Zhuo, *J. Mater. Chem. A*, 2018, **6**, 11189–11197.
- 77 S. B. Ambade, R. B. Ambade, W. Eom, S. H. Noh, S. H. Kim and T. H. Han, *Adv. Mater. Interfaces*, 2018, **5**, 1801361.
- 78 X. Li, C. Wen, H. Li and G. Sun, *J. Energy Chem.*, 2020, **47**, 272–280.
- 79 L. Cong, H. Xie and J. Li, *Adv. Energy Mater.*, 2017, **7**, 1601906.
- 80 B. Yao, J. Zhang, T. Kou, Y. Song, T. Liu and Y. Li, *Adv. Sci.*, 2017, **4**, 1700107.
- 81 Q. Wei, F. Xiong, S. Tan, L. Huang, E. H. Lan, B. Dunn and L. Mai, *Adv. Mater.*, 2017, **29**, 1602300.
- 82 B. Sun, P. Munroe and G. Wang, *Sci. Rep.*, 2013, **3**, 2247.
- 83 H.-D. Lim, K.-Y. Park, H. Song, E. Y. Jang, H. Gwon, J. Kim, Y. H. Kim, M. D. Lima, R. O. Robles, X. Lepró, R. H. Baughman and K. Kang, *Adv. Mater.*, 2013, **25**, 1348–1352.
- 84 G. Q. Zhang, J. P. Zheng, R. Liang, C. Zhang, B. Wang, M. Hendrickson and E. J. Plichta, *J. Electrochem. Soc.*, 2010, **157**, A953.
- 85 Y. Li, J. Wang, X. Li, D. Geng, R. Li and X. Sun, *Chem. Commun.*, 2011, **47**, 9438–9440.
- 86 D. Higgins, Z. Chen, D. U. Lee and Z. Chen, *J. Mater. Chem. A*, 2013, **1**, 2639–2645.
- 87 F. Wu, Y. Xing, X. Zeng, Y. Yuan, X. Zhang, R. Shahbazian-Yassar, J. Wen, D. J. Miller, L. Li, R. Chen, J. Lu and K. Amine, *Adv. Funct. Mater.*, 2016, **26**, 7626–7633.
- 88 X. Yang, P. He and Y. Xia, *Electrochem. Commun.*, 2009, **11**, 1127–1130.
- 89 Y. Li, X. Li, D. Geng, Y. Tang, R. Li, J.-P. Dodelet, M. Lefèvre and X. Sun, *Carbon*, 2013, **64**, 170–177.
- 90 T. Kuboki, T. Okuyama, T. Ohsaki and N. Takami, *J. Power Sources*, 2005, **146**, 766–769.
- 91 N. Ding, S. W. Chien, T. S. A. Hor, R. Lum, Y. Zong and Z. Liu, *J. Mater. Chem. A*, 2014, **2**, 12433–12441.
- 92 B. Sun, S. Chen, H. Liu and G. Wang, *Adv. Funct. Mater.*, 2015, **25**, 4436–4444.
- 93 Z. Guo, D. Zhou, X. Dong, Z. Qiu, Y. Wang and Y. Xia, *Adv. Mater.*, 2013, **25**, 5668–5672.
- 94 K. Sakaushi, T.-P. Fellingner and M. Antonietti, *ChemSusChem*, 2015, **8**, 1156–1160.
- 95 H.-D. Lim, H. Song, H. Gwon, K.-Y. Park, J. Kim, Y. Bae, H. Kim, S.-K. Jung, T. Kim, Y. H. Kim, X. Lepró, R. Ovalle-Robles, R. H. Baughman and K. Kang, *Energy Environ. Sci.*, 2013, **6**, 3570–3575.
- 96 H. Liu, Y. Zhang, R. Li, X. Sun, S. Désilets, H. Abou-Rachid, M. Jaidann and L.-S. Lussier, *Carbon*, 2010, **48**, 1498–1507.
- 97 Y. Chen, J. Wang, H. Liu, M. N. Banis, R. Li, X. Sun, T.-K. Sham, S. Ye and S. Knights, *J. Phys. Chem. C*, 2011, **115**, 3769–3776.
- 98 P. Ayala, A. Grüneis, T. Gemming, D. Grimm, C. Kramberger, M. H. Rummeli, F. L. Jr, H. Freire, R. Kuzmany, A. Pfeiffer, B. Büchner Barreiro and T. Pichler, *J. Phys. Chem. C*, 2007, **111**, 2879–2884.
- 99 Y. Li, J. Wang, X. Li, J. Liu, D. Geng, J. Yang, R. Li and X. Sun, *Electrochem. Commun.*, 2011, **13**, 668–672.
- 100 J. G. Kim, Y. Noh and Y. Kim, *J. Energy Storage*, 2023, **66**, 107329.
- 101 Y. Li, J. Wang, X. Li, D. Geng, M. N. Banis, R. Li and X. Sun, *Electrochem. Commun.*, 2012, **18**, 12–15.
- 102 Y. Li, J. Wang, X. Li, D. Geng, M. N. Banis, Y. Tang, D. Wang, R. Li, T.-K. Sham and X. Sun, *J. Mater. Chem.*, 2012, **22**, 20170–20174.
- 103 P. Wang, Y. Ren, R. Wang, P. Zhang, M. Ding, C. Li, D. Zhao, Z. Qian, Z. Zhang, L. Zhang and L. Yin, *Nat. Commun.*, 2020, **11**, 1576.
- 104 B. Sun, X. Huang, S. Chen, P. Munroe and G. Wang, *Nano Lett.*, 2014, **14**, 3145–3152.
- 105 H. W. Park, D. U. Lee, L. F. Nazar and Z. Chen, *J. Electrochem. Soc.*, 2012, **160**, A344.
- 106 B. D. McCloskey, A. Speidel, R. Scheffler, D. C. Miller, V. Viswanathan, J. S. Hummelshøj, J. K. Nørskov and A. C. Luntz, *J. Phys. Chem. Lett.*, 2012, **3**, 997–1001.
- 107 B. M. Gallant, R. R. Mitchell, D. G. Kwabi, J. Zhou, L. Zuin, C. V. Thompson and Y. Shao-Horn, *J. Phys. Chem. C*, 2012, **116**, 20800–20805.
- 108 Z. Jian, P. Liu, F. Li, P. He, X. Guo, M. Chen and H. Zhou, *Angew. Chem., Int. Ed.*, 2014, **53**, 442–446.
- 109 C.-S. Yang, Z. Sun, Z. Cui, F.-L. Jianga, J.-W. Denga and T. Zhang, *Energy Storage Mater.*, 2020, **30**, 59–66.
- 110 Q. Li, P. Xu, W. Gao, S. Ma, G. Zhang, R. Cao, J. Cho, H.-L. Wang and G. Wu, *Adv. Mater.*, 2014, **26**, 1378–1386.
- 111 Y.-C. Lu, H. A. Gasteiger and Y. Shao-Horn, *J. Am. Chem. Soc.*, 2011, **133**, 19048–19051.
- 112 T. Bligaard and J. K. Nørskov, *Electrochim. Acta*, 2007, **52**, 5512–5516.
- 113 Y. Zhou and S. Guo, *eScience*, 2023, **3**, 100123.
- 114 S. Sankarasubramanian, N. Singh, F. Mizuno and J. Prakash, *J. Power Sources*, 2016, **319**, 202–209.
- 115 Q. He, T. Xu, J. Li, J. Wang, C. Jin, Q. Chen, X. Gu, X. Wang, J. Wei, H. Duan and Y. Gong, *Adv. Energy Mater.*, 2022, **12**, 2200849.
- 116 W.-B. Luo, X.-W. Gao, S.-L. Chou, J.-Z. Wang and H.-K. Liu, *Adv. Mater.*, 2015, **27**, 6862–6869.
- 117 R. Choi, J. Jung, G. Kim, K. Song, Y.-I. Kim, S. C. Jung, Y.-K. Han, H. Song and Y.-M. Kang, *Energy Environ. Sci.*, 2014, **7**, 1362–1368.
- 118 L. Zhang, H. Jang, H. Liu, M. G. Kim, D. Yang, S. Liu, X. Liu and J. Cho, *Angew. Chem., Int. Ed.*, 2021, **60**, 18821–18829.
- 119 Y. Lee, J. Suntivich, K. J. May, E. E. Perry and Y. Shao-Horn, *J. Phys. Chem. Lett.*, 2012, **3**, 399–404.
- 120 Y. Zhang, S. Zhang, J. Ma, A. Huang, M. Yuan, Y. Li, G. Sun, C. Chen and C. Nan, *ACS Appl. Mater. Interfaces*, 2021, **13**, 39239–39247.
- 121 Z. Lian, Y. Lu, S. Zhao, Z. Li and Q. Liu, *Adv. Sci.*, 2023, **10**, 2205975.
- 122 C. Tang, P. Sun, J. Xie, Z. Tang, Z. Yang, Z. Dong, G. Cao, S. Zhang, P. V. Braun and X. Zhao, *Energy Storage Mater.*, 2017, **9**, 206–213.



- 123 F. Li, D.-M. Tang, T. Zhang, K. Liao, P. He, D. Golberg, A. Yamada and H. Zhou, *Adv. Energy Mater.*, 2015, **5**, 1500294.
- 124 X. Guo, P. Liu, J. Han, Y. Ito, A. Hirata, T. Fujita and M. Chen, *Adv. Mater.*, 2015, **27**, 6137–6143.
- 125 K. Guo, Y. Li, T. Yuan, X. Dong, X. Li and H. Yang, *J. Solid State Electrochem.*, 2015, **19**, 821–829.
- 126 J. Zheng, W. Zhang, R. Wang, J. Wang, Y. Zhai and X. Liu, *Small*, 2023, **19**, 2204559.
- 127 O. M. Yaghi and H. Li, *J. Am. Chem. Soc.*, 1995, **117**, 10401–10402.
- 128 A. J. Howarth, A. W. Peters, N. A. Vermeulen, T. C. Wang, J. T. Hupp and O. K. Farha, *Chem. Mater.*, 2017, **29**, 26–39.
- 129 J. Lee, O. K. Farha, J. Roberts, K. A. Scheidt, S. T. Nguyen and J. T. Hupp, *Chem. Soc. Rev.*, 2009, **38**, 1450–1459.
- 130 D. Wu, Z. Guo, X. Yin, Q. Pang, B. Tu, L. Zhang, Y.-G. Wang and Q. Li, *Adv. Mater.*, 2014, **26**, 3258–3262.
- 131 Z. Ye, Y. Jiang, L. Li, F. Wu and R. Chen, *Nano-Micro Lett.*, 2021, **13**, 203.
- 132 Q. Lv, Z. Zhu, Y. Ni, B. Wen, Z. Jiang, H. Fang and F. Li, *J. Am. Chem. Soc.*, 2022, **144**, 23239–23246.
- 133 W. Yin, Y. Shen, F. Zou, X. Hu, B. Chi and Y. Huang, *ACS Appl. Mater. Interfaces*, 2015, **7**, 4947–4954.
- 134 L. Zhao, J. Feng, A. Abbas, H. Sun, C. Wang and H. Wang, *J. Mater. Chem. A*, 2024, **12**, 30591–30600.
- 135 Z. Lyu, G. J. H. Lim, R. Guo, Z. Kou, T. Wang, C. Guan, J. Ding, W. Chen and J. Wang, *Adv. Funct. Mater.*, 2019, **29**, 1806658.
- 136 Y. Yang, X. Hu, G. Wang, J. Han, Q. Zhang, W. Liu, Z. Xie and Z. Zhou, *Adv. Funct. Mater.*, 2024, **34**, 2315354.
- 137 W. Cheng, X. Zhao, H. Su, F. Tang, W. Che, H. Zhang and Q. Liu, *Nat. Energy*, 2019, **4**, 115–122.
- 138 Z. Zhu, X. Shi, G. Fan, F. Li and J. Chen, *Angew. Chem., Int. Ed.*, 2019, **58**, 19021–19026.
- 139 J. Zhou, Z. Han, X. Wang, H. Gai, Z. Chen, T. Guo, X. Hou, L. Xu, X. Hu, M. Huang, S. V. Levchenko and H. Jiang, *Adv. Funct. Mater.*, 2021, **31**, 2102066.
- 140 Y. Yuan, K. Amine, J. Lu and R. Shahbazian-Yassar, *Nat. Commun.*, 2017, **8**, 15806.
- 141 P. Schwager, H. Bülter, I. Plettenberg and G. Wittstock, *Energy Technol.*, 2016, **4**, 1472–1485.
- 142 D. Sharon, D. Hirsberg, M. Afri, F. Chesneau, R. Lavi, A. A. Frimer, Y.-K. Sun and D. Aurbach, *ACS Appl. Mater. Interfaces*, 2015, **7**, 16590–16600.
- 143 C.-E. Dutoit, M. Tang, D. Gourier, J.-M. Tarascon, H. Vezin and E. Salager, *Nat. Commun.*, 2021, **12**, 1410.
- 144 J. Chen, E. Quattrocchi, F. Ciucci and Y. Chen, *Chem*, 2023, **9**, 2267–2281.
- 145 X. Liao, R. Lu, L. Xia, Q. Liu, H. Wang, K. Zhao, Z. Wang and Y. Zhao, *Energy Environ. Mater.*, 2022, **5**, 157–185.
- 146 J. Suntivich, H. A. Gasteiger, N. Yabuuchi, H. Nakanishi, J. B. Goodenough and Y. Shao-Horn, *Nat. Chem.*, 2011, **3**, 546–550.
- 147 Y. Pan, R. Xu, A. Hu, C. Zhao, R. Li, B. Zhou, J. Liu and J. Long, *Batteries Supercaps*, 2024, **7**, e202300609.
- 148 S. Chen, L. Jin, Y. Ji and Y. Li, *J. Mater. Chem. A*, 2025, **13**, 9841–9848.
- 149 S. A. Freunberger, Y. Chen, N. E. Drewett, L. J. Hardwick, F. Bardé and P. G. Bruce, *Angew. Chem., Int. Ed.*, 2011, **50**, 8609–8613.
- 150 X. Gao, Y. Chen, L. R. Johnson, Z. P. Jovanov and P. G. Bruce, *Nat. Energy*, 2017, **2**, 17118.
- 151 Y. Chen, S. A. Freunberger, Z. Peng, O. Fontaine and P. G. Bruce, *Nat. Chem.*, 2013, **5**, 489–494.
- 152 B. Liu, W. Xu, J. Tao, P. Yan, J. Zheng, M. H. Engelhard, D. Lu, C. Wang and J.-G. Zhang, *Adv. Energy Mater.*, 2018, **8**, 1702340.
- 153 J. Zhu, J. Yang, J. Zhou, T. Zhang, L. Li, J. Wang and Y. Nuli, *J. Power Sources*, 2017, **366**, 265–269.
- 154 J.-H. Kim, H.-S. Woo, W. K. Kim, K. H. Ryu and D.-W. Kim, *ACS Appl. Mater. Interfaces*, 2016, **8**, 32300–32306.
- 155 D. Liu, Z. Fu, S. Wang, X. Gong, T. You, H. Yu, Y. Jiang and Y. Zhang, *Angew. Chem., Int. Ed.*, 2025, **64**, e202425277.
- 156 A. Kilic, D. Eroglu and R. Yildirim, *J. Electrochem. Soc.*, 2021, **168**, 090544.
- 157 B. Lee, J. Yoo and K. Kang, *Chem. Sci.*, 2020, **11**, 7813–7822.
- 158 H. Tian, A. Song, H. Tian, J. Liu, G. Shao, H. Liu and G. Wang, *Chem. Sci.*, 2021, **12**, 7656–7676.
- 159 K. Song, E. Cho and Y.-M. Kang, *ACS Catal.*, 2015, **5**, 5116–5122.
- 160 Y. Zheng, R. Gao, L. Zheng, L. Sun, Z. Hu and X. Liu, *ACS Catal.*, 2019, **9**, 3773–3782.
- 161 D. Du, L. Wang, R. Zheng, M. Li, Z. Ran, L. Ren, M. He, Y. Yan and C. Shu, *J. Colloid Interface Sci.*, 2021, **601**, 114–123.
- 162 N. B. Aetukuri, B. D. McCloskey, J. M. García, L. E. Krupp, V. Viswanathan and A. C. Luntz, *Nat. Chem.*, 2015, **7**, 50–56.
- 163 R. R. Mitchell, B. M. Gallant, C. V. Thompson and Y. Shao-Horn, *Energy Environ. Sci.*, 2011, **4**, 2952–2958.
- 164 X. Lin, X. Lu, T. Huang, Z. Liu and A. Yu, *J. Power Sources*, 2013, **242**, 855–859.
- 165 C. Zor, K. D. Jones, G. J. Rees, S. Yang, A. Pateman, X. Gao, L. R. Johnson and P. G. Bruce, *Energy Environ. Sci.*, 2024, **17**, 7355–7361.
- 166 X. Yao, Q. Dong, Q. Cheng and D. Wang, *Angew. Chem., Int. Ed.*, 2016, **55**, 11344–11353.
- 167 B. D. McCloskey, R. Scheffler, A. Speidel, D. S. Bethune, R. M. Shelby and A. C. Luntz, *J. Am. Chem. Soc.*, 2011, **133**, 18038–18041.
- 168 S. J. Kang, T. Mori, S. Narizuka, W. Wilcke and H.-C. Kim, *Nat. Commun.*, 2014, **5**, 3937.
- 169 J. Wandt, P. Jakes, J. Granwehr, H. A. Gasteiger and R.-A. Eichel, *Angew. Chem., Int. Ed.*, 2016, **55**, 6892–6895.
- 170 N. Mahne, B. Schafzahl, C. Leypold, M. Leypold, S. Grumm, A. Leitgeb, G. A. Strohmeier, M. Wilkening, O. Fontaine, D. Kramer, C. Slugovc, S. M. Borisov and S. A. Freunberger, *Nat. Energy*, 2017, **2**, 1–9.
- 171 W.-J. Kwak, H. Kim, Y. K. Petit, C. Leypold, T. T. Nguyen, N. Mahne, P. Redfern, L. A. Curtiss, H.-G. Jung, S. M. Borisov, S. A. Freunberger and Y.-K. Sun, *Nat. Commun.*, 2019, **10**, 1380.
- 172 E. Mourad, Y. K. Petit, R. Spezia, A. Samojlov, F. F. Summa, C. Prehal, C. Leypold, N. Mahne, C. Slugovc, O. Fontaine, S. Brutti and S. A. Freunberger, *Energy Environ. Sci.*, 2019, **12**, 2559–2568.



- 173 W.-J. Kwak, Rosy, D. Sharon, C. Xia, H. Kim, L. R. Johnson, P. G. Bruce, L. F. Nazar, Y.-K. Sun, A. A. Frimer, M. Noked, S. A. Freunberger and D. Aurbach, *Chem. Rev.*, 2020, **120**, 6626–6683.
- 174 N. Mahne, S. E. Renfrew, B. D. McCloskey and S. A. Freunberger, *Angew. Chem., Int. Ed.*, 2018, **57**, 5529–5533.
- 175 S. Ahn, C. Zor, S. Yang, M. Lagnoni, D. Dewar, T. Nimmo, C. Chau, M. Jenkins, A. J. Kibler, A. Pateman, G. J. Rees, X. Gao, P. Adamson, N. Grobert, A. Bertei, L. R. Johnson and P. G. Bruce, *Nat. Chem.*, 2023, **15**, 1022–1029.
- 176 C. Zor, K. D. Jones, G. J. Rees, S. Yang, A. Pateman, X. Gao, L. R. Johnson and P. G. Bruce, *Energy Environ. Sci.*, 2024, **17**, 7355–7361.
- 177 T.-F. Hung, S. G. Mohamed, C.-C. Shen, Y.-Q. Tsai, W.-S. Chang and R.-S. Liu, *Nanoscale*, 2013, **5**, 12115–12119.
- 178 P. Li, W. Sun, Q. Yu, M. Guan, J. Qiao, Z. Wang, D. Rooney and K. Sun, *Mater. Lett.*, 2015, **158**, 84–87.
- 179 B. Liu, W. Xu, P. Yan, P. Bhattacharya, R. Cao, M. E. Bowden, M. H. Engelhard, C.-M. Wang and J.-G. Zhang, *ChemSusChem*, 2015, **8**, 3697–3703.
- 180 J.-C. Kim, G.-H. Lee, S. Lee, S.-I. Oh, Y. Kang and D.-W. Kim, *Adv. Mater. Interfaces*, 2018, **5**, 1701234.
- 181 K. Song, B. Yang, Z. Li, Y. Lv, Y. Yu, L. Yuan, X. Shen and X. Hu, *Appl. Surf. Sci.*, 2020, **529**, 147064.
- 182 Y. Pan, K. Li, A. Hu, C. Zhao, Y. Zhang, X. Jiang, B. Li, J. Wang and J. Long, *Chem. Eng. J.*, 2023, **477**, 147209.
- 183 L. Ren, X. Wen, D. Du, Y. Yan, H. Xu, T. Zeng and C. Shu, *Chem. Eng. J.*, 2023, **462**, 142288.
- 184 S. Peng, Y. Hu, L. Li, X. Han, F. Cheng, M. Srinivasan, Q. Yan, S. Ramakrishna and J. Chen, *Nano Energy*, 2015, **13**, 718–726.
- 185 L. Wang, T. Zhu, Z. Lyu, J. Zhang, L. Gong, S. Xiao, J. Liu, W. Dong, X. Cui, G. W. Ho and W. Chen, *RSC Adv.*, 2016, **6**, 98867–98873.
- 186 F. Tu, J. Xie, S. Zhang, G. Cao, T. Zhu and X. Zhao, *J. Mater. Chem. A*, 2015, **3**, 5714–5721.
- 187 C. Shen, Z. Wen, F. Wang, K. Rui, Y. Lu and X. Wu, *J. Power Sources*, 2015, **294**, 593–601.
- 188 P. Moni, S. Hyun, A. Vignesh and S. Shanmugam, *Chem. Commun.*, 2017, **53**, 7836–7839.
- 189 Z.-D. Yang, Z.-W. Chang, J.-J. Xu, X.-Y. Yang and X.-B. Zhang, *Sci. China:Chem.*, 2017, **60**, 1540–1545.
- 190 G. Liu, L. Zhang, S. Wang, L.-X. Ding and H. Wang, *J. Mater. Chem. A*, 2017, **5**, 14530–14536.
- 191 T. Guo, X. Qin, L. Hou, J. Li, X. Li and Q. Liang, *J. Solid State Electrochem.*, 2019, **23**, 1359–1369.
- 192 Y. Jiang, L. Zou, J. Cheng, Y. Huang, L. Jia, B. Chi, J. Pu and J. Li, *ChemElectroChem*, 2017, **4**, 3140–3147.
- 193 W. Zhao, X. Li, R. Yin, L. Qian, X. Huang, H. Liu, J. Zhang, J. Wang, T. Ding and Z. Guo, *Nanoscale*, 2019, **11**, 50–59.
- 194 L. Liu, J. Wang, Y. Hou, J. Chen, H.-K. Liu, J. Wang and Y. Wu, *Small*, 2016, **12**, 602–611.
- 195 J. Wang, R. Zhan, Y. Fu, H.-Y. Yu, C. Jiang, T.-H. Zhang, C. Zhang, J. Yao, J.-F. Li, X. Li, J.-H. Tian and R. Yang, *Mater. Today Energy*, 2017, **5**, 214–221.
- 196 X. Li, J. Liu, J. Zhang, S. Wu, D. Zhang and J. Shui, *Chem. Eng. J.*, 2021, **411**, 128403.
- 197 T. Priamushko, E. Budiyo, N. Eshraghi, C. Weidenthaler, J. Kahr, M. Jahn, H. Tüysüz and F. Kleitz, *ChemSusChem*, 2022, **15**, e202102404.
- 198 L. Ren, L. Wang, D. Du, R. Zheng, Y. Yan, M. He, Z. Ran, M. Li and C. Shu, *Electrochim. Acta*, 2022, **407**, 139891.
- 199 Y. Xia, L. Wang, G. Gao, T. Mao, Z. Wang, X. Jin, Z. Hong, J. Han, D.-L. Peng and G. Yue, *Nano-Micro Lett.*, 2024, **16**, 258.
- 200 Y. Xia, S. Fan, X. Jin, L. Wang, S. Lin, J. Yan, J. Han, Z. Yu, D.-L. Peng and G. Yue, *Nano Energy*, 2025, **141**, 111086.
- 201 S. Karunarathne, Y. Y. Kannangara, C. R. Ratwani, C. Sandaruwan, W. P. S. L. Wijesinghe, A. R. Kamali and A. M. Abdelkader, *Nanoscale*, 2024, **16**, 7937–7950.
- 202 Y. Liu, X. Hua, C. Xiao, T. Zhou, P. Huang, Z. Guo, B. Pan and Y. Xie, *J. Am. Chem. Soc.*, 2016, **138**, 5087–5092.
- 203 J. Kang, X. Yang, Q. Hu, Z. Cai, L.-M. Liu and L. Guo, *Chem. Rev.*, 2023, **123**, 8859–8941.
- 204 L. Johnson, C. Li, Z. Liu, Y. Chen, S. A. Freunberger, P. C. Ashok, B. B. Praveen, K. Dholakia, J.-M. Tarascon and P. G. Bruce, *Nat. Chem.*, 2014, **6**, 1091–1099.
- 205 D. Aurbach, B. D. McCloskey, L. F. Nazar and P. G. Bruce, *Nat. Energy*, 2016, **1**, 16128.
- 206 D. G. Kwabi, V. S. Bryantsev, T. P. Batcho, D. M. Itkis, C. V. Thompson and Y. Shao-Horn, *Angew. Chem., Int. Ed.*, 2016, **55**, 3129–3134.
- 207 N. B. Aetukuri, B. D. McCloskey, J. M. García, L. E. Krupp, V. Viswanathan and A. C. Luntz, *Nat. Chem.*, 2015, **7**, 50–56.
- 208 F. Li, S. Wu, D. Li, T. Zhang, P. He, A. Yamada and H. Zhou, *Nat. Commun.*, 2015, **6**, 7843.
- 209 W.-J. Kwak, D. Hirshberg, D. Sharon, H.-J. Shin, M. Afri, J.-B. Park, A. Garsuch, F. F. Chesneau, A. A. Frimer, D. Aurbach and Y.-K. Sun, *J. Mater. Chem. A*, 2015, **3**, 8855–8864.
- 210 C. M. Burke, R. Black, I. R. Kochetkov, V. Giordani, D. Addison, L. F. Nazar and B. D. McCloskey, *ACS Energy Lett.*, 2016, **1**, 747–756.
- 211 T. Liu, M. Leskes, W. Yu, A. J. Moore, L. Zhou, P. M. Bayley, G. Kim and C. P. Grey, *Science*, 2015, **350**, 530–533.
- 212 Y. Wang, N.-C. Lai, Y.-R. Lu, Y. Zhou, C.-L. Dong and Y.-C. Lu, *Joule*, 2018, **2**, 2364–2380.
- 213 J. W. Yeh, S. K. Chen, S. J. Lin, J. Y. Gan, T. S. Chin, T. T. Shun, C. H. Tsau and S. Y. Chang, *Adv. Eng. Mater.*, 2004, **6**, 299–303.
- 214 D. B. Miracle and O. N. Senkov, *Acta Mater.*, 2017, **122**, 448–511.
- 215 T. H. Dolla, S. P. Mbokazi, T. Matthews, R. Mohamed, L. L. Sikeyi, U. M. Tukur, J. Wang, P. F. Msomi, W. K. Maboya, P. R. Makgwane, N. Palaniyandy and M. K. Mathe, *Energy Storage Mater.*, 2025, **79**, 104357.
- 216 Q. Yu, S. Qiu and Z.-B. Jiao, *Rare Met.*, 2025, DOI: [10.1007/s12598-025-03358-z](https://doi.org/10.1007/s12598-025-03358-z).
- 217 J. K. Nørskov, T. Bligaard, A. Logadottir, S. Bahn, L. B. Hansen, M. Bollinger, H. Bengaard, B. Hammer, Z. Sljivancanin, M. Mavrikakis, Y. Xu, S. Dahl and C. J. H. Jacobsen, *J. Catal.*, 2002, **209**, 275–278.
- 218 J. Tian, Y. Rao, W. Shi, J. Yang, W. Ning, H. Li, Y. Yao, H. Zhou and S. Guo, *Angew. Chem., Int. Ed.*, 2023, **62**, e202310894.



- 219 L. Tao, M. Sun, Y. Zhou, M. Luo, F. Lv, M. Li, Q. Zhang, L. Gu, B. Huang and S. Guo, *J. Am. Chem. Soc.*, 2022, **144**, 10582–10590.
- 220 X. Wang, Q. Dong, H. Qiao, Z. Huang, M. T. Saray, G. Zhong, Z. Lin, M. Cui, A. Brozena, M. Hong, Q. Xia, J. Gao, G. Chen, R. Shahbazian-Yassar, D. Wang and L. Hu, *Adv. Mater.*, 2020, **32**, 2002853.
- 221 P. Zhang, X. Hui, Y. Nie, R. Wang, C. Wang, Z. Zhang and L. Yin, *Small*, 2023, **19**, 2206742.
- 222 R. Wu, Q. Zhang, Q. Yang, Z. Hu and Y. Zhao, *Nanoscale*, 2025, **17**, 10581–10588.
- 223 L. Li, M. Hua, J. Li, P. Zhang, Y. Nie, P. Wang, X. Lin, Z. Zhang, R. Wang, X. Ge, Y. C. Li and L. Yin, *ACS Nano*, 2025, **19**, 4391–4402.
- 224 C. Wang, Z. Zhang, W. Liu, Q. Zhang, X.-G. Wang, Z. Xie and Z. Zhou, *Angew. Chem., Int. Ed.*, 2020, **59**, 17856–17863.
- 225 Q. Zhang, S. Rao, S. V. C. Vummaleti, E. T. Poh, W. Dai, X. Cui, J. Wu, J. Zhang and W. Chen, *Adv. Energy Mater.*, 2022, **12**, 2200580.
- 226 P. Kichambare, S. Rodrigues, D. Firsich, W. A. Feld, K. Hankins, P. B. Balbuena and L. Scanlon, *Chem. Phys. Lett.*, 2024, **841**, 141179.
- 227 J. Kim, G. Y. Jung, C. Hwang, J. Jeong, K. Baek, J. Lee, S. J. Kang, S. K. Kwak and H.-K. Song, *J. Power Sources*, 2021, **492**, 229633.
- 228 S. Xing, Z. Zhengcai, D. Yaying, L. Minghui, W. Jing, Z. Zhang and Z. Zhou, *CCS Chem.*, 2024, **6**, 1810–1820.
- 229 J. Lai, N. Chen, F. Zhang, B. Li, Y. Shang, L. Zhao, L. Li, F. Wu and R. Chen, *Energy Storage Mater.*, 2022, **49**, 401–408.
- 230 H. Zhang, Y. Yu, D. Yang, Y. Fan, H. Chen, N. Zhang, Z. Wang, G. Huang and X. Zhang, *Adv. Mater.*, 2025, **37**, 2413948.
- 231 Y. Wang, L.-N. Song, Y.-F. Wang, X.-X. Wang, J.-Y. Wu, Y. Sun and J.-J. Xu, *Adv. Funct. Mater.*, 2024, **34**, 2405222.
- 232 L.-N. Song, L.-J. Zheng, X.-X. Wang, D.-C. Kong, Y.-F. Wang, Y. Wang, J.-Y. Wu, Y. Sun and J.-J. Xu, *J. Am. Chem. Soc.*, 2024, **146**, 1305–1317.
- 233 G.-H. Lee, M.-C. Sung and D.-W. Kim, *Chem. Eng. J.*, 2023, **453**, 139878.

